2024

Characterization of size effects in additively manufactured GRCop-42 and their influence on mechanical response

Gabriel Demeneghi

CHARACTERIZATION OF SIZE EFFECTS IN ADDITIVELY MANUFACTURED GRCOP-42 AND THEIR INFLUENCE ON MECHANICAL RESPONSE

Gabriel Demeneghi

A DISSERTATION

Submitted in partial fulfillment of the requirements
for the degree of Doctor of Philosophy
in
The Department of Mechanical Engineering
to
The Graduate School
of
The University of Alabama in Huntsville

May 2024

Approved by:

Dr. Kavan Hazeli, Research Advisor
Dr. George J. Nelson, Committee Chair
Dr. Babak Shotorban, Committee Member
Dr. Gang Wang, Committee Member
Dr. Jason R. Mayeur, Committee Member
Dr. George J. Nelson, Department Chair
Dr. Shankar Mahalingam, College Dean
Dr. Jon Hakkila, Graduate Dean

Abstract

CHARACTERIZATION OF SIZE EFFECTS IN ADDITIVELY MANUFACTURED GRCOP-42 AND THEIR INFLUENCE ON MECHANICAL RESPONSE

Gabriel Demeneghi

A dissertation submitted in partial fulfillment of the requirements for the degree of Doctor of Philosophy

Mechanical Engineering

The University of Alabama in Huntsville
May 2024

This study investigates size effects on microstructure, mechanical behavior, and fatigue performance of additively manufactured GRCop-42. Systematic analyses, encompassing changes on powder composition, wall thickness, and heat treatment, was conducted on specimens produced through laser powder bed fusion (L-PBF) and laser powder direct energy deposition (DED) techniques. L-PBF specimens exhibited a reduction in strength and elongation with decreasing thickness, attributed to increasing porosity as specimen's thickness decreases. Conversely, in DED specimens, decreasing mechanical properties with thickness were associated to surface topography. Emphasizing the non-generalizability of size effects across AM methods. Size effects were also investigated on high cycle fatigue, as tensile properties cannot be readily translated into fatigue properties. Fatigue testing of L-PBF specimens revealed internal defects as operative features responsible for an early fatigue failure, which were remediated by hot isostatic pressing. Fractography unveiled size-dependent fatigue characteristics, particularly an increased presence of brittle features on thinner specimens. This investigation highlights the significance of size effect considerations for GRCop-42 in AM applications.

Acknowledgements

The Ph.D. journey is a rigorous and demanding path that takes a toll on one's physical, mental, and social well-being, often affecting those closest to us. It demands significant sacrifices, including missed special occasions, holidays, and quality time with family and friends. Undertaking this journey isn't a solo endeavor; it requires the unwavering support and assistance of mentors, advisors, and loved ones. To all those who have been part of this challenging yet rewarding marathon, I offer my heartfelt gratitude.

Foremost, I extend my deepest appreciation to my advisor and mentor, Dr. Kavan Hazeli. His guidance, encouragement, and support have been the cornerstone of this work. Without his expertise and mentorship, this achievement would not have been possible.

I'm sincerely thankful to the members of my advisory committee, Dr. Jason Mayeur, Dr. George Nelson, Dr. Babak Shotorban, and Dr. Gang Wang. Their commitment to reviewing this dissertation and the time they've devoted to my academic journey is truly invaluable. Special thanks to Dr. Jason Mayeur for his insightful discussions, instructions, and scientific review and advice over the years.

My gratitude also goes out to Paul Gradl, whose mentorship and support have been instrumental not only in this research but in my entire professional development. Additionally, I want to acknowledge my NASA colleagues, whose support and guidance played a vital role in the successful completion of this project.

Lastly, but by no means least, I'm profoundly thankful to my family. Their unyielding support sustained me through this journey. I want to express my gratitude for their understanding of the sacrifices this path entailed. Everything I have achieved is a reflection of your support and sacrifices. I owe everything I am to you!

Table of Contents

List of Figures

List of Tables

I have been impressed with the urgency of doing. Knowing is not enough; we must apply. Being willing is not enough; we must do.

- Leonardo da Vinci

Leave this world a little better than you found it.

- Robert Baden-Powell

Chapter 1. Introduction

Additive manufacturing (AM) has enabled the fabrication of components with intricate geometries while minimizing fabrication steps and the need for post-fabrication machining. This fabrication method has significantly impacted industries by making it easier to produce components with internal channels, delicate features, and complex geometric designs, resulting in substantial cost savings, reduced production times, and diminished material waste. AM's unparalleled design freedom also permits the reduction in component thickness, leading to a potential reduced weight and increased surface area, a desirable trait in numerous sectors, including industries such as aerospace, automotive, energy, chemical, among others. However, this reduction in size can introduce unique challenges known as "size effects".

Size effects first surfaced when discrepancies were observed in the mechanical behavior of smaller "witness" specimens compared to their full scale counterparts. These smaller specimens exhibited longer fatigue lives and higher fatigue strength, but these effects could not be uniformly generalized, as they were influenced by the specimen size and specific features arising from the fabrication process.

In addition to the size effects seen in traditionally manufactured components, AM introduces its own set of complexities. Inherent characteristics of

AM, such as surface topography, residual stresses, and internal defects, can have unpredictable consequences, which become more pronounced as component size decreases. Moreover, the grain structure (size, morphology, and orientation), porosity (size, shape, and distribution), and surface topography (roughness and waviness) can be influenced by the the solidification rate during AM fabrication process, creating variations in material properties. Even when these inherent features remain unaffected by the build process, the reduced thickness of specimens means that the grains, porosity, and surface topography become a more substation fraction of the cross-sectional area, directly impacting the mechanical response.

Furthermore, accurate measurement of the specimen's cross-section becomes crucial in determining yield stress and ultimate tensile stress for AM components, given their unique surface topography. Surface roughness and, to a greater extent, surface waviness can lead to an overestimation of the load-bearing area, which can impact the design, potentially resulting in over-engineering or, worst, premature failure. Therefore, establishing a relationship between the measured area and surface topography is essential to accurately determine the effective load-bearing area of specimens.

To mitigate these manufacturing-induced microstructural features, post-processing techniques such as surface polishing and heat treatments are employed. These post fabrication processes are used with the intent to reduce surface topography, close internal porosity, relieve residual stresses, and homogenize the microstructure. However, post-processing steps add complexity, time, and cost

to component fabrication, and their precise effects on mechanical properties and size effects remain unclear.

The work herein seeks to quantify the size effects on GRCop-42, a material commonly used in rocket combustion engines, using two AM methods; laser powder bed fusion (L-PBF) and direct energy deposition (DED). It is crucial to note that specific size effects are highly dependent on the fabrication process, which cannot be generalized to all AM methods and, instead, need to be individually determined for each deposition technique. The experiments conducted consider surface topography, internal porosity, microstructure, and mechanical response for specimens with varying thicknesses, all fabricated using the same printing parameters for each deposition method. Additionally, this research investigates the impact of hot isostatic pressing (HIP) on mechanical properties and its effectiveness in reducing porosity and enhancing microstructural uniformity as a function of thickness.

The selection of GRCop-42 as the model material stems from its increasing use in aerospace, particularly in rocket propulsion systems where the demand for thin structures to meet stringent certifications, such as NASA-STD-6030 [10], is pressing. Further insights into the practical application of GRCop-42 are presented in Section 2.4.1.

Chapter 2. Background and Literature Review

2.1 Thin Structures

Thin structures are attractive design features primarily for their capacity to offer significant advantages including reduced weight and augmented surface area. These attributes translate into tangible benefits for diverse fields. For instance, thin structures can substantially enhance surface area, making them invaluable in applications such as heat exchangers and chemical catalysis [4]. Moreover, the replacement of fully dense components with thin structures translates directly into reduced overall weight, leading to lower fuel consumption in vehicles ranging from rockets and airplanes to everyday automobiles. This, in turn, results in reduced operational costs and environmental benefits. Additionally, the integration of lattice structures into designs unlocks the potential for intelligent load distribution, which enables the absorption of impact energy and efficient load-bearing, all while maintaining a minimum stiffness [2, 11]. Figure 2.1 illustrates the versatility on thin wall applications. (a) cooling channels, (b) lattice structures, (c) structural components, and (d) lattice structures infills.

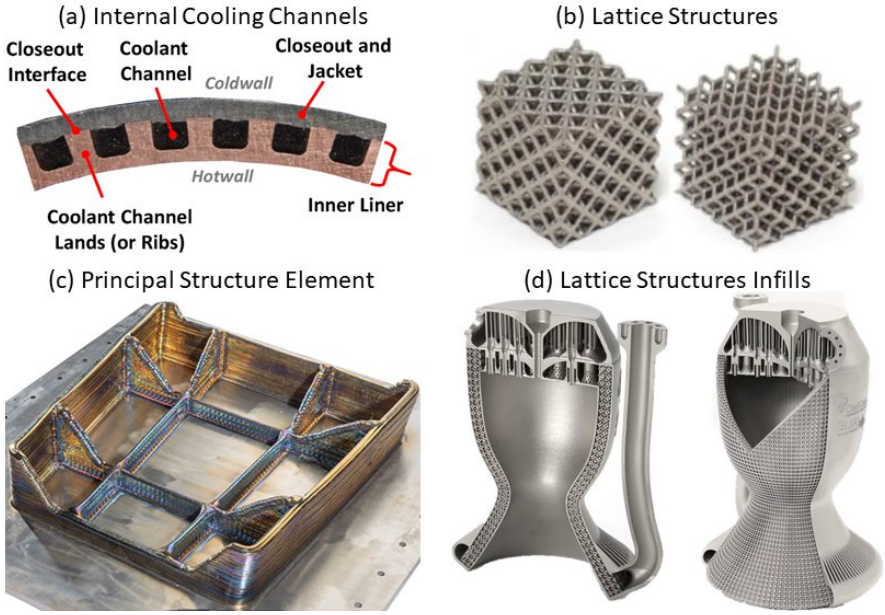

Figure 2.1: Application of thin structures including (a) internal cooling channels [1], (b) AM lattice structures [2], (c) DED principal structure element [3], and (d) single-piece rocket propulsion engine by SLM Solutions [4].

While the advantages of thin structures are evident, it is important to recognize that their fabrication is typically a complex and multi-step process, involving the manufacturing of various components, intricate assembly, and meticulous post-processing. These challenges have traditionally limited the widespread adoption of thin structures, however, AM poses a solution to their fabrication. AM removes barriers that have made thin structure production costly, time consuming, and challenging to achieve through conventional manufacturing [12]. With AM, the possibility of building intricate, light-weight structures has become tangible.

2.2 Additive Manufacturing

Additive manufacturing has changed the way manufacturing is perceived in virtually every field, including aerospace, automotive, energy, oil and gas, tool and die, medical, and others [13]. This transformative technology enables the direct fabrication of intricate, geometrically complex components from digital designs, eliminating the need for traditional, labor-intensive processes involving tooling or molding.

This work delves into two prominent additive manufacturing methods: laser-powder bed fusion (L-PBF) and direct energy deposition (DED). These techniques offer unique attributes, each with its own set of advantages and disadvantages, which necessitate careful consideration in both the manufacturing and end-use stages. Figure 2.2 provides schematic representations of both setups: (a) L-PBF and (b) DED.

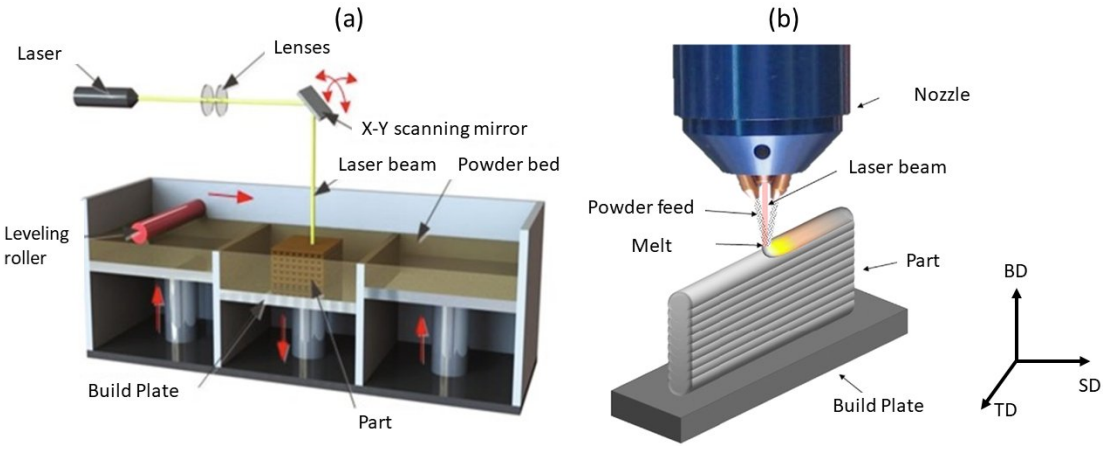

Figure 2.2: Diagrams showing the different deposition methods setups for (a) L-PBF [5] and (b) DED [6].

In L-PBF, a thin layer of metal powder is evenly distributed onto a vertically movable platform situated within a controlled environment filled with argon or nitrogen to ensure inert conditions. A continuous wave laser scans the predefined area based on the input computer-aided design (CAD) file, effectively melting the deposited powder. Subsequently, the platform descends by one layer height, and this procedure is repeated until the entire component is fully constructed, layer-by-layer [14, 15, 16, 12, 17].

In contrast, the DED methods involves the controlled delivery of material from a nozzle into a concentrated heat source, facilitating the deposition of the material onto pre-existing layers [18, 19, 20, 21]. Notably, DED exhibits advantage of reduced constraints on part size compared to other AM techniques, enabling the production of larger components as a single, integrated entities [20]. However, its essential to acknowledge that DED typically employs larger-diameter powder particles and requires a higher heat input. While this allows for accelerated deposition rates, it also results in thicker walls and coarser surface features compared to methods such as L-PBF [1, 22, 23].

The AM deposition process can also gives rise to a distinct set of defects that can impact the structural integrity and functionality of fabricated components. These defects arise from the complex interplay of process parameters, material characteristics, and the layer-by-layer deposition approach used in AM, including residual stresses due to rapid solidification and thermal gradients between layers, irregular shape porosity due to incomplete powder melting during

the layer build-up, spherical porosity from entrapped gas bubbles, among others [24, 25, 26, 27].

It is important to note that the characteristics and prevalence of these defects (shape, size, orientation, density, and location) are highly dependent on the specific AM process, parameters, and material composition. For example, insufficient energy leads to lack of fusion (LoF) defects and lack of bonding between deposited layers. In contrast, high power may vaporize the powder and entrap gases in the melt pool [27]. Additionally, the layer-to-layer deposition method results in a thermal gradient between the layer's top and bottom, leading to geometrical deviations from the CAD file [28, 16] and also giving rise to residual stresses [29].

The characteristic defects inherent to AM processes can significantly impact the mechanical properties of fabricated components. It has been shown in [12] that mechanical properties in L-PBF components, such as ultimate tensile strength (UTS), may exhibit a reduction of approximately 20 % to 25 % compared to conventionally manufactured counterparts, *i.e.,* hot-rolled parts, this is particularly true for components in the as-built condition (no post-processing heat treatment). This discrepancy in mechanical properties is likely related to stress concentrations during loading caused by residual porosity.

2.3 Size Effects

Evidence of the study of size effects on the strength of materials can be dated back to scientists such as Leonardo da Vinci (1500's), Galileo (1638), and

Mariotte (1686) [30]. Where Leonardo da Vinci experimented with the strength of iron wires of a given thickness of various wire lengths, Leonardo suspended a basket using a wire and slowly filled the basked with sand, once the wire breaks, a spring stops the sand from flowing and the sand on the basket can be weighed to establish the tensile strength of the wire [31]. Leonardo found that the strength of the wire was inversely proportional to its length [30]. Mariotte contributed further to the study of size effects and concluded that the strength of a "rope" was independent of its length as long as there was no flaws within it [30].

Following these experiments, the next recorded evidence of the study of size effects is found on Griffiths work. Griffith experimentally determined that the strength of glass fibers increased from approximately 291MPa to 3.39GPa as the diameter decreased from 0.1mm to 0.003mm [32], which was determined to be due to the presence of flaws in the fiber. These experiments established the basis for the statistical size effects, consisting of the weakest link model and extreme value statistics, which was completed by Weibull with a new statistical distribution method: The Weibull distribution [30, 33].

More recently, size effects are assessed to investigate variations in mechanical properties as the size or scale of a component changes. Mechanical properties of materials are routinely assessed through laboratory experiments conducted on small-scale specimens, serving as representative proxies, or "witness", for the actual components. This practice is adopted to circumvent the challenges associated with testing full-scale components. Nevertheless, it is imperative to recognize that the mechanical behavior of thin specimens cannot be assumed to mirror that of

bulk specimens. Consequently, an in-depth examination of how specimens size influences material properties is indispensable [34]. The study of specimen size effects can be categorized into three distinct domains [34, 35]:

1. **Statistical size effects:** These defects revolve around the probability of finding flaws within a region increases with the increased volume of the stressed region.

2. **Geometrical size effect:** This aspect pertains to alterations in the stress gradient and their impact on the fatigue life. In essence, reducing the size of structural notches diminishes the fatigue life of the material.

3. **Technological size effects:** These effects stem from variations in the fabrication process, giving rise to different microstructures, surface characteristics (such as roughness and waviness), and residual stresses within the final component.

It is noteworthy to emphasize that technological size effects are intricately intertwined with the specific fabrication methods employed. Consequently, different manufacturing approaches will engender distinct sources of size effect. Furthermore, the role played by inherent features, such as internal defects and surface topography, in influencing material yielding and failure will exhibit variations.

The origin of size effects in AM components can be attributed to several contributing factors, encompassing aspects related to fabrication or experimental method, the microstructural characteristics, and the morphological attributes of

specimens. Figure 2.3 provides a chart with the origin of size effects in AM components.

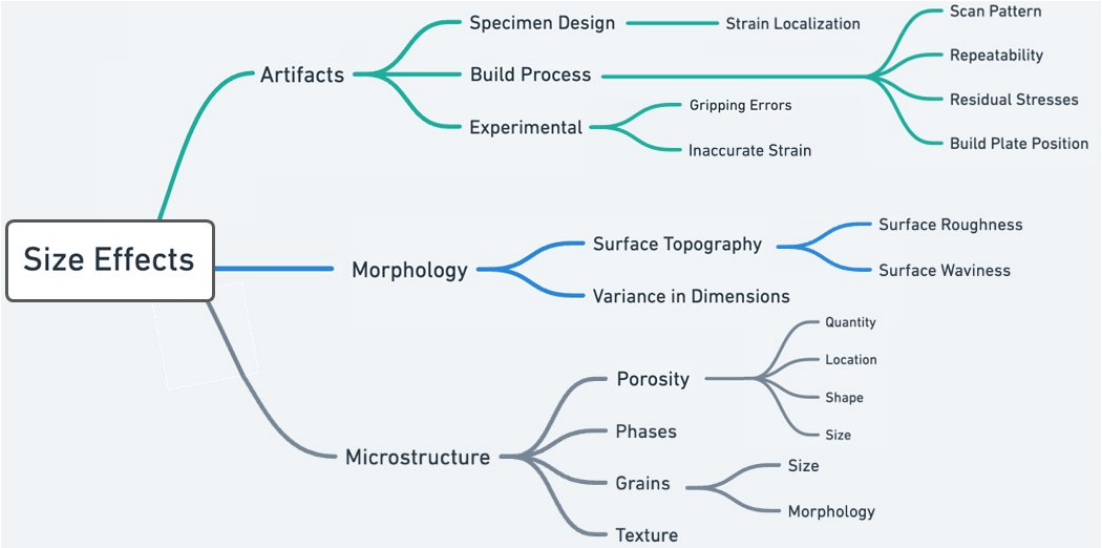

Figure 2.3: Diagram showing the possible origin for size effects dependent on the fabrication process.

Although this list provides an initial framework for understanding the sources of size effects, it is not exhaustive as different deposition techniques lead to different features. The variation in fabrication processes, characterized by differing environmental condition, feedstock materials, energy sources, and deposition procedures, imparts a unique fingerprint to the size effects observed in each case. Thus, it is necessary to meticulously discern the distinctive features contributing to size effects within each individual AM process.

While defects arising from AM methods are detrimental to the mechanical properties of components, including strength and elongation, they can be remediated post-fabrication through the application of heat treatments and ma-

chining, at the expense of additional fabrication cost and time. For instance, HIP has demonstrated effectiveness in mitigating internal defects in AM components [36, 37, 38, 39]. However, it is necessary to acknowledge the limitations of HIP, as it exhibits limited impact on surface-connected pores and near-surface porosity [38, 39]. Furthermore, HIP's efficacy has been observed to decrease as the thickness of GRCop-42 diminishes from 2mm to 0.7mm [40], and the non-closure of porosity in AM thin parts, such as lattice structures [2]. Additionally, larger pores might undergo flattening during HIP, rendering them undetectable via micro-computed tomography (µCT) and potentially detrimental to fatigue life [27]. Therefore, while avenues exist for mitigating AM defects, the defect's impact on AM components necessitates comprehensive investigation and understanding.

2.4 Copper Alloys

Copper alloys are highly sought after for applications requiring high conductivity and mechanical strength simultaneously. In addition to these advantageous properties, copper alloys exhibit remarkable resistance to corrosion and oxidation, good machinability, hydrogen compatibility, and remain cost effective for numerous industrial applications [41]. While pure copper boasts an exceptional thermal conductivity, with values typically falling within the range of $400\frac{\mathrm{W}}{\mathrm{m\,K}}$, in stark contrast to materials such as nickel ($90\frac{\mathrm{W}}{\mathrm{m\,K}}$) and titanium ($20\frac{\mathrm{W}}{\mathrm{m\,K}}$) [42], it faces limitations in terms of strength at elevated temperatures. Consequently, the incorporation of alloying elements becomes imperative in scenarios demanding both high thermal conductivity and mechanical strength.

Whithin the realm of copper alloys, numerous candidates have garnered attention as suitable contenders for applications requiring high conductivity and mechanical strength simultaneously. Examples include NARloy-Z (Cu-Ag-Zr), C18150 (Cu-Cr-Zr) AMZIRC (Cu-Zr) and GRCop (Cu-Cr-Nb), with NARloy-Z having found utilization in the space shuttle engine until its final mission in 2011. However, despite its noteworthy attributes, NARloy-Z exhibited certain limitations, particularly in terms of reusability and operational temperature ranges. These limitations led to the a renewed interest om research and development endeavors, aimed at identifying and tailoring copper alloy formulations capable of enduring and excelling in the demanding environments encountered by components such as rocket engine combustion chamber liners [7, 43].

2.4.1 GRCop Alloys

Within the spectrum of copper alloys, one notable mention is the GRC alloy family, originally developed by NASA Glenn Research Center in 1986 to be used in rocket combustion chambers [44, 45, 46]. It offers improved mechanical strength (ambient temperature ultimate tensile strength between 350 and 700MPa, compared to 300MPa for pure copper) while maintaining 70 to 85% the thermal conductivity of pure copper [42, 47, 48, 49, 17]. To date, the GRC alloy family has seen the maturation of two distinct compositions: GRCop-84 (Cu, 8 at% Cr, 4 at% Nb) and GRCop-42 (Cu, 4 at% Cr, 2 at% Nb). Figure 2.4 shows a GRCop (Cu-Cr_2Nb) phase diagram calculate by Menneci et al [7].

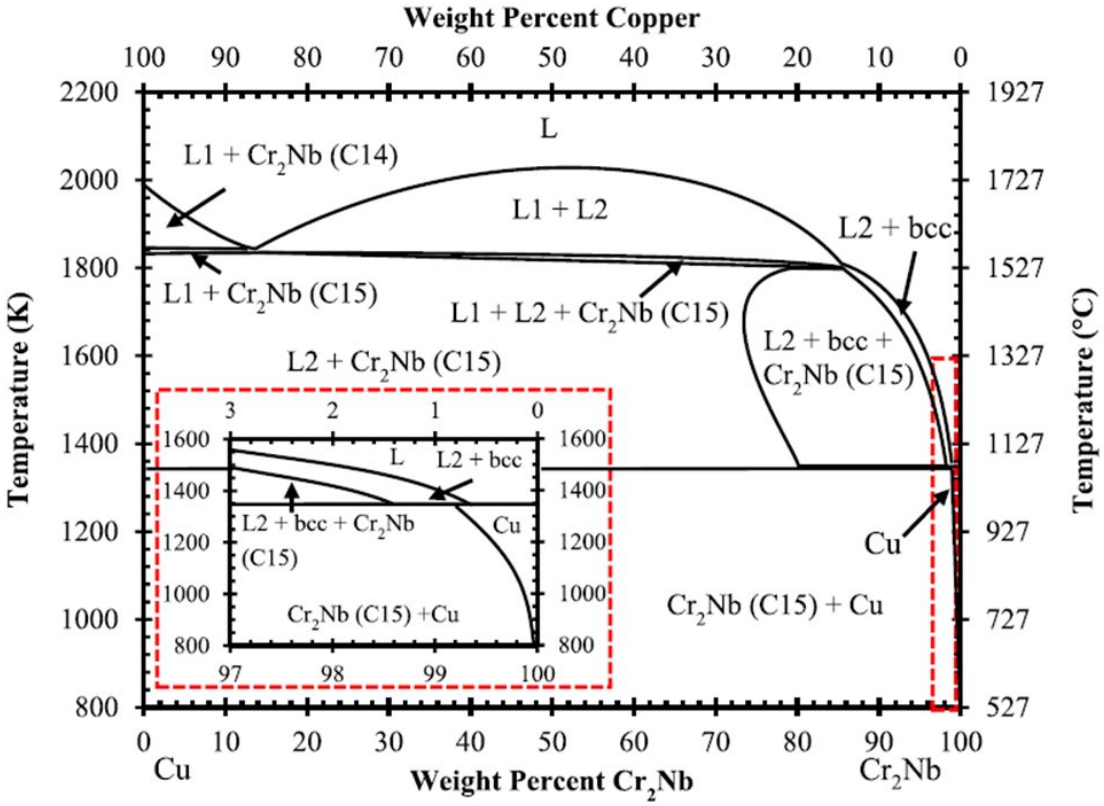

Figure 2.4: Cu-Cr_2Nb phase diagram [7] calculated from Zinkle *et al.* [8].

The boxed red dashed lines shows a magnified view of the alloy composition, revealing a distinct lack of solubility of Cr_2Nb within the Cu matrix. Consequently, GRCop has two distinct phases, Cu and Cr_2Nb. Notably, Cr_2Nb intermetallic phase has two polymorphs [7, 8], a solid that can be arranged in more than one crystal structure, a C14 - hexagonal unit cell, and a C15 - cubic unit cell. From the Cu-Cr_2Nb phase diagram, it becomes evident that below approximate temperature threshold of 1350°C, the cubic (C15) Laves phases of Cr_2Nb commence precipitating withing the copper matrix. Where the C15 Laves

phase has a face centered cubic (FCC) crystal structure characterized by four interpenetrating layers, which effectively inhibit dislocation at lower temperatures.

Both compositions, GRCop-84 and GRCop-42, leverage the advantageous attributes of chromium and niobium, both of which exhibit a low solubility in copper and a high affinity for each other. Through alloying, these elements form intermetallic compounds, Cr_2Nb intermetallic phase, which disperses within the copper matrix. The precipitation imparts a considerable strength increase in the alloy strength, achieved through a dispersion strengthening mechanism, while preserving an almost pure copper matrix that retains it high thermal conductivity. In essence, the GRC family embodies a unique set of qualities, including low thermal expansion, high thermal conductivity, high ductility, high operating temperature, high oxidation resistance, high low-cycle fatigue strength, and low creep rate [49, 50, 51]. These combination of properties renders GRCop alloys highly desirable for a diverse array of applications, particularly those demanding a high thermal conductivity while maintaining high mechanical strength.

Recently, GRCop-42 has become favored over GRCop-84 as a material of choice for rocket engine combustion chamber liners due to the increased thermal conductivity and maturing additive manufacturing supply chain [52]. The increased copper content in GRCop-42 results in a 5 to 8% increase in thermal conductivity and increased ductility in the HIP condition over GRCop-84 while maintaining comparable mechanical strength. Furthermore, GRCop-42 enables simplified powder atomization, as the reduced Cr and Nb content lowers the alloy's melting temperature. This decreases the likelihood of clogging the

atomization nozzle compared to GRCop-84 [52]. Additionally, build times are reduced for GRCop-42, as indicated in [52], since the layer thickness for successful GRCop-42 prints can be increased compared to GRCop-84. It is worth noting that these improvements are achieved at the expense of reduced fatigue strength. However, GRCOP-42 still satisfies the design requirements for reusable high heat flux applications [52, 17, 53].

As stated previously, GRCop alloys are well suited for applications requiring high thermal conductivity and high mechanical strength, one such application is in regeneratively cooled combustion engines. Figure 2.5 provides a depiction of a regeneratively cooled combustion chamber featuring a GRCop internal liner and a external jacket for structural support.

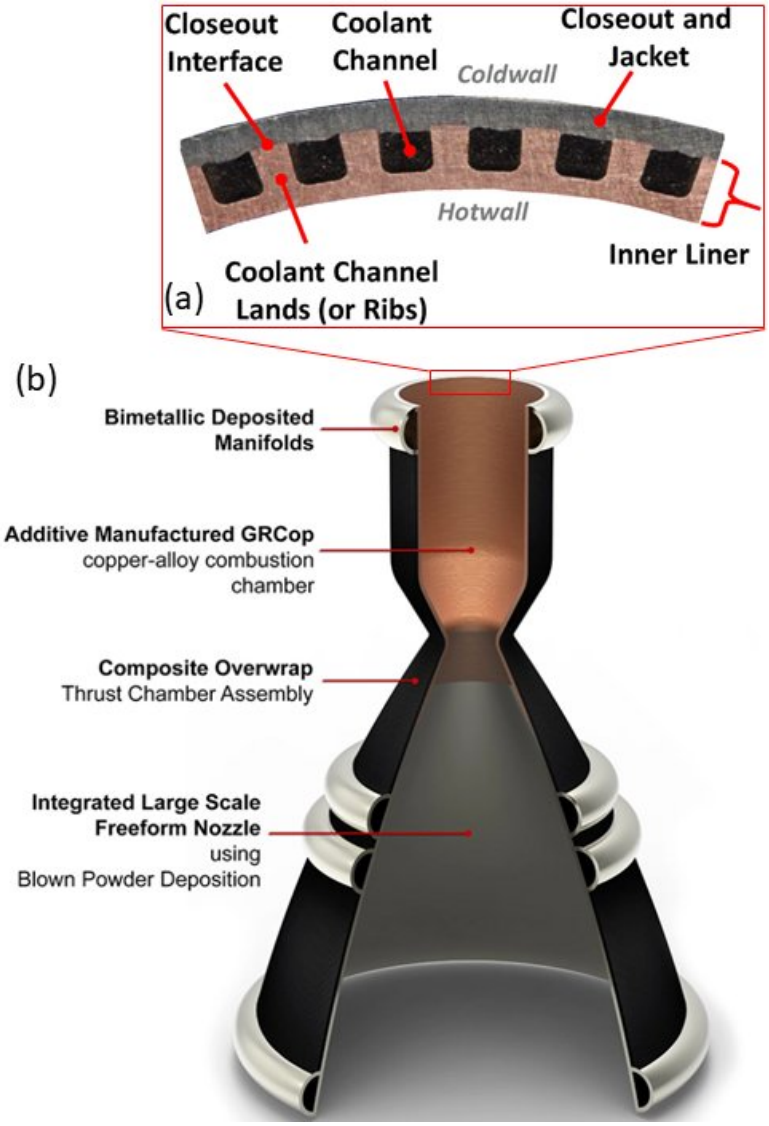

Figure 2.5: Part (a) shows a magnified view of the cooling channels [1] inside of a (b) regeneratively cooled combustion chamber [9].

Regeneratively cooled combustion chambers contain internal channels to flow high-pressure liquid or gaseous propellants. This configuration serves the dual purpose of preheating the fuel and preventing the combustion chamber

from overheating. During operation, these chambers experience elevated temperatures, ranging from approximately 400°C and 700°C [49], on the combustion side, while simultaneously handling high-pressure conditions and cryogenic temperatures within the internal channels. These operational conditions result in substantial thermal gradient, leading to thermal stresses, and endure high pressure, up to, or even greater than, 41MPa [17]. Consequently, they require materials capable of functioning both as efficient thermal conductors and structurally resilient components, making GRCop alloys an ideal choice.

2.4.2 Strengthening Mechanisms

GRCop alloys are dispersion strengthened by the addition of Cr and Nb particles. A 2:1 CrNb ratio is desired for all the Cr and Nb to combine and form an insoluble Cr_2Nb intermetallic, preserving the electrical conductivity of copper. However, an excess of Cr is used to ensure all Nb is combined to prevent the formation of niobium hydride during operation [46]. Additionally, Cr_2Nb is resistant to coarsening at high temperatures, effectively pinning grain boundaries within the copper matrix and retarding grain growth [7].

In any precipitation or dispersion hardening process, a range of particle sizes naturally arises due to variations in nucleation times and growth rates. Therefore, there exist both large and small Cr_2Nb particles within the material. The larger particles of irregular shape form along grain boundaries, serving to inhibit grain growth (following the Hall-Petch mechanism). While, smaller spher-

ical particles remain embedded within the copper matrix, impeding dislocation movement (operating according to Orowan mechanism) [46, 54, 55].

The dispersed particles in copper alloys are generally incoherent or stronger than the copper matrix and resistant to particle shearing. Consequently, the primary mechanism at play is Orowan strengthening [7]. The Orowan strengthening effect, denoted as $\Delta\sigma$, is represented by the following equation:

$$\Delta\sigma = \frac{0.13 G_\tau b}{\lambda_{LD}} ln(\frac{r}{b}) \tag{2.1}$$

where G_τ is the shear modulus (around 44GPa for copper), b is the burgers vector in the slip direction (0.255nm for copper [54]), f is the precipitate/dispersoid volume fraction (7% for GRCop-42 [55]), λ_{LD} is the linear mean free path of dislocations between particles, and r is the precipitate radius. The linear mean free path λ_{LD} can be approximated as follows:

$$\lambda_{LD} = \frac{4r(1-f)}{3f} \tag{2.2}$$

Furthermore, grain size strengthening, governed by Hall-Petch mechanism, is attainable since grain boundaries act as barriers to glide dislocations. Smaller grains lead to the dislocations being positioned closer together, thereby increasing their mutual interaction and further hindering dislocation movement [7]. The Hall-Petch strengthening effect, denoted as σ_y, is described by the following equation:

$$\sigma_y = \sigma_0 + k_y d^{-1/2} \tag{2.3}$$

where σ_0 is the Hall-Petch constant (about 26MPa for pure copper [54]), k_y is the strengthening coefficient (approximately 0.12MPa$\sqrt{\text{m}}$ for copper), and d is the grain diameter[54, 55].

Moreover, although both strengthening mechanisms are present and important in GRCop alloys, Hall-Petch strengthening has a greater effect on the overall strength of the alloy due to the Cr_2Nb intermetallic phase pinning the grains and preventing grain growth. Anderson *et al.* found that the grain boundary strengthening accounted for approximately two thirds of the total strength while Orowan strengthening accounts for the remainder [56].

Chapter 3. Experimental Procedure

3.1 Heat Treatment

HIP'ing serves as an effective methods to close out internal porosity and relieve residual stresses in AM components, as documented in various studies [40, 37, 57, 58, 39], and in mitigating anisotropy in elongation [57]. Therefore, to optimize the mechanical properties, including tensile strength and fatigue, for practical applications, the AM components will subjected to the HIP process in accordance to NASA STD 6030 standards [10]. However, it is noteworthy to mention that post-HIP porosity requires further investigation, as its effectiveness was shown to diminish as GRCop-42 component thickness reduces from 2mm to 0.7mm [40], and also due to the non-closure of porosity in additive manufactured thin parts, such as lattice structures [2].

The application of HIP aimed to reduce residual stresses that may accumulated during the build process, potentially leading to component distortion if removed from the build plate before stress relieving. In the case of L-PBF, specimens were tested in the as-built and HIP'd conditions. It is necessary to mention that as-built specimens underwent stress relieving process prior to removal from the build plate, but were not HIP'd. Conversely, all DED specimens underwent HIP post-deposition while still attached to the build plate.

Generally, HIP on copper alloys is conducted within the temperature range of 800 °C and 950 °C at a pressure of 100 MPa [59]. However, improved outcomes have been demonstrated when HIP is performed at a higher temperature of 1075 °C at 206.84 MPa for 2 hours (reduced from 4 hours to limit grain growth) [58]. Although increased success were achieved with higher temperatures and pressures, the specimens in this study underwent HIP at the more commonly employed lower temperature and pressure conditions. This decision was motivated by the Aerospace Structural Materials Handbook's report of GRCop-84's solidus temperature, approximately 1080 °C ±10 °C [48]. Ultimately, the HIP conditions chosen in this study were within the range for copper alloys presented in [59], however, precise details are omitted for proprietary data considerations.

3.2 Surface Analysis

Surface finish assessments for L-PBF specimens with varying thicknesses were conducted using a Keyence VR-5000 series 3D optical profiler, operating at 80× magnification. This non-contact measurement system employs white light interferometry and features a double telecentric lens. It captured an area measuring 3.8mm by 2.9mm with a resolution of 1024 × 768 px. For L-PBF specimens, the areal average (Sa) and root mean square surface roughness (Sq) were measured within the gage section for one specimen of each thickness (0.7 mm, 1.0 mm, 1.7 mm and 2.0 mm) in both the as-built and HIP'd conditions.

In the case of DED specimens, a more extensive surface analysis was required due to the layering effect inherent to the the single wall build-up process.

Surface topography examination was conducted using a Keyence VHX-1100 laser microscope equipped with a 20× magnification lens, operating at a working distance of 3.1mm, and employing the widefield focus variation scan mode. This microscope uses a 405nm laser to map and measure specimens surfaces, yielding a vertical resolution of approximately 20nm. To ensure accurate measurement the average surface characteristics, the gage section of two specimens from each wall was analyzed. A total of 36 images, with a 20% overlap, and then measuring the surface topography values of the entire mapped area in order to increase the confidence on the surface analysis results.

For the investigation of size effects on the fatigue life of L-PBF GRCop-42 specimens, the same equipment and configuration to that used on DED specimens was adopted. Specifically, three random locations, each covering an area of approximately 6.5mm^2, were selected for analysis. Figure 3.1 shows a specimen being measured and representative surface scans for individual specimens. The surface characteristics, including the average areal surface roughness (Sa) Equation (3.1), root mean square surface roughness (Sq) Equation (3.2), maximum measured valley depth (Sv) Equation (3.3), maximum measured peak height (Sp) Equation (3.4), and the collective range of maximum height of the surface (Sz) Equation (3.5), were calculated using the following equations where the peak height Z as a function of the coordinates x and y, and A is the area:

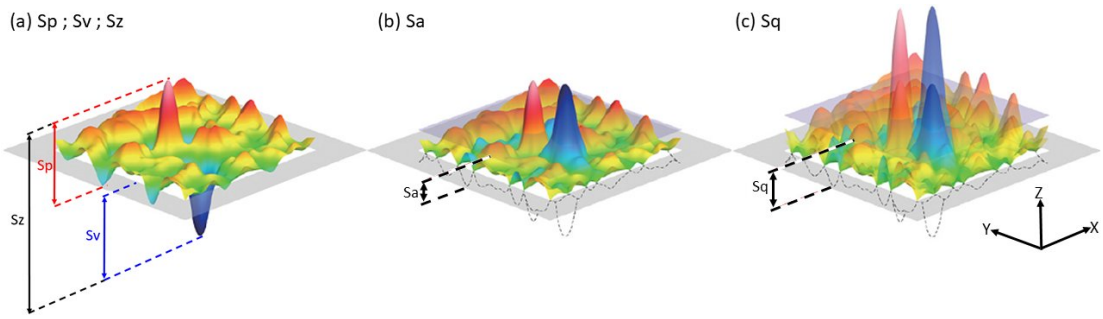

Figure 3.1: Graphical representation of the measure values for (a) Sp; Sv; Sz, (b) Sa, and (c) Sq. The gray plane represents the mean value for the measurements with indications of how each measurement is taken. Image courtesy of Evident Corporation.

$$Sa = \frac{1}{A} \int \int_A |Z(x,y)| dxdy \tag{3.1}$$

$$Sq = \sqrt{\frac{1}{A} \int \int_A Z^2(x,y) dxdy} \tag{3.2}$$

$$Sv = |min(Z(x,y))| \tag{3.3}$$

$$Sp = |max(Z(x,y))| \tag{3.4}$$

$$Sz = Sp + Sv \tag{3.5}$$

3.3 Internal Defects

To investigate the influence of specimen thickness on porosity size and distribution, determine effective load-bearing areas, and evaluate the impact of the HIP process on porosity closure in relation to specimen thickness, one representative specimen of each thickness and heat treatment condition was subjected to imaging using a commercial micro-compute tomography (µCT) system, specifi-

cally Zeiss Xradia 620 Versa. µCT has become widely accepted as an accurate method for porosity determination of AM specimens [60, 61, 62]. It is favored over alternative porosity measurement methods due to it is non-destructive nature, capacity to determining the shape and size of individual pores (provided pores are of sufficient size) [60], and ability to consider a large, statistically significant volume of the specimen in a single analysis [63]. Furthermore, µCT measurements of porosity generally agree with porosity measurements made via more conventional means [60, 62].

The µCT process involves the generation and projection of X-rays onto the specimen. Each specimen was imaged at the center of the gage section, covering an area of approximately 3.5mm^2, with image depth corresponding to the specimen's thickness. To ensure adequate X-ray transmission, operational parameters for the X-ray source were selected; for this study, a voltage of 160kV and power of 25W were employed. The X-rays travel through the specimen and are captured by a lens-coupled scintillator with 4.0× magnification, which converts the X-rays into visible light image. This image is then recorded by a charge-coupled device (CCD) detector with a physical pixel size of 2.02µm/px, yielding an overall image resolution in the range of 2000×2000 px. Once an image is captured, the specimen is incrementally rotated by a fraction of a degree to allow another image to be taken. Imaging is continued until the specimen has been rotated a full 360°, allowing the images to be stacked to create a complete 3D object and determine varying densities within the material.

3.4 Microscopy

The influence of specimen thickness on microstructure and surface topography were examine using optical and scanning electron microscopy (SEM). These techniques allow for a comprehensive comparative analysis of the specimens.

3.4.0.1 Optical Microscopy

Optical imaging was conducted using a LEICA DMi8 optical microscope equipped with Leica Application Suit X (LAS X) software. Microscopic examination encompassed capturing images in both parallel and perpendicular orientations to the build direction. This approach allowed for the documentation of distinct sections of the specimen and the assessment of microstructural variances related to thickness and heat treatment.

The specimen preparation process entailed sectioning and a sequence of polishing steps. Specimens were manually ground on 80 to 1200 grit wet SiC paper, auto polished with a water base diamond suspension on an MD Mol pad from 3 to 1µm for 5 minutes with each suspension applying 20 to 15N of force. Finally, the samples had a mirror-like finish applied using an MD Nap pad with 0.05µm colloidal silica for 10 minutes applying 10N of force. Specimens were rinsed thoroughly with cold water for several seconds, followed by an ethanol rinse to remove water impurities, and then blow-air dried. To reveal the underlying microstructure, specimens underwent etching by submersion in a kallings solution (4g $CuCl_2$, 80mL of HCl, 100mL of ethyl alcohol) for a duration of 2 to 5s. Following etching, specimens were subjected to a cold water rinse, then

an ethanol rinse to remove water impurities, and ultimately dried using heated air. Additional information on the surface preparation process can be found in [64, 65].

3.4.0.2 Scanning Electron Microscopy

The specimens used for SEM analysis underwent a similar preparation process as the specimens used for optical microscopy. However, specimens used for SEM analysis were not etched. SEM was used to document the underlying microstructure of specimens and also to investigate the internal porosity along the fracture path and the fracture surfaces of postmortem tensile specimens. SEM fractography analysis was conducted using a Hitachi S-3700N SEM, operating with a power of 15 kV, a probe current of 60 mA, and a working distance withing the range of 10 mm–11 mm from the specimen's surface.

For electron backscatter diffraction (EBSD) analysis, specimens underwent an examination aimed at investigating microstructural and crystallographic texture variations with varying thicknesses and heat treatment conditions. EBSD involves directing accelerated electrons from the SEM beam at an inclined specimen (approximately 70° relative to the normal incidence of the electron beam). These electrons are diffracted by atomic layers within the material and impinge upon a phosphorous screen, integrated with a digital frame grabber. This process generates Kikuchi bands (electron backscatter patterns (EBSP's)), which are projections of the crystal lattice plane geometry. They provide direct information about the crystalline structure and orientation of the grain from which they

originate. Digitized patterns of Kikuchi lines are processed to identify individual Kikuchi lines, facilitating phase identification and the determination of crystal orientation [66].

The EBSD analysis was conducted on an FEI QUANTA 600 F SEM, operating at 20 kV to 21 kV with a 6.0 spot size, and fitted with an OXFORD Instruments NordlysMax3 EBSD detector using a step size of 2.0µm for the analysis. Due to the sensitivity of EBSD analysis to surface preparation, to following additional steps were implemented for further specimen preparation: following the polishing procedure described in Section 3.4.0.1, optical microscopy, specimens were electropolished using a Struers Lectropol-5 at 6V for 15s with a solution consisting of 78mL of phosphoric acid, 21mL sulfuric acid, and 100mL D.I. water.

3.5 Mechanical Testing

3.5.1 Quasi-static Testing

Quasi-static mechanical testing was conducted using a servo-hydraulic Materials Testing System (MTS) machine with either a 100kN or 5kN load cell, depending on the predicted failure load for each individual specimen thickness. These predicted failure loads were calculated from ultimate tensile strength data reported in [17]. The displacement rate was set to 0.5mm/min, corresponding to strain rates on the order of $10^{-4}s^{-1}$. Tests continued until the tensile specimens reached failure. At least two tests were run for each specimen thickness and heat treatment condition to ensure the repeatability of results.

The strain was measured using digital image correlation (DIC) techniques, employing Correlated Solution's Vic 2D software. DIC was selected for these measurements due to its well established reliability in capturing surface strain when compared to traditional extensometers [67, 68, 69]. DIC, when implemented with proper speckling, imaging equipment, and lighting, provides low uncertainty in strain measurements [70]. The imaging process employed a PointGrey Grasshopper camera (model number GS3-U3-51S5M-C) with a resolution of 2448×2048 px. During the elastic deformation phase, a frame rate of 10 frames per second was used, which was reduced to 1 frame per second thereafter. Illumination of the specimens was achieved through a Cole-Parmer 41500-50 fiber optic illuminator. DIC analysis was performed with a subset size of 33 pixels and a step size of 11 pixels. Moreover, a standard deviation of the unloaded strain was determined for all specimens by capturing a series of images taken prior to loading the specimens and then calculated to be 127 $\mu\epsilon$.

3.5.2 Fatigue Testing

Fatigue tests were conducted under ambient temperature conditions and air, in accordance with ASTM E466-21 standards, using an Instron 8801 servo-hydraulic frame. The Instron frame possessed a dynamic load capacity of $\pm$100kN, an actuator stroke of 150mm (positioned at the base), and a frame stiffness of 390kN equipped with a 97.86kN fatigue rated load cell.

Tests were initiated in load control mode at a frequency of 30Hz employing a stress ratio of $R = 0.1$ and a sinusoidal waveform. Tests were continued until

reaching failure or until a total of 10^6 cycles, depending on whichever criteria was met first.

3.5.3 Cross-section Measurement

The surface topography of AM components can result in inaccurate measurements of the cross-sectional area when conducted through mechanical means, such as calipers [71, 72]. In order to better determine the effective load-bearing area of AM specimens, the cross-sectional area was measured using three different methods. The first method involved determining the cross-sectional area by measuring the gage section dimensions using Mitutoyo CD-6"-ASX digital calipers.

A second method used optical microscopy to measure the load bearing area of specimens built in the same build. However, as this is a destructive measuring method, quasi-static tests needed to be performed on different specimens. In order to measure the load bearing area using optical microscopy, the specimens were sectioned near the center of the gauge section, epoxy mounted, and imaged using an optical microscope. The load-bearing area was calculated using ImageJ software [73], which converts the image to black and white, outlines the perimeter of the specimen, and calculates the area inside the perimeter. Similar methods have been previously employed to calculate load-bearing area in AM materials [72].

As the third method, micro-computed tomography (µCT) scans were used to measure the load-bearing areas in the tested specimens. µCT scans were obtained for a segment of the gage section, approximately 10mm in length, and

processed using Dragonfly software to calculate the volume. This volume was then divided by the scanned length of the gage section segment to determine an average cross-sectional area for roughly 5/6 of the gage section. Importantly, the segmentation process involves selecting a range of pixel color values corresponding to the solid areas of the specimen, allowing for the exclusion of internal porosity from the load-bearing area calculations. While µCT scans offer the advantage of more precise cross-sectional area measurements on the exact specimens that are to be tested, the scans are associated with higher costs, and their accuracy is limited by the resolution of the computed tomography system [74].

Given the limitations associated with of these measurement methods, namely inaccurate measurements from calipers, destructive measurements from optical microscopy, and high costs associated with µCT [40]. This study examined the idea of finding a correlation between the caliper measurements and the maximum peak height, denoted Sp. For this correlation, the Sp value was subtracted from the caliper-measured dimensions. Since the Sp represents the tallest peaks on the surface, it is likely where the caliper first makes contact with the surface. Figure 3.2 displays a schematic of a cross-section of a L-PBF specimen being measured with calipers, note that the calipers make contact with the peaks of the surface, which do not necessarily represent the load-bearing area of the specimen.

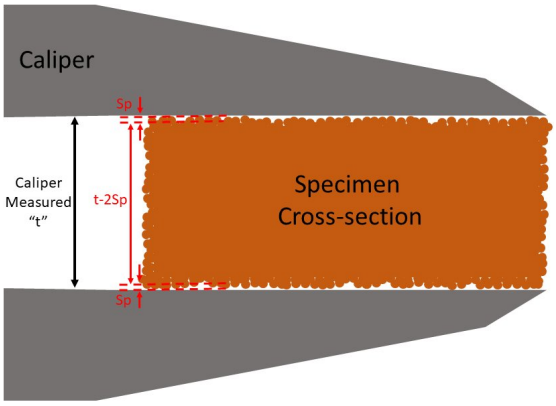

Figure 3.2: Illustrates an exaggerated schematic of a L-PBF specimen's cross-sectional area being measured using calipers. Note that calipers make contact with the highest peaks on the surface of the specimen. Thus, removing the Sp from each as-printed surface removes the highest peaks measured, approximating the value to the mean surface plane.

Furthermore, the fabrication of specimens utilizing different deposition methods, *i.e.,* L-PBF and DED, lead to different surface characteristics. In the case of DED specimens, which were EDM sectioned from single walls and had a smooth surface on cut sides, only had two as-printed surfaces. Therefore, to calculate the calibrated cross-sectional area (A_c), the Sp value was exclusively subtracted from the caliper-measured thickness (t) and then multiplied by the caliper-measured width (w), as shown in the equation below:

$$A_c = (w) \times (t - Sp) \tag{3.6}$$

This correction method yielded close approximations to the area obtained through µCT measurements and also a similar stress-strain behavior to that of polished specimens. In contrast, L-PBF specimens retained their as-printed surface conditions. Consequently, the calculation of A_c for L-PBF specimens required

a different approach, factoring in the Sp value with respect to both width and thickness. The cross-sectional area was defined with the following equation:

$$A_c = (w - 2Sp) \times (t - 2Sp). \tag{3.7}$$

Twice the Sp value is subtracted from both areal dimensions to properly account for specimen symmetry. Previous works arrived at similar conclusions, for example, Yu *et al.* [75] subtracted twice the maximum profile peak height (Rp) from the thickness prior to multiplying by the width to correct for the surface roughness. Variants of these corrective methods have been presented in other studies, c.f. [76, 77, 78].

These equations for A_c are then used to compute the calibrated stress (σ_c) experienced by the specimens during mechanical testing, as shown in the following equation:

$$\sigma_c = \frac{F}{A_c}, \tag{3.8}$$

where F is the applied force.

Chapter 4. Results

This chapter is divided into 4 sections: size effects on quasi-static behavior of L-PBF GRCop-42 (Section 4.1), size effects on quasi-static behavior on DED GRCop-42 (Section 4.2), Comparison Between Laser Powder Bed Fusion and Direct Energy Deposition of GRCop-42 (Section 4.3), and size effects on fatigue behavior on L-PBF GRCop-42 (Section 4.4). These sections were obtained from four scientific publications, given below:

- Demeneghi, G., Barnes, B., Gradl, P., Mayeur, J. R., & Hazeli, K. (2021). Size effects on microstructure and mechanical properties of additively manufactured copper–chromium–niobium alloy. Materials Science and Engineering: A, 820, 141511.

- Demeneghi, G., Barnes, B., Gradl, P., Ellis, D., Mayeur, J. R., & Hazeli, K. (2022). Directed energy deposition GRCop-42 copper alloy: Characterization and size effects. Materials & Design, 222, 111035.

- Demeneghi, G., Gradl, P., Mayeur, J. R., & Hazeli, K. (2024). Size Effect Characteristics and Influences on Fatigue Behavior of Laser Powder Bed Fusion of Thin Wall GRCop-42 Copper Alloy. Heliyon.

- Demeneghi, G., Gradl, P., Mayeur, J. R., & Hazeli, K. (2024). GRCop-42: Comparison between laser powder bed fusion and direct energy deposition. Under Review.

4.1 Size Effects on Laser Powder Bed Fusion

Specimens were fabricated with various thicknesses, including 0.7, 1.0, 1.7, and 2.0 mm, in accordance with ASTM E8/E8M standard dimensions [79], where the long axis of the specimen is parallel to the build direction as shown in Figure 4.1. This orientation was choosen to preserve the integrity of the surface topography in the gage section, as it prevents any plane of the specimen's gage section from contacting the build plate during the deposition process or contacting the electric discharge machining (EDM) wire when removing the specimens from build plate.

Specimens were manufactured using GRCop-42 pre-alloyed gas atomized powder on an EOS M400 Series printer with a Yb-fiber laser. The specimens were deposited on top of a stainless steel base plate coated with a nickel-based alloy, specifically Inconel 718. It is noteworthy that, in this study, L-PBF specimens are occasionally referred to as being in the "as-built" condition. However, these samples underwent a stress-relief (SR) process, a step necessary to remove components from the build plate without risking to distort them due to residual stresses. The stress relief procedure is performed by subjecting the specimens to a controlled environment, with heating performed at 425 °C ±25 °C for a duration of 2 hours and ±15 minutes, within a vacuum atmosphere, followed by air cooling.

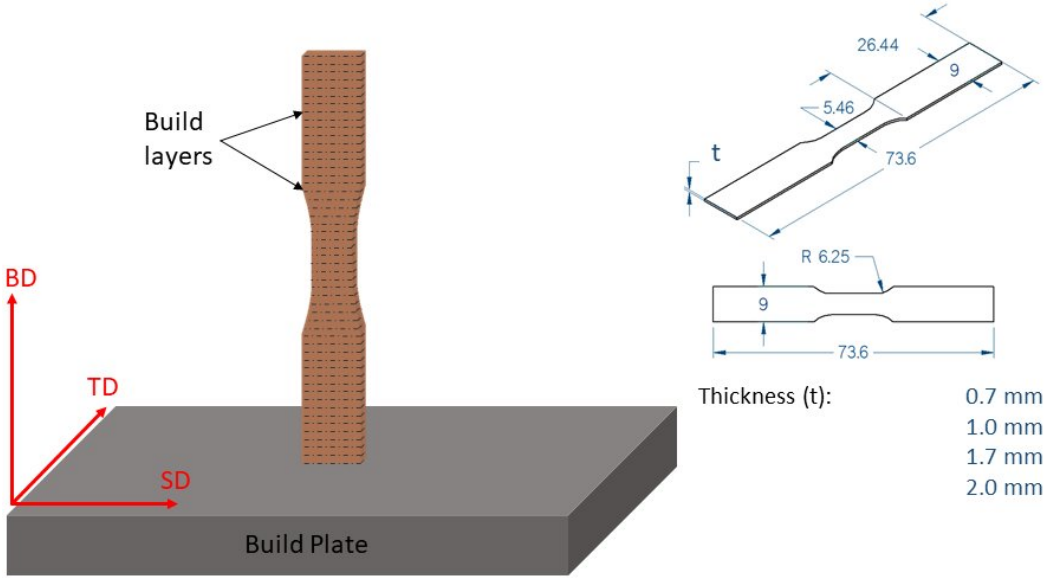

Figure 4.1: Graphical representation illustrating the spatial orientation of build direction coordinates and layer deposition with respect to the build plate. The terms Build Direction (BD), Transverse Direction (TD), and Scanning Direction (SD) are employed to demarcate distinct axes within the three-dimensional deposition process. The dimensions of the tensile specimen are shown on the right side of the figure. Note that all specimens have the same dimensions except for thickness. The thickness values for the fabricated specimens are 0.7 mm, 1.0 mm, 1.7 mm, and 2.0 mm.

4.1.1 Surface Topography

Surface topography was subjected to both qualitative and quantitative investigation, employing SEM and digital profilometer, respectively. Given the relatively small feature size associated with L-PBF deposition process, significant waviness is not expected in the process. Nevertheless, due to the presence of powder particles surrounding the component during fabrication, it is reasonable to assume that a substantial amount of partially melted and loose powder adhered to the surface. This eludes to specimens characterized by a predominantly flat yet rough surface topography. A SEM image of the specimens surface is illustrated

on Figure 4.2 and the surface topography values are presented in Table 4.1. These values include the areal average (Sa) and root mean square (Sq) from the surface analyzes.

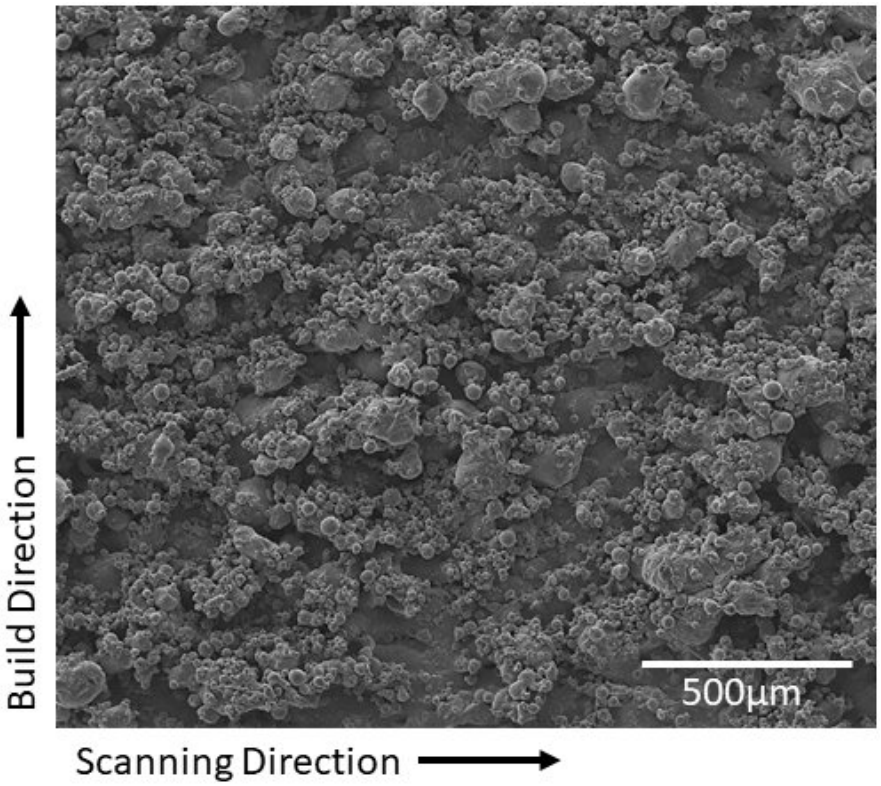

Figure 4.2: L-PBF specimen's surface obtained through SEM along with the build direction and scanning direction. A significant amount of partially melted and loose powder is observed to have adhered to the surface.

Table 4.1: Average (Sa) and root mean square (Sq) surface topography values for representative specimens.

	Sa (µm)	**Sp** (µm)
0.7mm As-built	12.660	16.099
0.7mm HIP	21.941	28.674
1.0mm As-built	17.797	23.074
1.0mm HIP	15.687	19.716
1.7mm As-built	16.935	21.518
1.7mm HIP	15.073	18.947
2.0mm As-built	15.759	20.981
2.0mm HIP	17.230	22.022

No discernible correlation was observed among the measured surface topography values, specimen thickness, or heat treatment condition. Because the measured surface topography values are similar for each thickness, it is reasonable to assume that this similarities translate into a more substantial percentage reduction in load-bearing area for thinner specimens.

4.1.2 Porosity

A volumetric analysis was conducted on one specimen of each thickness, ranging from 0.7 to 2mm, for both heat treatment conditions, employing a µCT system. Figure 4.3 illustrates a three-dimensional reconstructions from the µCT data of selected areas located on the gage section of the specimens.

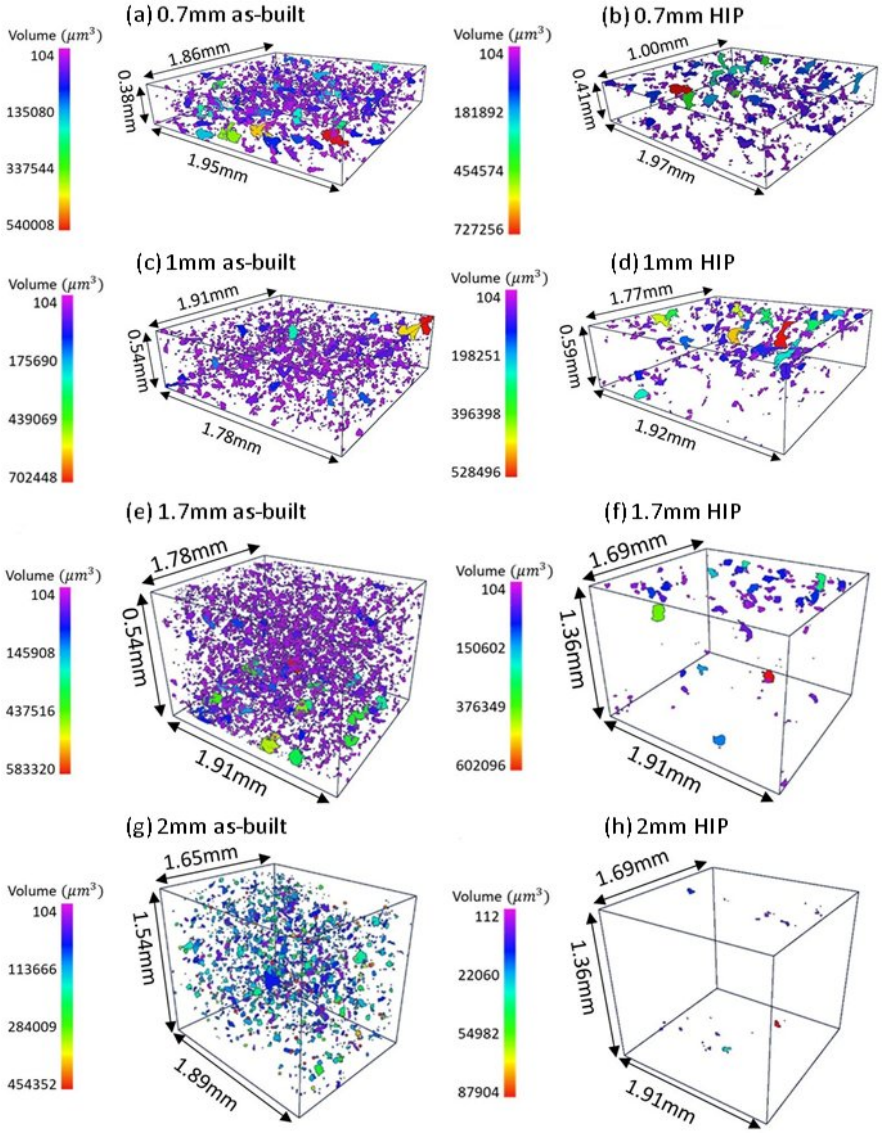

Figure 4.3: Three-dimensional reconstructions of the µCT analyses performed on varying thickness and heat treatment condition. (a) corresponds to 0.7mm as-built specimens, (b) to 0.7mm HIP, (c) to 1.0mm as-built, (d) to 1.0mm HIP, (e) to 1.7mm as-built, (f) to 1.7mm HIP, (g) to 2.0mm as-built, and (h) to 2.0mm HIP specimens. Notice that as thickness decreases, porosity increases across all specimens. Additionally, the effectiveness of HIP in reducing porosity becomes significantly more pronounced as specimen thickness increases.

The efficacy of HIP is evident as the pore volume ratio decreases by as much as 99.89% for the thicker specimens. Notably, HIP exhibited greater effectiveness in closing the smaller, interior pores as opposed to large ones or those situated near the surface. Additionally, it is worth mentioning that the reconstructions presented in this figure do not encompass the entire cross-sectional area of a specimen. Detailed data regarding the total scanned volume, pore volume, number of pores, and the percentage of pores based on the size of each specimen are provided in Table 4.2.

Table 4.2: Provides the total volume, pore volume, the total number of pores, and the percentage of different pore volumes in each representative specimen. It is evident from the results that both pore volume and the number of pores exhibited a noticeable reduction following HIP. This observation validates the effectiveness of HIP in mitigating small pores and defects on L-PBF components.

	Total Volume (mm^3)	**Total Porosity** (mm^3)	**Porosity Percentage** (%)
0.7 As-built	1.391	0.015	1.07
0.7 HIP	1.461	0.013	0.90
1.0 As-built	1.851	0.012	0.64
1.0 HIP	2.000	0.008	0.42
1.7 As-built	4.244	0.022	0.52
1.7 HIP	4.389	0.005	0.12
2.0 As-built	4.795	0.013	0.27
2.0 HIP	6.400	0.0002	0.003

The analysis reveals a trend with repect to pore characteristics in relation to specimen thickness and heat treatment condition. Thinner specimens in the as-built condition generally exhibit a lower number of pores, yet they account for a higher total pore volume. This indicates that thinner specimens contain a higher portion of larger pores compared to their thicker counterparts. The majority of pores, exceeding 90%, found in specimens, regardless of heat treatment

condition, are smaller than 100 000µm^3. Consequently, these data show that HIP significantly reduced the pore volume and the total number of pores in each specimen. A reduction in porosity through HIP aligns with findings in other AM alloys, such as Ti-6Al-4V [80], GRCop-84 [81], and Inconel 718 [82].

While no direct correlation between the total number of pores and specimen thickness could be identified, the total pore volume ratio, which is the total pore volume divided by the total scanned volume, provides valuable insights. The pore volume ration exhibited a significant decreased of 74.7%, from 1.07% pore volume in 0.7mm as-built specimens to 0.27% pore volume in 2.0mm as-built specimens. Similarly, for HIP'd specimens, the pore volume ratio experienced a decrease of 99.7%, from 0.90% pore volume in 0.7mm HIP'd specimens to 0.003% pore volume in 2.0mm HIP'd specimens. Furthermore, HIP'ing decreased the pore volume ratio by 15.89% for 0.7mm specimens, 34.38% for 1.0mm specimens, 76.92% for 1.7mm specimens, and 99.89% for 2.0mm specimens. This indicates that HIP is more effective in reducing pores as the specimen size increases.

Figure 4.4 illustrates the distribution of pore sizes relative to specimen thickness, depicting the frequency of pores within specific volume ranges.

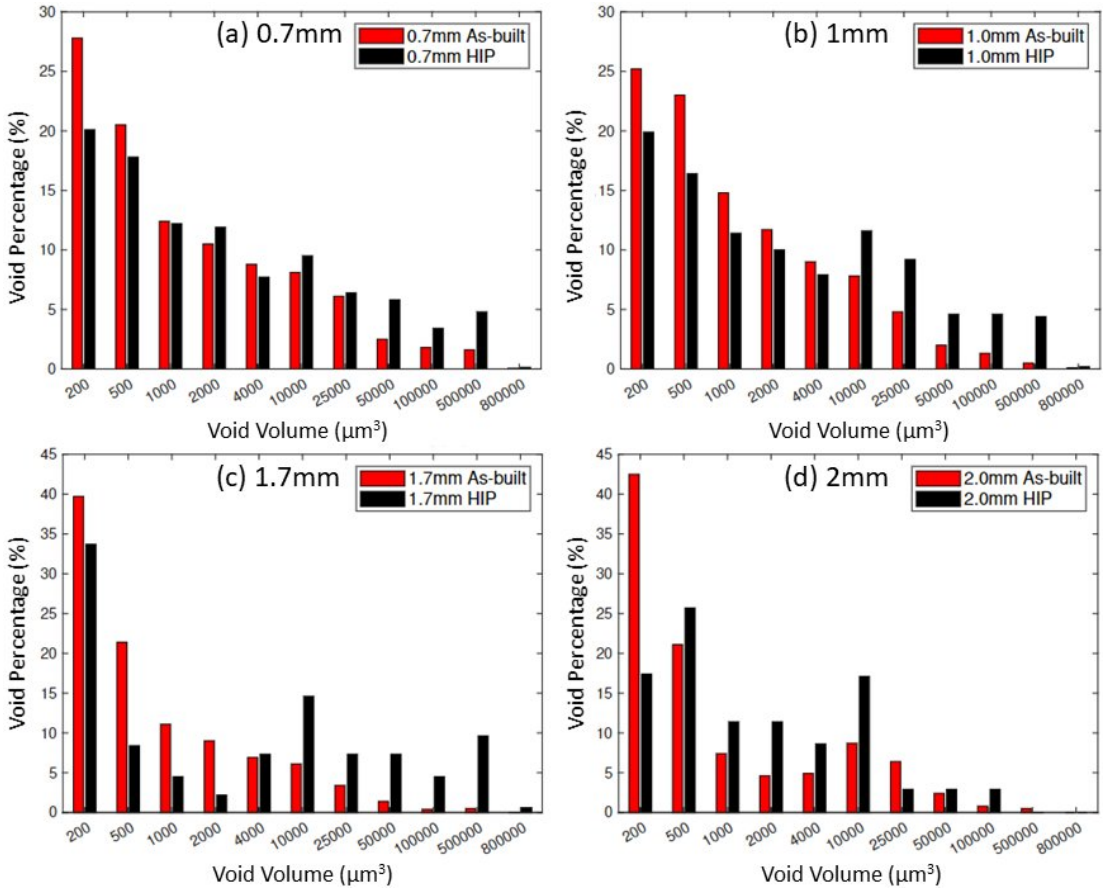

Figure 4.4: Frequency of pore size of a given volume in relation to specimen thickness ((a) for 0.7mm, (b) for 1.0mm, (c) for 1.7mm, and (d) for 2.0mm) and heat treatment condition. It is evident the majority of pores in all specimens are smaller than 1000µm^3. Furthermore, these charts demonstrate that HIP is most efficient at reducing smaller pores, resulting in larger pores comprising a higher percentage of the total in HIP'd specimens. Finally, it should be noted that small pores with volumes less than 200µm^3 constitute a considerably larger portion of the total pores in the thicker specimens as compared to thinner ones.

While the majority of pores in the as-built specimens are smaller than 1000µm^3, there is a noticeable shift in the overall distribution towards larger pores in the thinner specimens. Moreover, the data presented in these plots highlight

that HIP is most effective at reducing smaller pores, leading to a shift in the distribution of pores towards larger sizes in the HIP'd specimens.

Thinner specimens generally exhibit a higher pore volume, predominantly consisting of larger pores, resulting in a higher pore volume ratio. Note that pores with volumes smaller than 200µm^3 are more prevalent in thicker specimens, accounting for approximately 40% of the total pores in 2.0mm and 1.7mm specimens, while thinner specimens (1.0mm and 0.7mm) exhibit only around 25% of pores within this size. Furthermore, HIP'd specimens demonstrate a reduction in both pore volume and the number of pores, proving the efficacy of the heat treatment. However, it should be noted that the percentage of smaller pores decreases while the percentage of larger pores increases in all specimens, indicating that HIP is efficient in closing small pores but has little effect on larger pores.

4.1.3 Microstructure

The microstructure of all specimens was analyzed through optical microscopy and EBSD. This was done to investigate changes in the grain morphology, grain size, and crystallographic texture between different thicknesses or heat treatment conditions.

4.1.3.1 Grains

The grain structure analysis was conducted in the SD-TD plane, perpendicular to the build direction. EBSD maps were configured with a grain detection angle of 12° and at least 5 pixels per grain. The selection of a high grain detec-

tion angle was motivated by the unique "melted" grain structure present in these specimens, where a high detection angle enhances the visual clarity of the grain analysis. In Figure 4.5, EBSD maps in the ST-TD plane, perpendicular to the build direction, are presented to assess the influence of different solidification conditions on different thicknesses. Figure 4.6 provides the percentage distribution of grains sizes for specimens with different thicknesses and heat treatment condition.

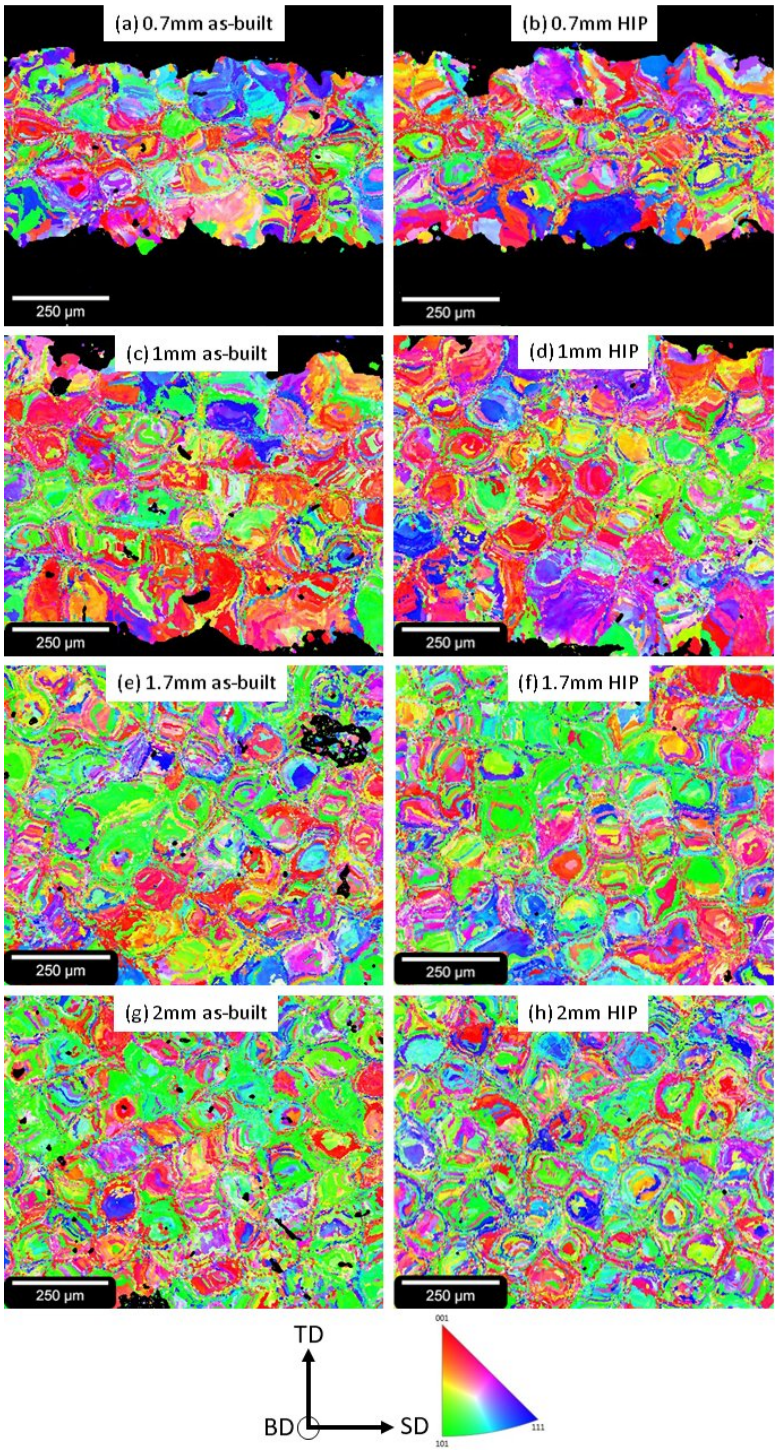

Figure 4.5: The grain structure perpendicular to the build direction are presented for all specimens. In the left column, the as-built specimens are presented as follows: (a) - 0.7mm, (c) - 1.0mm, (e) - 1.7mm, (g) - 2.0mm. In the right column, the HIP'd specimens are depicted: (b) - 0.7mm, (d) - 1.0mm,(f) - 1.7mm,(h) - 2.0mm.

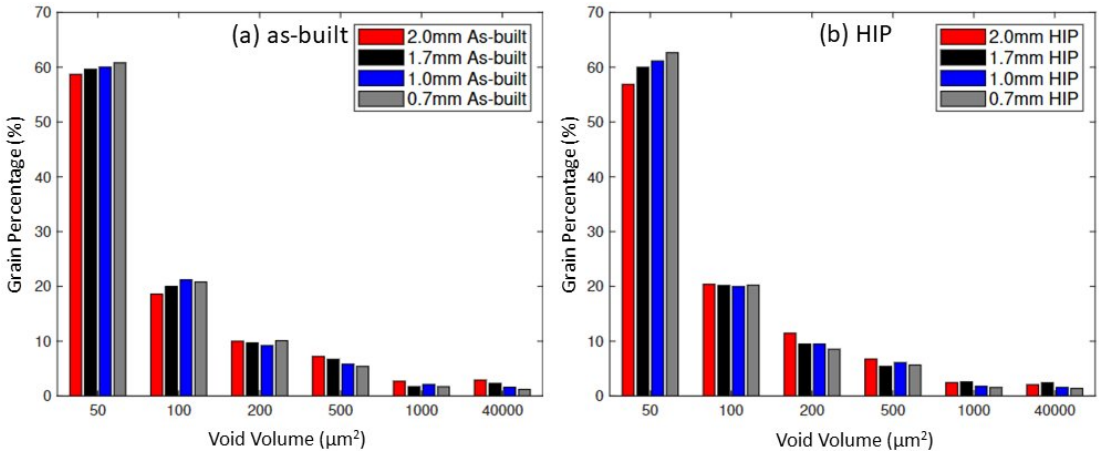

Figure 4.6: Percentage distribution of grain sizes within the gage section of a representative specimen for each thickness and heat treatment condition. (a) shows the as-built specimens and (b) shows the HIP'd specimens. It is evident that the distribution of grain sizes remains relatively consistent across varying thicknesses and heat treatment conditions, displaying minimal changes.

No appreciable difference in microstructural characteristics is observed between the as-built and HIP'd specimens. Across all specimen thicknesses, a fine grain size is consistently present, which is typical of the L-PBF process owing to its rapid solidification rate [83]. Where the average grain size for all specimen thicknesses corresponds to approximately ASTM grain size 11. Notably, the majority of grains, approximately 94%, are smaller than 300µm^2. Specifically, within this range, 57 to 63% are smaller than 50µm^2, 18 to 20% fall within the 50 to 100µm^2 range, 10% within 100 to 200µm^2, and 3 to 4% within 200 to 300µm^2. The remaining percentage of grains encompasses various larger grain sizes.

The consistent grain size across different specimen thickness implies a uniformity in grain distribution throughout the specimen cross-section. This homogeneity results in a reduced number of grains across the specimen as thickness is

reduced, which, in turn, contributes to a decreased toughness as grain boundaries serve as hindrance to dislocation movement and crack propagation [34].

4.1.3.2 Texture

The grain structure morphology and crystallographic texture were investigate using EBSD analysis conducted on the BD-SD plane, which is parallel to the build direction. Figure 4.7 illustrates the EBSD maps of the 0.7 mm, 1.0 mm, 1.7 mm and 2.0 mm specimens in both the as-built (left) and HIP'd (right) conditions.

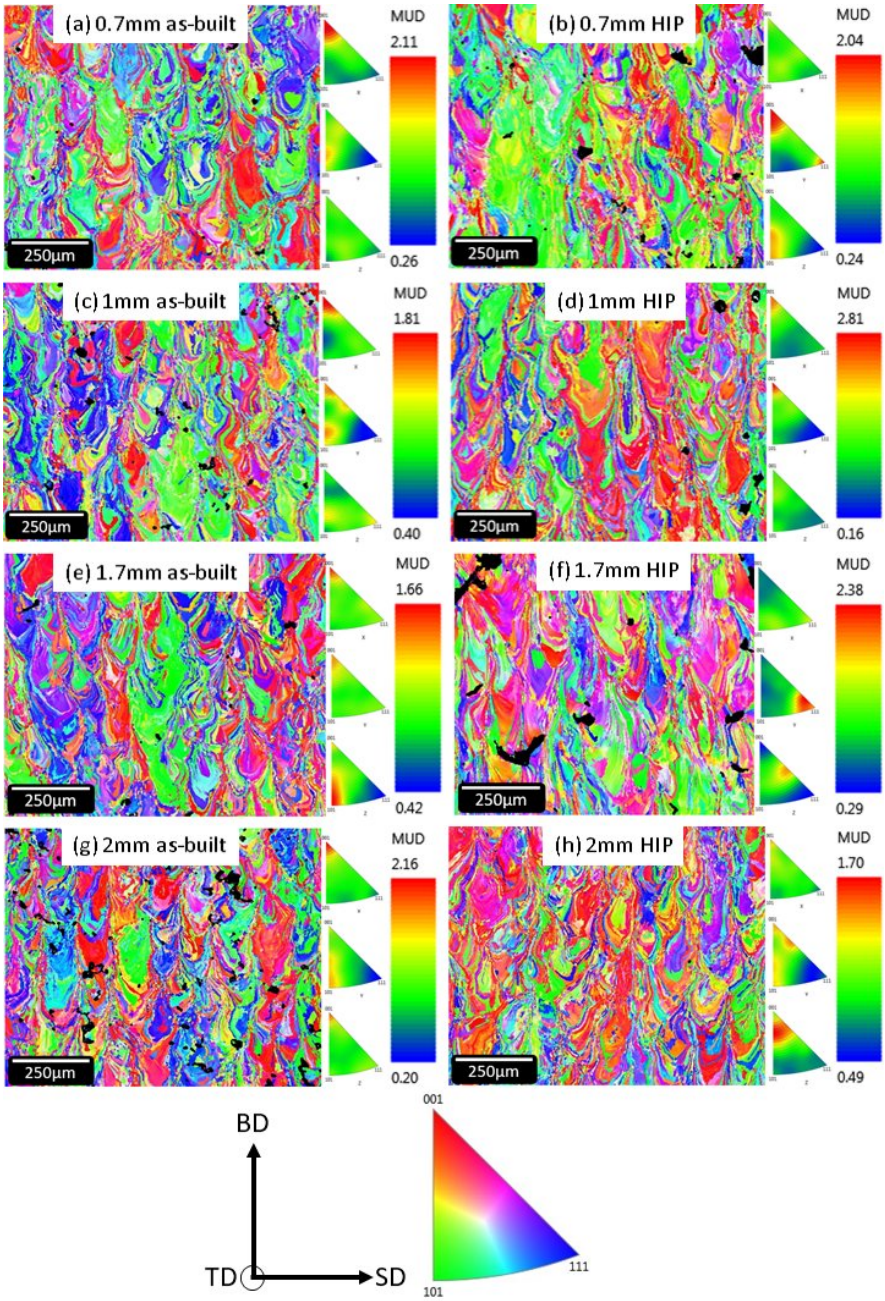

Figure 4.7: Microstructure parallel to the build direction of one specimen of each thickness in both as-built and HIP conditions. The left column displays the microstructures of as-built specimens, corresponding to (a) 0.7mm, (c) 1.0mm, (e) 1.7mm, (g) 2.0mm). The right column exhibits microstructures of HIP'd specimens, representing (b) 0.7mm, (d) 1.0mm, (f) 1.7mm, (h) 2.0mm.

The EBSD maps reveal a common occurrence in AM processes, where grains exhibit epitaxial growth from one layer to the next due to the re-melting of the previously solidified layers [84]. This phenomenon leads to the elongation of grains along the build direction [85, 86] due to the higher rate of heat conduction in the previously solidified layers compared to the build powder. The grain morphology for L-PBF GRCop-42 specimens displays distinctive hatch patterns resulting from the laser's scanning path. This is in stark contrast to extruded GRCop-84 [87, 88, 89], which typically exhibits an equiaxed copper grain structure. Additionally, there was no substantial variations in microstructure observed across different specimen thicknesses or heat treatment conditions. The similarities in grain structure among specimens of varying thicknesses are consistent with results found for Inconel 718 [72], 316L stainless steel [71], and Cu−Cr−Zr−Ti [12]. It is noteworthy to mention that Popovich *et al.* [12] also reported no morphology changes after heat treatment, aligning with the results of the present here.

To quantify the crystallographic texture, the inverse pole figure (IPF) multiples of uniform distribution (MUD) number, which measures the texture orientation density (a MUD of up to 1 corresponds to random texturing [90]) is shown at the right of each sub-figure of Figure 4.7. Mild crystallographic texture variations were noted with increased specimen thickness and heat treatment, but the overall intensities of specific texture components remained relatively weak. The observed random internal texture is consistent with findings reported in [91], where it attributed to the re-melting of subsequent solidified layers and the 90° scan rotation

strategy. Moreover, an investigation into the L-PBF Cu-15Sn bronze revealed a maximum texture intensity of only 2.3, indicating weak texture of the $< 111 >$ direction along the build direction [83]. Additionally, a study conducted across several thicknesses of additive manufactured 316L stainless steel [71] found no discernible difference in texture among different specimen sizes.

Although the IPF maps indicate a slight increase in density along the $< 101 >$ orientation on the Z IPF map for 1.7 mm and 2.0 mm specimens, the change in the MUD number is relatively low, signifying only weak texture. Furthermore, the MUD number remained similar between as-built and HIP'd specimens. This variation is presumed to be inherent to the deposition process rather than HIP'ing. Consequently, regardless of specimen thickness, HIP'ing does not induce significant alterations in the texture of AM GRCop-42 specimens.

4.1.4 Quasi-Static Test

In order to calculate engineering stress-strain curves for the tested specimens, the cross-sectional area of the specimens should be accurately determined. This section presents stress-strain curves for representative specimens, each based on cross-sectional area measurements obtained through three distinct methods: calipers, optical microscopy, and µCT scans.

Caliper measurements offer a fast and cost effective approach. However, due to the surface topography inherent to L-PBF deposition method, calipers tend to over-estimate the cross-sectional area. This occurs because calipers measures only the outermost extent of the cross-section, disregarding the intricate surface

topography characterized by peaks and valleys, which fully define the tue load-bearing area.

Optical microscopy, provides a more comprehensive view of the surface topography, thus, offering a superior means of cross-sectional area measurement. However, the same pristine specimen cannot be used for both testing and measurement. While it may be reasonable to assume that specimens from the same build batch exhibit a similar cross-sectional area, optical microscopy provides, at best, an estimation rather than an exact measurement.

In contrast, cross-sectional areas measured using µCT scans prove to be the most accurate representation of the actual load-bearing area of the specimens. µCT accounts for surface topography while remaining non-destructive. However, it is important to note that µCT scans are costly. Consequently, it is the preferred choice when precise assessment of the load-bearing area is necessary and when accommodating the inherent surface topography associated with AM is crucial.

Figure 4.8 presents representative quasi-static tension behavior data for specimen of varying thicknesses and heat treatment conditions. The stress calculations were obtained from area measurements made through the three methods described above.

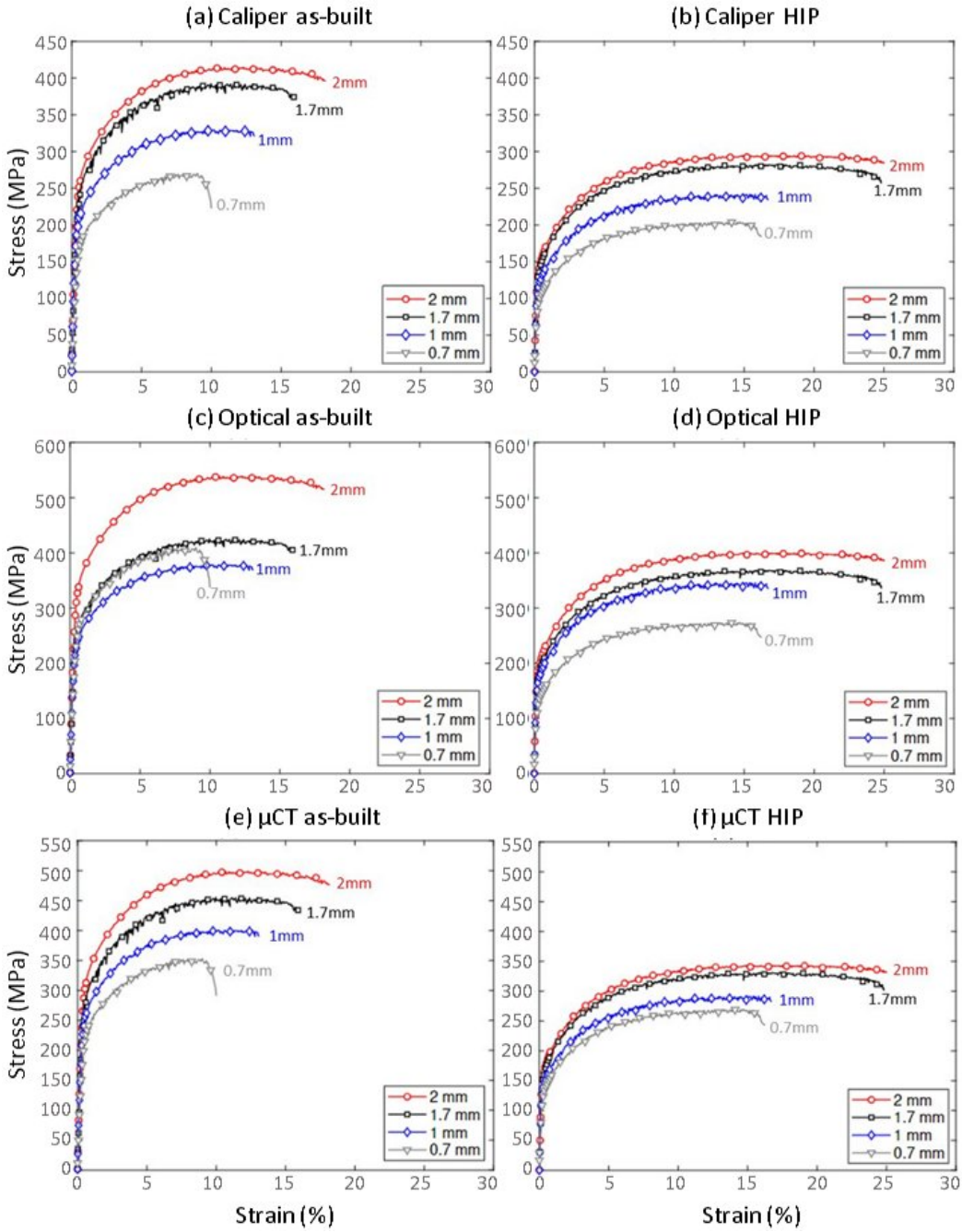

Figure 4.8: Representative stress-strain curves for each specimen thickness and heat treatment condition with the cross-sectional area measured with a caliper, optically, and µCT. (a), (c), (e) depicts stress strain curves for as-built specimens employing caliper, optical, and µCT measurements, respectively. While (b), (d), and (f) displays stress strain curves for HIP'd specimens using caliper, optical, and µCT measurements, respectively. A discernible trend of decreasing tensile strength with decreasing specimen thickness can be seen in both the as-built and HIP conditions.

Consistent with previous investigations [17], the application of HIP to GRCop-42 specimens results in a substantial reduction in both YS and UTS, accompanied by an increase in elongation. Moreover, a notable decline in YS, UTS, elongation and young's modulus is obsered as the specimen thickness decreases, regardless of cross-sectional area measurement technique. When employing caliper measurements, as shown in Figure 4.8 (a) and (b), a sizeable decrease in properties is evident. This is partially due to inaccuracies inherent of cross-sectional area measurements from calipers. The overestimation of the cross-sectional area becomes more pronounced as the specimen thickness decreases, owing to a higher surface topography to volume ratio characteristic of thin-wall specimens.

Optical cross-sectional area measurements, depicted in Figure 4.8 (c) and (d), also exhibit a general trend of decreasing strength with decreasing specimen thickness. However, this trend appears less pronounced for as-built specimens in the as-built. It is important to note that these values are likely not an accurate representation of the actual material properties due to limitations in measuring cross-sectional areas using optical microscopy.

µCT scan area calculations, illustrated in Figure 4.8 (e) and (f), yield the most accurate load-bearing area values among the presented options. It demonstrates that, for both heat treatment conditions, while a decreasing trend in strength with decreasing specimen thickness persists, the percentage decrease in UTS between successive specimens with decreasing thickness is less pronounced compared to UTS calculated based on caliper-measured area.

Table 4.3 displays the cross-sectional area ratio obtained by comparing measurements acquired via calipers and µCT scans, accompanied by its impact on the YS and UTS of the specimens.

Table 4.3: Discrepancy in specimen cross-sectional area measurements obtained via calipers as specimen thickness decreases. The area ratio represents the specimen area measured with calipers divided by the specimen area measured with µCT. The YS and UTS reported here are averages derived from all specimens of a given thickness and heat treatment condition.

		YS (MPa)		**UTS (MPa)**	
	Area Ratio	**Calipers**	**µCT**	**Calipers**	**µCT**
0.7mm As-built	1.307	176 ± 5.0	230 ± 6.5	270 ± 5.7	353 ± 7.4
0.7mm HIP	1.321	102 ± 2.0	135 ± 2.7	199 ± 6.3	263 ± 8.3
1mm As-built	1.216	207 ± 2.0	252 ± 2.4	305 ± 3.3	399 ± 4.0
1mm HIP	1.206	120 ± 3.5	145 ± 4.2	238 ± 8.2	287 ± 9.9
1.7mm As-built	1.160	245 ± 0.4	284 ± 0.5	391 ± 1.4	454 ± 1.7
1.7mm HIP	1.173	141 ± 2.0	165 ± 2.4	282 ± 5.0	331 ± 5.9
2mm As-built	1.203	255 ± 1.8	307 ± 2.2	413 ± 2.0	497 ± 2.4
2mm HIP	1.165	149 ± 2.5	173 ± 2.9	297 ± 1.5	346 ± 1.8

Considering the ratio between the cross-sectional area measurements obtained through calipers and µCT, it becomes evident that the accuracy of measuring specimen dimensions with calipers diminishes as the specimen thickness decreases. Consequently, this leads to increasingly less accurate calculations of

YS and UTS. In both the as-built and HIP'd specimens, the error in caliper cross-sectional area measurement ranges from 16 to 20% for 2mm specimens. However, this error increases to more than 30% for both heat treatment conditions in 0.7mm specimens. Due to the surface topography inherent to AM components, calipers are unable to accurately determine cross-sectional area, and particularly great care must be taken in determining the cross-sectional area of thin-wall specimens with as-printed surface topography conditions.

To investigate whether surface topographical features induce premature failure in thin-wall specimens by creating stress concentrations, two as-built and two HIP'd specimens printed with a 2mm thickness were machined and polished to a thickness of 1.9mm, eliminating the rough surface finish. These specimens were then tensile tested under the same conditions as the as-printed specimens. Figure 4.9 provides the engineering stress-strain curve for both as-built and HIP'd specimens with the as-printed surface and polished surface.

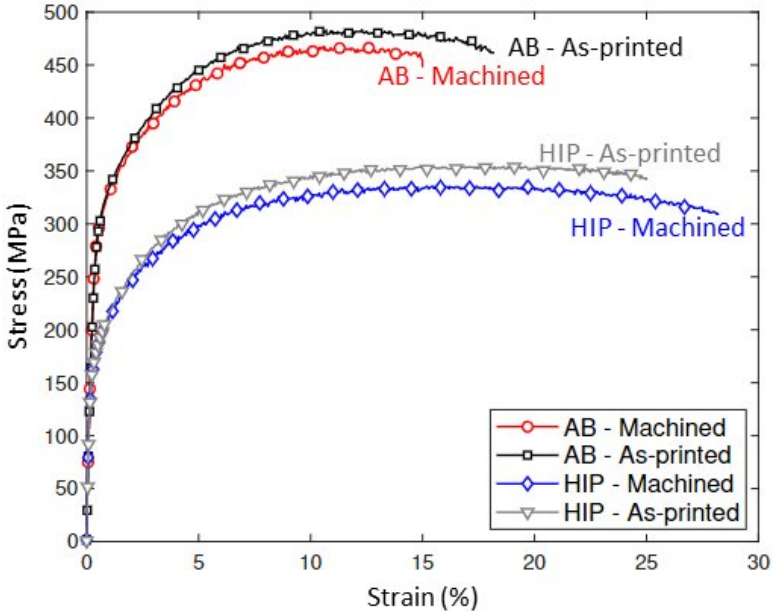

Figure 4.9: Representative stress-strain curves for both as-built and HIP'd specimens in two surface finish conditions: as-printed and machined. The magnitude of the flow stress of the two surface finish conditions exhibits a difference of less than 6%. Notably, the slighly higher flow stress is observed in the as-printed specimens. This observation suggests that the surface topography does not induce substantial stress concentrations that would adversely affect the material properties.

It is observed that the YS and UTS of the polished specimens are within 6% of the as-printed 2mm specimens. This comparison is based on stress calculated using the load-bearing area measurements obtained from µCT scans. This indicates that the surface topography of the specimens investigated in this study exerts a negligible influence on the formation of detrimental stress concentrations under monotonic tensile loading conditions.

4.1.5 Fractography

Internal porosity appears to exert a more pronounced influence on the observed size effects over microstructure or surface topography, specifically on the reduction in strength and elongation with decreasing specimen thickness. To identify the role of internal porosity in fracture surface, fractography was performed using SEM perpendicular to the fracture plane. This analysis aimed to establish a correlation between the internal porosity and the propagation path of the crack network. The fractured specimens were prepared by polishing them perpendicular to the loading direction and analyzed to ascertain whether there is a causal relationship between internal porosity and the strength decrease observed in the tensile tests.

Figure 4.10 displays specimens with thicknesses of 0.7 mm, 1.0 mm, 1.7 mm and 2.0 mm, in both the as-built and HIP'd conditions, highlighting the differences in the fracture patterns.

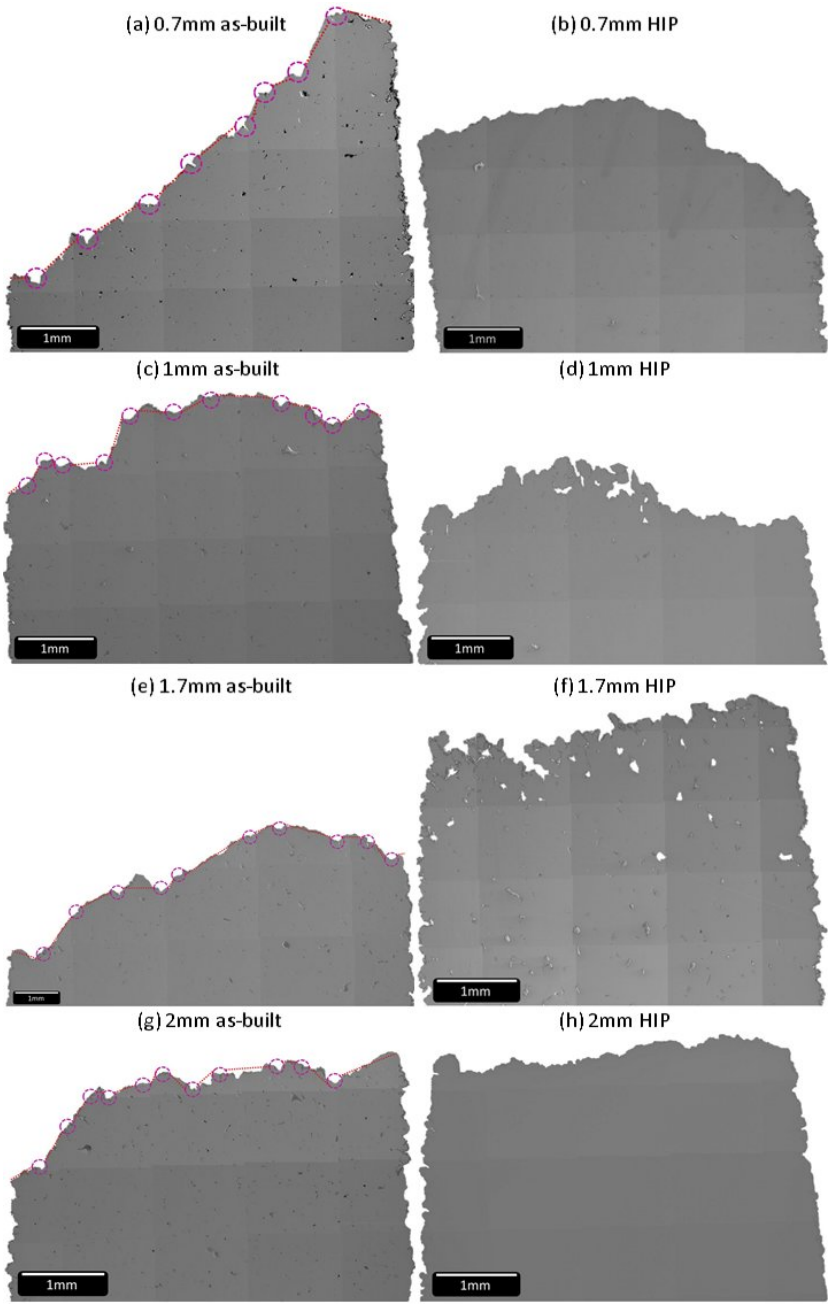

Figure 4.10: Fractography analysis was conducted perpendicular to the fracture plane. Figures to the left ((a) - 0.7 mm, (c) - 1.0mm, (e) - 1.7mm, and (g) - 2.0mm) depict specimens in the as-built condition, while figures to the right ((b) - 0.7mm, (d) - 1.0mm, (f) - 1.7mm, and (h) - 2.0mm) represent HIP'd specimens. The circles in the figures indicate pores along the fracture surface, from which internal cracks propagated.

The SEM images reveal no discernible evidence of crack initiation stemming from surface topography features, such as peaks and valleys. Instead, the cracks appear to propagate between internal pores, forming the fracture surface. This observation contradicts the findings of previous studies [71, 92, 93], which have suggested that surface topography leads to stress concentrations in thin-wall specimens, decreasing the strength. Notably, among these studies, only Algardh *et al.* [93] provided numerical values for the magnitude of surface roughness. The lineal surface roughness (Ra) reported in [93] for each specimen was within the range of 30 to 50µm, which is significantly higher than Ra values measured in the present study. Given that the magnitude of stress concentrations depends upon the magnitude of surface roughness [94], the relatively low surface roughness of the specimens in this study may be insufficient to induce significant stress concentrations.

As expected based on the µCT scan results, the as-built specimens exhibit a higher frequency of pores, which make it easier to observe the interconnected pores along the fracture path. The higher porosity in thinner specimens appears to be a key factor contributing to the decrease in mechanical properties. This is supported by SEM imaging in Figure 4.10, which demonstrates that crack networks propagate between internal pores along the fracture surface, rather than multiple isolated cracks originating from surface topography features. Such surface topography-induced cracks has been observed in high cycle fatigue situations [95]. Furthermore, porosity has been repeatedly determined to be responsible for

reduced mechanical properties, including tensile strength and elongation, in AM components [96, 97, 24, 98].

It worth noting that while the HIP'd specimens exhibited lower porosity than the as-built specimens, HIP'd specimens also have a lower yield and ultimate tensile strength. This reduction in tensile strength of HIP'd specimens has been attributed to the relief of residual stresses during the HIP process, as a decrease in tensile strength has been associated with residual stress relief in other L-PBF metals [99]. However, this has yet to be investigated explicitly for GRCop alloys.

4.2 Size Effects on Direct Energy Deposition

The DED specimens were fabricated with GRCop-42 pre-alloyed gas atomized powder via an RPMI 222 machine, employing an infrared laser. The laser's spot size was adjusted according to the desired thickness of each specimen. A back and forth striping deposition strategy was employed to fabricate four multi-panel build boxes with thin walls on an A36 mild steel build plate. The wall sets were fabricated with two distinct thicknesses that could be consistently deposited throughout the build process; 1.2 mm (T1), and 1.6 mm (T2). These specimens also exhibited variations in powder compositions. For each thickness, where two different Cr/Nb ratios were employed: 1.08 Cr/Nb ratio (C1) and 1.14 Cr/Nb ratio (C2). Accordingly, a naming convention was adopted for the specimens, corresponding both thickness and powder composition, yielding the following designations: T1C1, T2C1, T1C2, and T2C2.

Figure 4.11 depicts an illustration of a single build wall, the locations of specimen sectioning, the delineation of build layers, and dimensions of the tensile specimens and wall thickness. Specimens were designed by adapting the ASTM E8 standards to accommodate their unique thickness and length requirements. Subsequently, EDM was employed to extract the specimens from each set of walls, both in vertical and horizontal orientations with respect to the build direction. Specimens were sectioned from the center of the walls to prevent testing specimens that had interactions with the build plate during fabrication. Furthermore, the orientation is displayed on this figure with respect to the build direction (BD), scanning travel direction (SD), and transverse direction (TD). Specifically, the BD-SD plane corresponds the flat area of the specimens, the BD-TD plane illustrates the lateral cross-section across the thickness, and the SD-TD plane corresponds to a top down cross-section across the thickness.

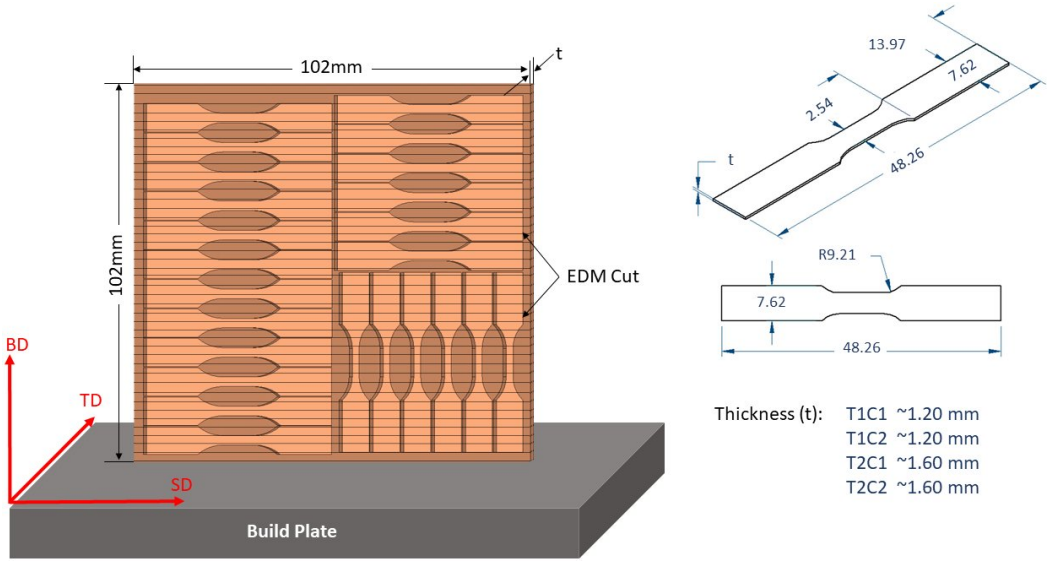

Figure 4.11: Build direction and specimen dimensions. The component was deposited as a set of single wall from which tensile specimens were removed using EDM. Two nominal thicknesses, T1 (1.2 mm) and T2 (1.6 mm), and two powder compositions, C1 (1.08Cr/Nb ratio) and C2 (1.14Cr/Nb ratio), were employed in the component fabrication process.

4.2.1 Surface Topography

A comprehensive surface topography analysis was conducted on each batch of deposited wall to assess and investigate features that may trigger deformation and eventual fracture. Moreover, the specimens' surface was imaged using SEM at a lower magnifications to document the morphology, defects, and powder adhesion. The build boxes were deposited by melting one layer on top of another, resulting in a macro waviness on the deposited components' surface, a phenomenon referred to as the "layering effect" in this study. It is important to note that the layering effect can induce anisotropic behavior, particularly in the case of thinner single-bead width walls. It is worthwhile to mention that surface topography encompasses various aspects, including overall form, waviness, and roughness.

A distinction between surface roughness and surface waviness is made to clarify the features that impact the performance of the specimens under uniaxial loading, with a 80µm low-pass filter (λ_c) being applied to the surface measurements to derive the waviness profile. Surface roughness is characterized by smaller and closely spaced irregularities (chaotic powder adhesion to the surface) resulting from the excess powder not captured in the melt pool or ejected from the melt pool. The surface waviness characterizes more regularly spaced layers [100, 101]. A form correction was applied to "flatten" the surface to avoid deformation of the specimens within the measurement. Figure 4.12 illustrates a diagram of a deposited DED single-track wall specimen, with the deposited layers and interlayers indicated by blue arrows. It also includes an SEM image showing the surface of a specimen.

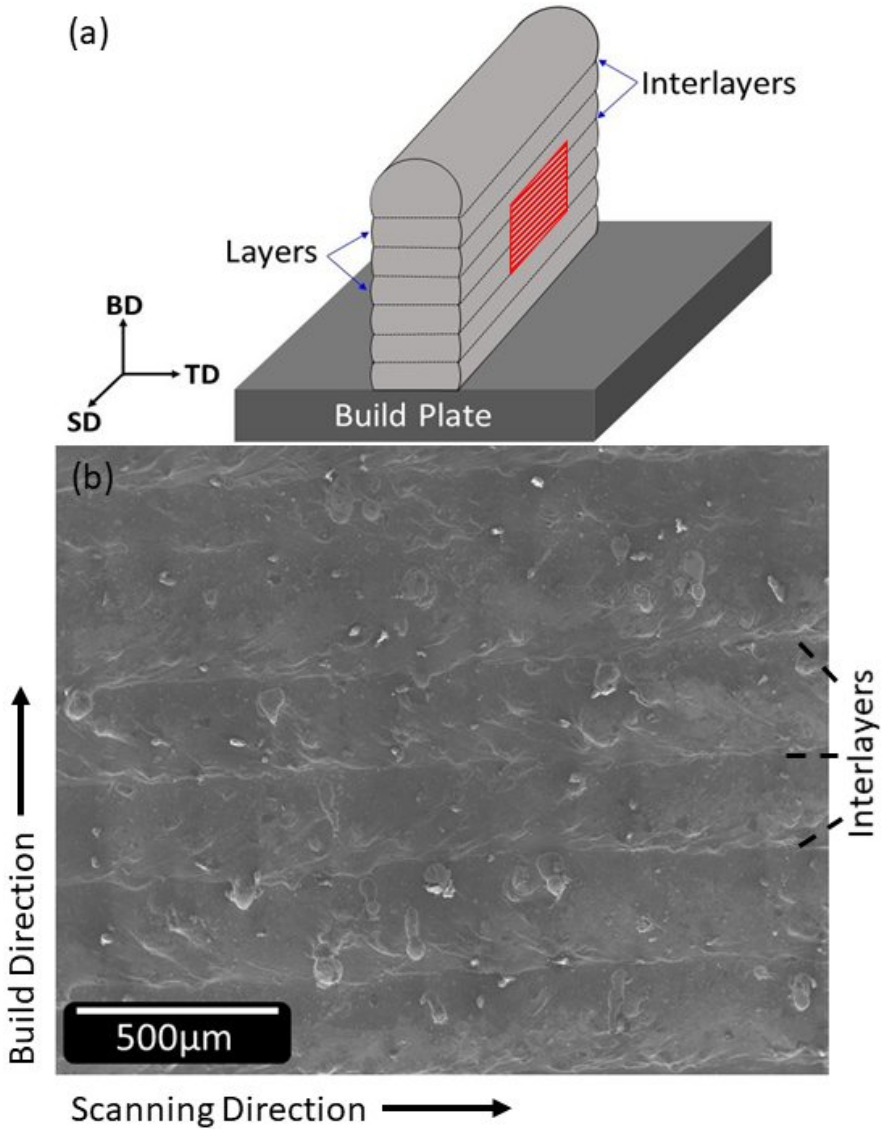

Figure 4.12: Illustrates (a) schematic representation of the cross-section of the build, featuring exaggerated layers and their interlayers, with a red box to highlighting the build layers, and (b) as image depicting the surface of an as-printed specimen at the location indicated by the red box is on part (a). Given the lack of significant variations in surface morphology among the specimens, only one specimen's surface is displayed.

Table 4.4 shows each deposited wall's areal surface topography measurements. Two specimens were randomly selected from each built wall for measure-

ments, and the results were averaged, with the standard deviation provided for each measurement. The reported values include the arithmetical mean height of an area (Sa), root mean square height (Sq), maximum peak height (Sp), maximum valley depth (Sv), maximum height (Sz), and average measurement area for each deposited wall. Aerial surface topography measurements exhibited minimal variation across specimens within the same measurement category, indicating that there was little influence from the build thickness or powder composition.

Table 4.4: Measured values obtained from the surface analysis and the average measured area per specimen. Notice that there is little variation between the specimens in any given measurement.

	Sa (µm)	**Sq** (µm)	**Sp** (µm)	**Sv** (µm)	**Sz** (µm)	**Area Size** (mm^2)
T1C1	13.2 ±1.5	18.4 ±2.2	106.3 ± 17.3	84.0 ±22.4	190.3 ±5.2	10.3
T1C2	13.3 ±0.1	16.1 ±2.2	84.0 ±6.8	70.8 ±24.2	154.8 ±18.4	10.0
T2C1	12.9 ±1.8	16.9 ±0.0	97.3 ±6.0	61.0 ±3.7	158.2 ±9.6	10.4
T2C2	12.6 ±0.2	17.2 ±0.1	98.4 ±6.9	58.9 ±4.4	157.3 ±2.5	10.0

The surface topography exhibited consistent characteristics across all specimens, with the build layers being discernible independent of build thickness or powder composition. Additionally, no noticeable defects and minimal powder adhesion were observed in the examined areas, as seen in Figure 4.12. It is important to note that this deposition method did not yield a uniform thickness throughout the entire build height; instead, it resulted in smaller areas situated between the

deposited layers, the interlayers. These interlayers feature pronounced valleys, which can lead to stress concentrations and facilitate crack initiation. A profile analysis of the deposited walls is presented in Figure 4.13. An 80µm low-pass filter was also applied to discriminate the waviness data from areal surface roughness. The analysis was conducted on an average of 51 profile lines within the measured area.

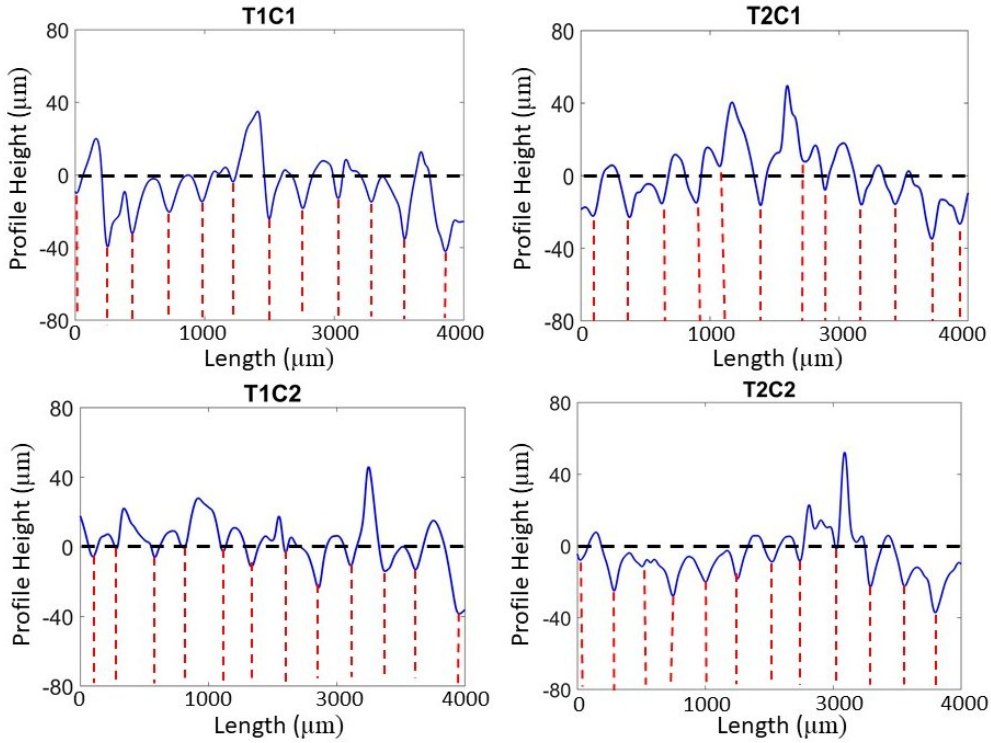

Figure 4.13: Waviness profile of the surface of each deposited wall.

The surface topography remains consistent across all specimens, independent of thickness or composition. This uniformity in surface topography, while specimen thickness varies, translates into a reduced percentage of the cross-sectional area serving as load-bearing area as specimen size decreases. Brown

et al. reported a similar phenomenon in their study on L-PBF 304L stainless steel and electron beam melting Ti-6Al-4V, where a decrease in mechanical properties was noticed when the component thickness was reduced, attributing this reduction to smaller load-bearing area and the presence of stress concentrations on the surface [92].

Moreover, the interlayers, displays is characterized by sharp valleys highlighted here using red dashed lines in Figure 4.13, while the layer peak is rounder. Sharp valleys can be regarded as notches in the specimens, which have the potential to generate stress concentrations and subsequently reduce the total elongation of the specimen. These findings align with previous research by Roach *et al.* [71], which identified surface roughness as a stress concentration capable of initiating deformation and fracture of specimens. Additionally, Arola *et al.* demonstrated that the magnitude of stress concentrations on machined surfaces correlates with the magnitude of the surface roughness [94]. This implies that the observed surface topography can significantly influence the mechanical response of the specimens under uniaxial loading, with potentially greater effects on thinner specimens.

4.2.2 Porosity

One specimen from each batch of deposited walls was randomly selected for µCT scanning to quantitatively assess the internal porosity. Porosity is a well known concern in AM alloys, and although it can be mitigated to some extent through HIP, it is not completely eliminated and can adversely affect mechanical

properties [40, 96, 57, 98, 24]. Therefore, it is imperative to quantify the porosity resulting from specific manufacturing processes, build thicknesses, and powder compositions.

Figure 4.14 provides a visual representation of the µCT scans, presenting a three-dimensional construct of the scanned volume, featuring information about the location, shape, and size of the pores. Notably, the pores are color-coded according to their volume, as indicated by the color bar accompanying each illustration. Table 4.5 displays the total scanned volume, total volumetric porosity, and the total percent porosity found in each specimen. Note that porosity is virtually negligible in all specimens. Although there appears to be notably less porosity in the thicker specimens (T2C1 and T2C2), the overall porosity in all specimens can be deemed insignificant, thus rendering the specimens fully dense.

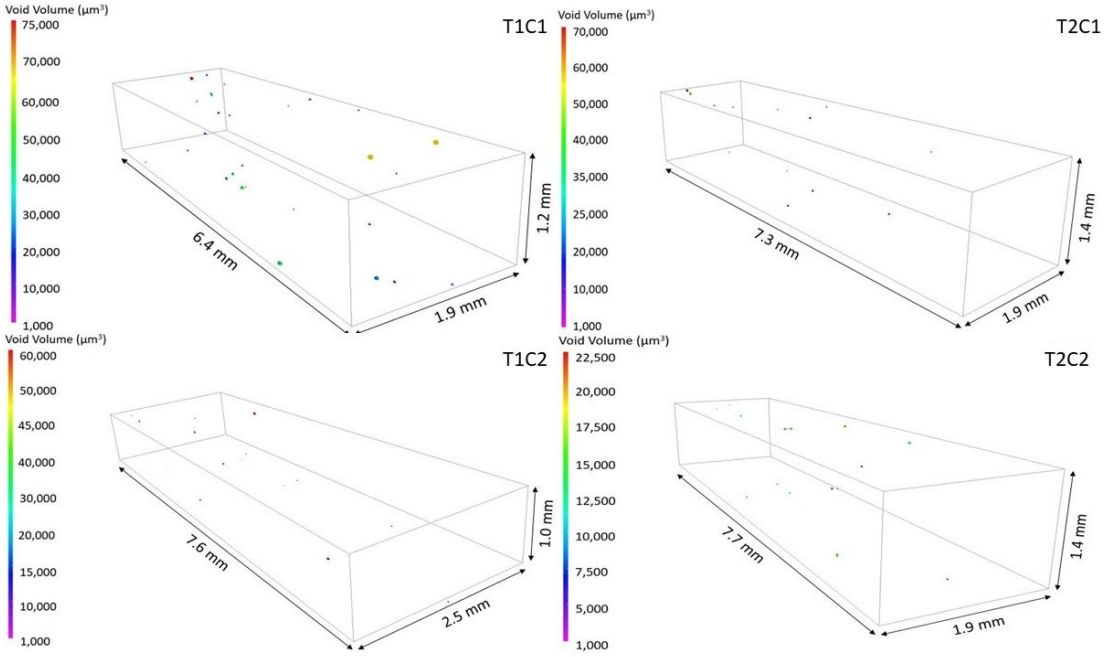

Figure 4.14: Three-dimensional reconstruction for the µCT scans of representative specimens from each build.

Table 4.5: Total scanned volume, total porosity, and the percentage porosity for each build.

	Total Volume (mm^3)	**Total Porosity** (mm^3)	**Porosity Percentage** (%)
T1C1	35.62	0.0010	0.0028
T1C2	43.63	0.0008	0.0018
T2C1	34.23	0.0005	0.0015
T2C2	36.58	0.0003	0.0008

The observed porosity within each specimen is minimal and predominantly exhibits a spherical shape, indicative of trapped gas, as opposed to irregular-shaped porosity typically associated with lack of fusion (LoF) [102, 103]. While DED copper has been reported to exhibit substantial porosity, both interlayer and intralayer [102], it has been demonstrated that this can be controlled and reduced through adjustments to the printing parameters [102, 104]. Consequently, although it is expected that these specimens have low porosity, a quantitative and qualitative examination remains essential.

Figure 4.15 presents a graphical representation of the frequency distribution of porosity volumes observed within each specimen, as measured by µCT. The majority of the porosity in all specimens measures 25,000µm^3 or smaller.

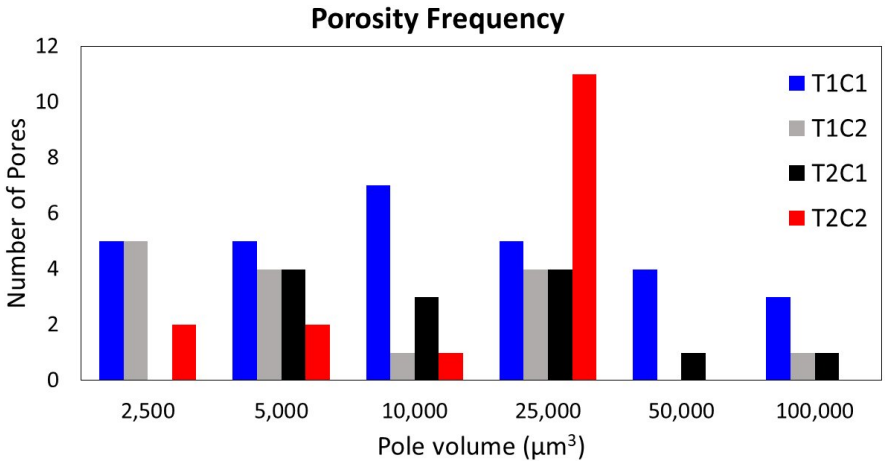

Figure 4.15: Number of pores and their volume found in each deposited wall. It is evident that the majority of pores possess volumes smaller than 25,000µm^3. Notably, 1.2mm specimens, represented by T1C1 and T1C2, exhibit a higher amount of porosity compared to 1.6mm specimens, T2C1 and T2C2.

It is worth noting that the thinner specimens exhibit more substantial porosity in comparison to their thicker counterparts, irrespective of pore volume.

Additionally, while porosity tends to be higher in thinner specimens, the total count of pores in all specimens is meager. Specimen T1C1 displays the highest pore count, with the µCT scan revealing fewer than 30 pores in the examined section.

4.2.3 Microstructure

The specimens microstructure was examined through a combination of optical microscopy, SEM, and EBSD techniques. This analysis aimed to observe microstructural variations along both the build direction (BD) and scanning travel direction (SD). Furthermore, EBSD was employed to determine crystallographic texturing, grain area, and the structure based on crystallographic misorientation. Figure 4.16 depicts a three-dimensional graphical representation of etched cross-sections at various locations of the specimen, with the coordinate system denoting the planes examined in this section.

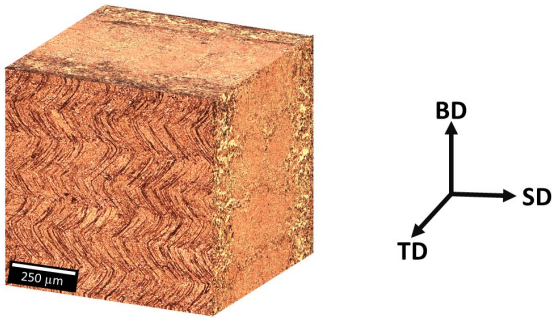

Figure 4.16: Composite image of the microstructure seen in the build direction (BD), scanning direction (SD), and transverse direction (TD) displayed as a three-dimensional cube.

The BD-TD and SD-TD planes displayed equiaxed grains near the borders of the specimens with a less defined, large grains, grain structure on the center.

This characteristics arises from the rapid solidification of the outer surfaces during the deposition process. It is important to note that, the grain structure within the material is primarily governed by two key factors: the thermal gradient (G) and the growth rate (R). These parameters play a crucial role in determine both the size and morphology of the grains present in the microstructure [105, 18]. The distinct zigzag pattern observed on all specimens on the BD-SD plane is attributed to the deposition method used in the fabrication process, which entailed a striping (back and forth) scan strategy. This strategy results in alternating thermal gradients between successive deposited layers, consequently influencing the preferential direction of grain growth [106, 107, 108].

Furthermore, in order to quantify the grain structure and texture, EBSD was performed on the BD-SD plane, parallel to the build direction, and on the SD-TD plane, perpendicular to the building direction. Consequently, the specimens coordinate system was adjusted to accommodate the specific mounting orientation foe each EBSD acquisition, as illustrated in Figure 4.16. Coordinates indicate the acquisition coordinates from the SEM system, and the specimen coordinates are Euler rotations to accommodate how the specimen is mounted for analysis. Thus, EBSD scans at the BD-SD plane of the specimen were collected facing the TD direction, with a (0,-90,0) rotation from the acquisition coordinates, and EBSD scans at the SD-TD plane were collected facing the BD direction, with a (-90,0,0) rotation from the acquisition coordinates.

4.2.3.1 Grains

The examination of grain structure was conducted perpendicular to the build direction in order to avoid the inclusion of elongated grains. The analysis employed EBSD to quantify grains based on their crystal orientation, providing a more accurate measurement of grain area as compared to traditional polishing and etching techniques.

Figure 4.17 depicts a grain map generated using randomly colored grains, with the analysis conducted on the ST-TD plane. Note that the colors used in this representation do not correspond to the actual crystallographic orientation of the grains, rather, they are applied randomly to differentiate one grain from its neighbors. The grain boundaries are distinguished by white lines for low-angle boundaries, with a misorientation angle between 6° and 10°, and black lines for high-angle boundaries with a misorientation angle exceeding 10°.

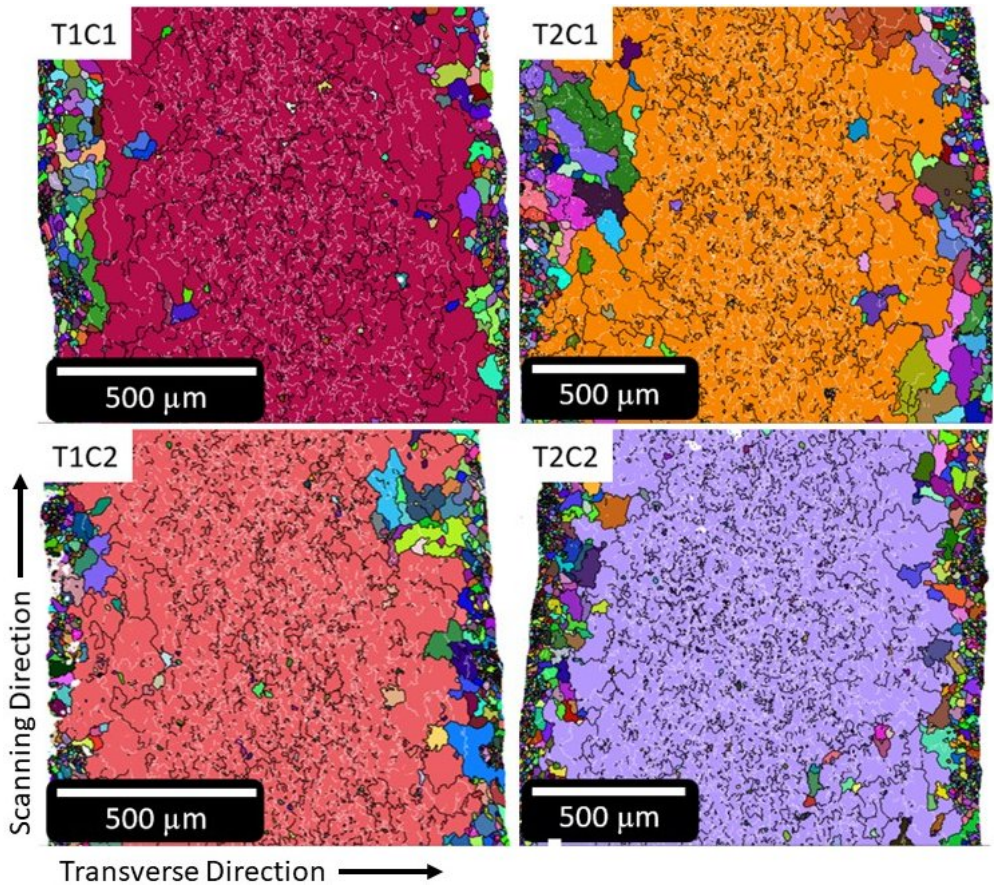

Figure 4.17: Randomly colored grains obtained from specimens oriented perpendicular to the build direction, on the SD-TD plane. High-angle grain boundaries are distinguished by black lines, and low-angle boundaries are represented by white lines. These maps clearly illustrate a pattern of smaller grains along the border of the specimens, with grain size gradually increasing towards the central region.

As explained previously, the variation in grain size between the surface and central regions of the specimens can be attributed to different cooling mechanisms. Convection is dominant on the surface, resulting in a significantly faster cooling rate compared to the central region, where conduction is dominant [18, 106]. The microstructure in DED builds can also be explained by the heat flow and cooling mechanisms present during the fabrication [107, 106]. Additionally, the

central region of the specimens exhibits numerous high- and low-angle boundary lines but lacks well defined grains. It is postulated that due to the preferred crystallographic orientation for FCC crystals and the continuous remelting during layer deposition, the grains are solidifying with misoriented crystals that fail to form distinct grains. Figure 4.18 displays the percentage of grain area for each specimen using measurements obtained through the EBSD analysis on the SD-TD plane, displayed on Figure 4.17.

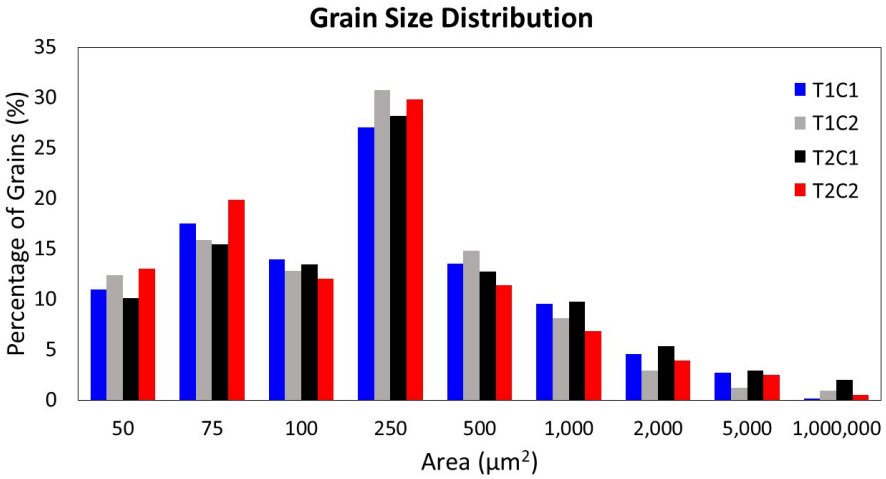

Figure 4.18: Percentage of grain size distribution for each specimen. The data indicate little variation in the occurrence of grain sizes independent of specimen thickness or powder composition.

The analysis reveals a consistent distribution f grain area among all specimens, with approximately 30% of the grains falling within the range of 100 µm^2 to 250 µm^2. This indicates that the grain size remains relatively unaffected by variations in single-wall wall thickness and powder composition for the GRCop-42 under investigation.

4.2.3.2 Texture

Crystallographic texture analysis focused on the BD-SD plane due to challenges in mounting thin specimens perpendicular to the build direction and specimen preparation inherent difficulties (*i.e.,* uneven polishing).

Figure 4.19 present scans parallel to the BD, along BD-TD plane. Epitaxial grain growth is observed aligned with the heat flow direction. These grains present a preferred growth orientation during solidification based on the heat gradient along the BD, from left to right, as previously observed in DED textures [107, 109, 77]. The color coding in the figure represents the [101] orientation, corresponding to the IPF with respect to the TD direction (IPF/Y map), which is normal to TD during acquisition. The pole figures (PF) required minor manual adjustments to properly align the texture with the proper poles due to slight misalignments during specimen preparation and SEM stage setting for EBSD. The texture is described with the indices {hkl}<uvw>, where the first indices {hkl} describes the crystallographic plane and the second indices <uvw> describe the crystal direction [110].

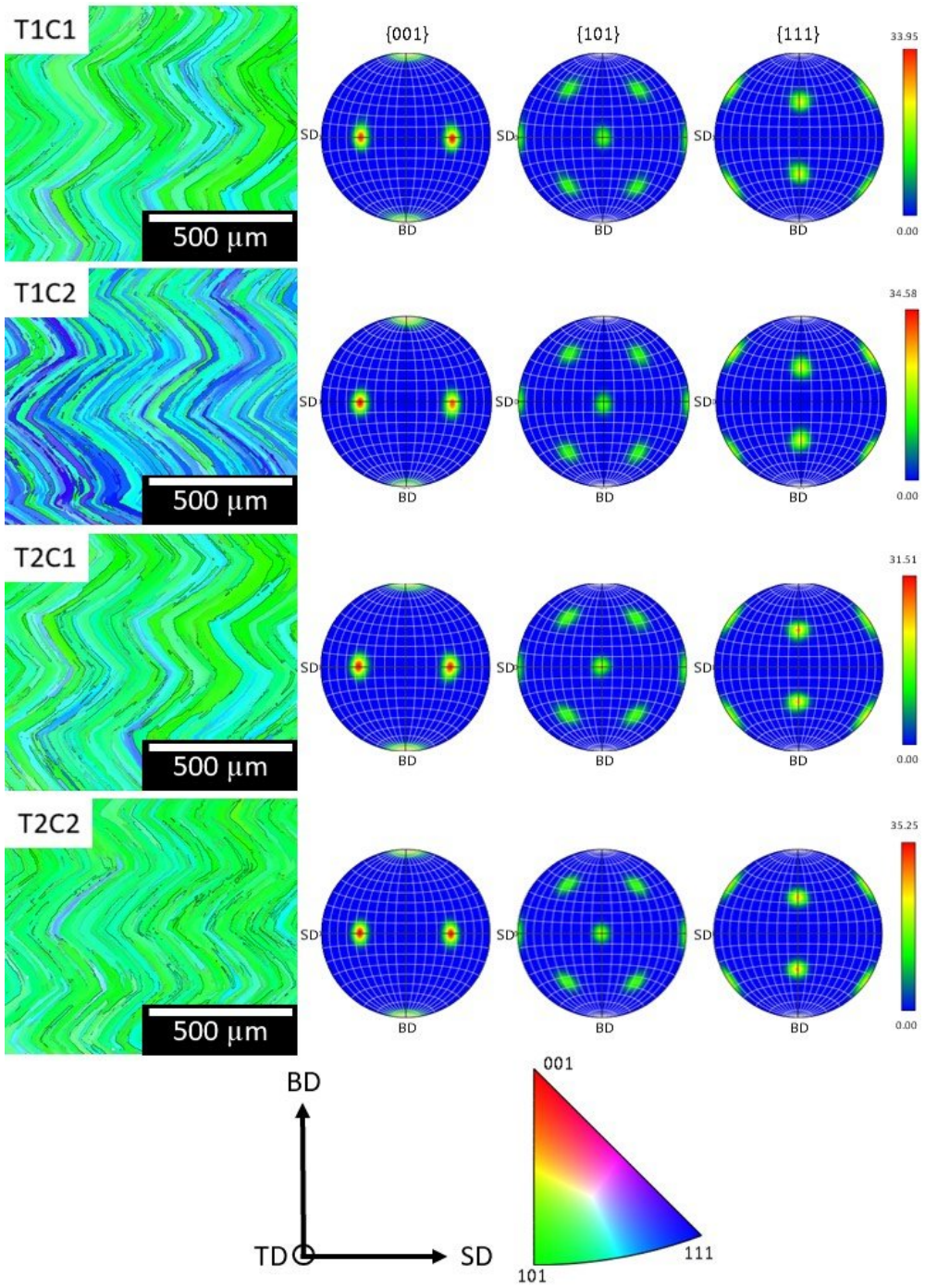

Figure 4.19: IPF maps, colored according to the TD direction, were generated for the BD-SD plane, along with their corresponding PF. It is evident in these representations that all specimens exhibit a strong (001) texture. Additionally, A fully defined {001}<101> texture is observed across the specimens.

A fully defined crystallographic texture, {001}<101>, is evident. The first set of indices, {001}, describes the crystallographic plane parallel to BD, while the second set, <101>, designates the direction parallel to the scanning travel direction. Notably, all specimens exhibit high texture on the (001) plane. This alignment can be attributed to the tendency of FCC crystals to form in the <001> direction during solidification [105, 108]. Furthermore, crystals tend to solidify parallel to the direction of heat flow, aligned with the maximum thermal gradient at the solidification front [111], which is, typically, normal to the BD in AM processes [112]. During the LP-DED, the deposition path (and thus heat flow direction) changes, establishing the growth direction [113]. A deviation from the build direction is observed during solidification, with the grains solidifying at an angle of 45° to 60° from the deposition surface, ultimately leading to a highly textured material in the [101] direction. Similar behavior has been documented in Inconel-718 [114, 113] and in 316L thin walls [107].

4.2.4 Quasi-Static Test

The surface irregularities produced during layer deposition and the distinct layering observed in DED specimens pose challenges to obtaining precise measurements using calipers to determine a specimen's effective load bearing area. As demonstrated in a previous study [40], the measurement that yields a more accurate cross-sectional area is resolved through µCT scanning. This method involves dividing the total scanned volume by the depth of the scan. However, due to its inherently high cost and time-intensive nature, only one specimen for each

deposited wall was subjected to µCT scanning. Additionally, as specimens are likely to fracture at the smallest cross-sectional area, the minimum area identified via µCT was adopted as the load-bearing area in this study instead of the average cross-sectional area.

To explore a more cost-effective approach for calculating the load-bearing area, this study examined the possibility of establishing a correlation between caliper measurements and the maximum peak height, denoted as Sp. The Sp value was determined from the average surface topography measurements of specimens for each deposited wall. To adjust the cross-sectional area, the Sp value was subtracted from the caliper measured thickness prior to multiplying it by the caliper-measured width. This process yielded close approximations to the area obtained through µCT measurements. A comparable approach for determining the load-bearing area was employed by Yu *et al.*, where the mean value of the peak height was subtracted from the caliper-measured cross-section [75]. In other studies, various methods have been devised to correlate the surface topography of AM components with caliper-measured areas for estimating the effective load-bearing area [77, 76].

Table 4.6 presents the width, thickness, Sp, calculated area, µCT area, and the percent error for each specimen. As observed, the effective load-bearing area can be more accurately determined by subtracting the highest peaks from a caliper-measured thickness.

Table 4.6: Provides the for caliper-measured width, caliper-measured thickness, maximum peak height (Sp), adjusted area, minimum µCT measured area, and the corresponding percentage error between the adjusted area and the minimum µCT measured area.

	Width (mm)	**Thickness** (mm)	**Sp** (mm)	**Area** (mm^2)	**µCT** (mm^2)	**Percent Error** (%)
T1C1	1.97	1.28	0.106	2.30	2.34	1.71
T1C2	2.46	1.21	0.084	2.77	2.58	-7.36
T2C1	1.89	1.51	0.097	2.67	2.66	-0.38
T2C2	1.94	1.60	0.098	2.91	2.87	-1.39

It is noteworthy to mention that these calculations are based on the assumption of uniform surface topography on both sides of the wall and consistent throughout the specimen's height. This assumption is reasonable because the powder and printing parameters remained constant during the entire deposition process for each wall. Further validation of the proposed method for adjusting the cross-sectional area was obtained by generating stress-strain curves using the caliper-measured area, minimum µCT-measured area, and the adjusted area for each specimen. These results were then compared to the stress-strain curve of polished specimen, which is unaffected by surface roughness and waviness. The comparative findings are presented in Figure 4.20.

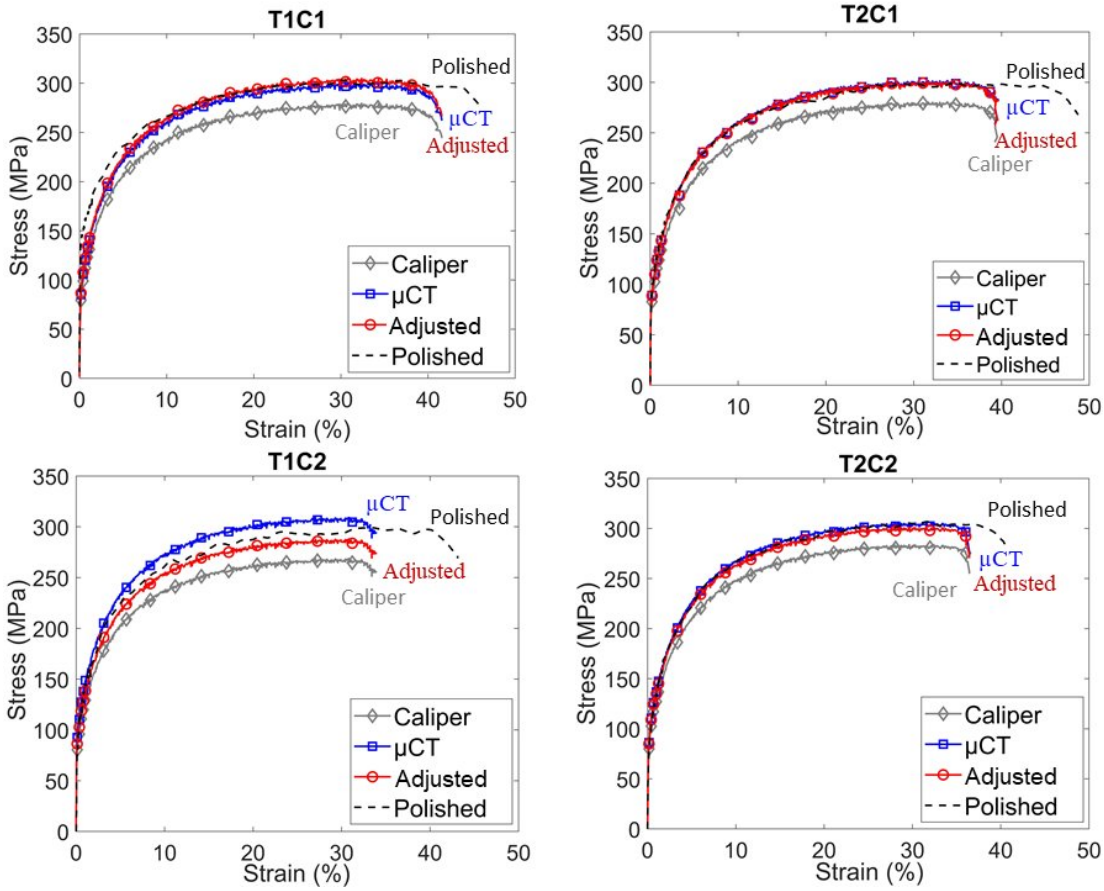

Figure 4.20: Overlay of engineering stress-strain curves obtained using various cross-sectional area calculation methods. It is evident that the caliper-measured area results in the lowest stress values, while the minimum µCT-measured area, the calculated area, and the polished specimen exhibit comparable stress responses.

The findings support the validity of subtracting the maximum peaks from the caliper-measured area, resulting in estimates closely resembling those derived from the minimum µCT-measured area and the polished specimens. Consequently, this approach is considered reliable from cross-sectional area determination of DED GRcop-42 specimens.

The size effects and orientation effects present during the DED builds were investigated through quasi-static loading tests using the adjusted cross-sectional area method described above. Figure 4.21 depicts the engineering stress-strain relationship for horizontal and vertical specimens, along with essential material properties such as Young's Modulus (E), YS, UTS, and percent elongation, as listed in Table 4.7.

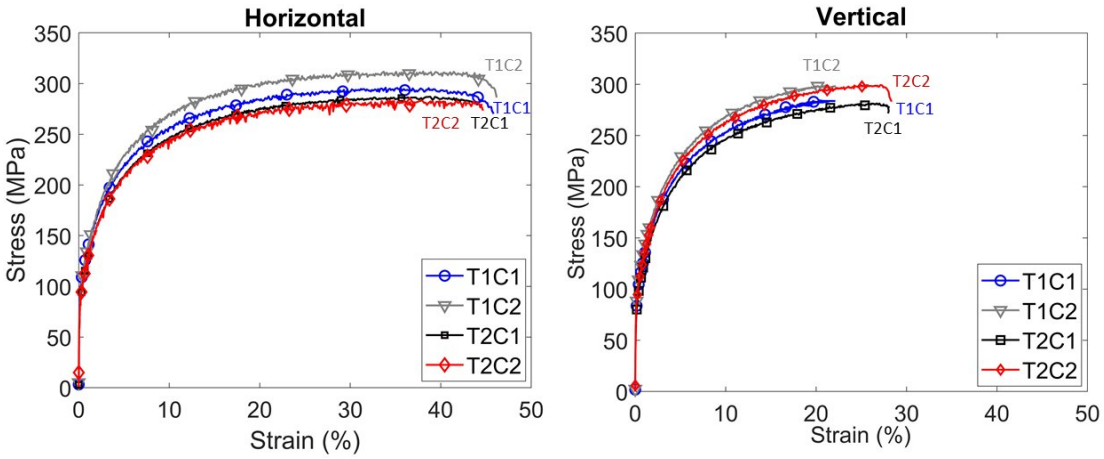

Figure 4.21: Engineering stress-strain curves for as-printed specimens oriented both horizontal and vertical directions with respect to the build direction. Note that horizontal specimens have similar elongations to each other. Conversely, the vertical specimens display a significant reduction in elongations, with a 38% decrease in thicker specimens and a 51% reduction in thinner specimens compared to their horizontal counterparts.

Table 4.7: Mechanical properties of the specimens tested. The specimens are categorized as follows: T1 and T2 represent thicknesses of 1.2mm and 1.6mm respectively, while C1 and C2 correspond to alloy compositions with 1.08Cr/Nb and 1.14Cr/Nb respectively. The designations of and H and V signify horizontal and vertical specimen orientations, respectively.

	E (GPa)	**YS** (MPa)	**UTS** (MPa)	**% Elongation**
T1C1 V	80 ± 9.5	97 ± 2.7	281 ± 5.7	23 ± 0.7
T1C1 H	78 ± 3.3	103 ± 5.4	290 ± 5.9	42 ± 5.9
T1C2 V	62 ± 3.3	101 ± 6.3	282 ± 12.3	19 ± 2.6
T1C2 H	67 ± 15.4	121 ± 14.3	301 ± 10.7	37 ± 8.7
T2C1 V	69 ± 12.8	97 ± 4.8	285 ± 5.3	25 ± 2.3
T2C1 H	92 ± 0.6	96 ± 3.3	290 ± 2.1	48 ± 4.3
T2C2 V	70 ± 14.1	102 ± 9.0	296 ± 2.6	30 ± 3.6
T2C2 H	97 ± 13.7	104 ± 10.9	257 ± 8.3	47 ± 2.5

The data presented in Table 4.7 reveal differences in YS and UTS between horizontal and vertical specimen orientations, particularly when considering two specimens thicknesses, 1.2mm and 1.6mm as well as two different alloy compositions, 1.08Cr/Nb and 1.14Cr/Nb. For the 1.2mm specimens, the YS and UTS are consistently higher in horizontal specimens when compared to their vertical counterparts. Specifically, specimen T1C1 exhibits a 6.42% higher YS and 3.25%

higher UTS for the horizontal orientation, while specimen T1C2 29.00% higher YS and 7.24% higher UTS in the horizontal orientation. In contrast, the 1.6mm specimens generally exhibited lower YS in the horizontal orientation, though UTS values vary. For instance, specimen T2C1 demonstrates a 0.13% lower YS but a 1.76% higher UTS for the horizontal specimens, whereas specimen T2C2 exhibits a 9.52% lower YS and a 13.29% lower UTS.

The relationship between specimen strength and build orientation has been observed before by Yadav *et al.* [102], who explored the properties of copper specimens fabricated through DED in the horizontal and vertical orientations. It was reported a 12.7% higher YS and a 3.7% higher UTS for horizontal specimens compared to vertical specimens. These variation was attributed to differences in microstructure formed along the build direction and scanning travel direction. Figure 4.22 shows a graphical representation of the results displayed in Table 4.7.

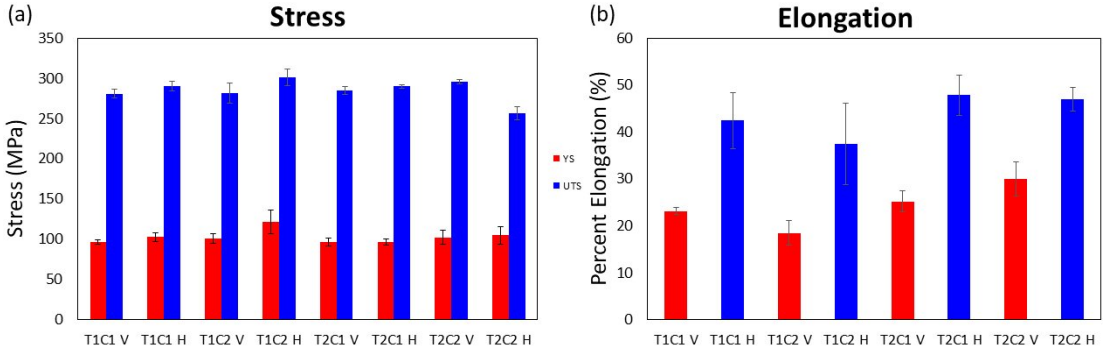

Figure 4.22: Mechanical properties of the tested specimens presented in Table 4.7. Chart (a) illustrates the YS and UTS values for each specimen, while chart (b) displays the percent elongation for these specimens.

From Table 4.7, Figure 4.21, and Figure 4.22, it is evident that horizontal specimens exhibit approximately twice the elongation of their vertical counter-

parts. This discrepancy can be attributed to the pronounced layers observed in the as-printed walls, which generate stress concentrations in the interlayers and reduce the effective load-bearing area. Furthermore, orientation and thickness dependence are apparent, where thicker vertical specimens exhibit a lower decrease in ductility compared to thinner horizontal specimens, a trend ascribed to the smaller load-bearing area perpendicular to the load direction, providing a lower resistance to crack propagation.

Another comparable size effect becomes evident among the vertical specimens, where specimens T2C1 and T2C2, both 1.6mm, demonstrate approximately 6% higher elongation compared to specimens T1C1 and T1C2, which are 1.2mm. This can be attributed to the difference in specimen thickness, with thicker specimens offering a relatively larger effective load-bearing area that can better sustain stress concentrations induced by the layering effects. Yadav *et al.* observed negligible differences in elongation between horizontal and vertical DED copper specimens, with values in the range of 19 % to 20 %, where the low elongation was primarily attributed to the fine grain size rather than surface effects [102]. In contrast, Ti-6Al-4V produced through DED exhibited twice the elongation [57, 18] and superior properties [115] for horizontal specimens compared to vertical specimens. This difference was attributed to planar porosity resulting from incomplete remelting and incomplete melted powder particles in vertical specimens. This observed anisotropy was shown to be eliminated with HIP [57, 18], which assisted in closing the porosity and homogenizing the microstructure.

Furthermore, Balit *et al.* [107] showed 4.5% higher ductility for vertical specimens compared to horizontal specimens in 316L DED thin wall specimens. It is important to note that Balit polished the specimens to remove surface topography and part distortions, emphasizing the need to investigate mechanical responses in the absence of surface artifacts. Figure 4.23 provides engineering stress-strain plots for polished horizontal and vertical specimens, where the cross-sectional area was calculated using a calipers sue to flat surfaces (not surface topography effects).

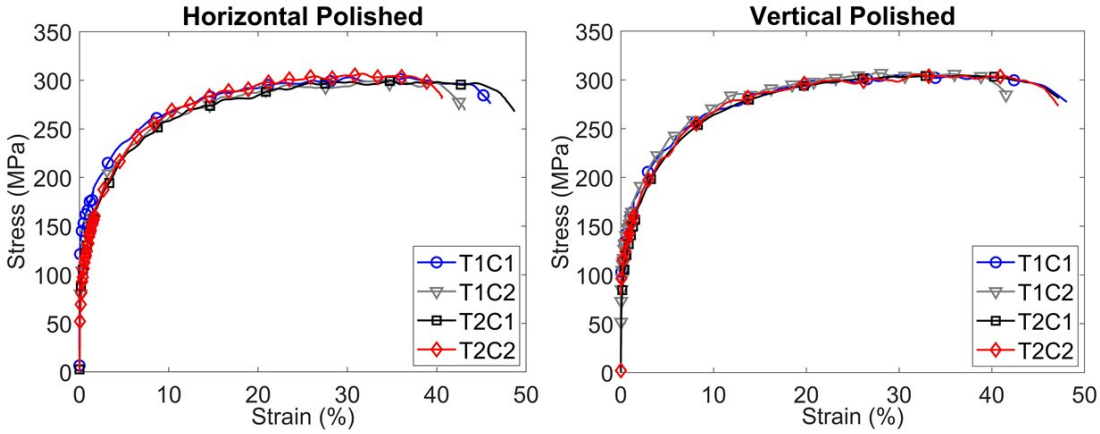

Figure 4.23: Engineering stress-strain plots for polished specimens on vertical and horizontal orientations.

The stress-strain curves for horizontal and vertical specimens in the polished condition are virtually identical, indicating that discrepancies in YS and UTS attributed to specimen thickness and composition disappears. Additionally, the lower elongation observed in vertical specimens compared to horizontal specimens is eliminated in the absence of surface artifacts. These results highlight the

significant contribution of uneven surface topography to the observed differences in tensile response.

4.2.5 Fractography

Fractography analysis was conducted on post-tensile test specimens to establish correlations between microstructural features such as grain structure, porosity, and surface characteristics, and their impact on mechanical performance and fracture features. Figure 4.24 displays SEM images of vertical specimens with the as-printed surface. It is notable that fractures occur within the interlayers, coinciding with areas characterized by stress concentrations and exhibiting the smallest cross-sectional area of the specimens' gage section.

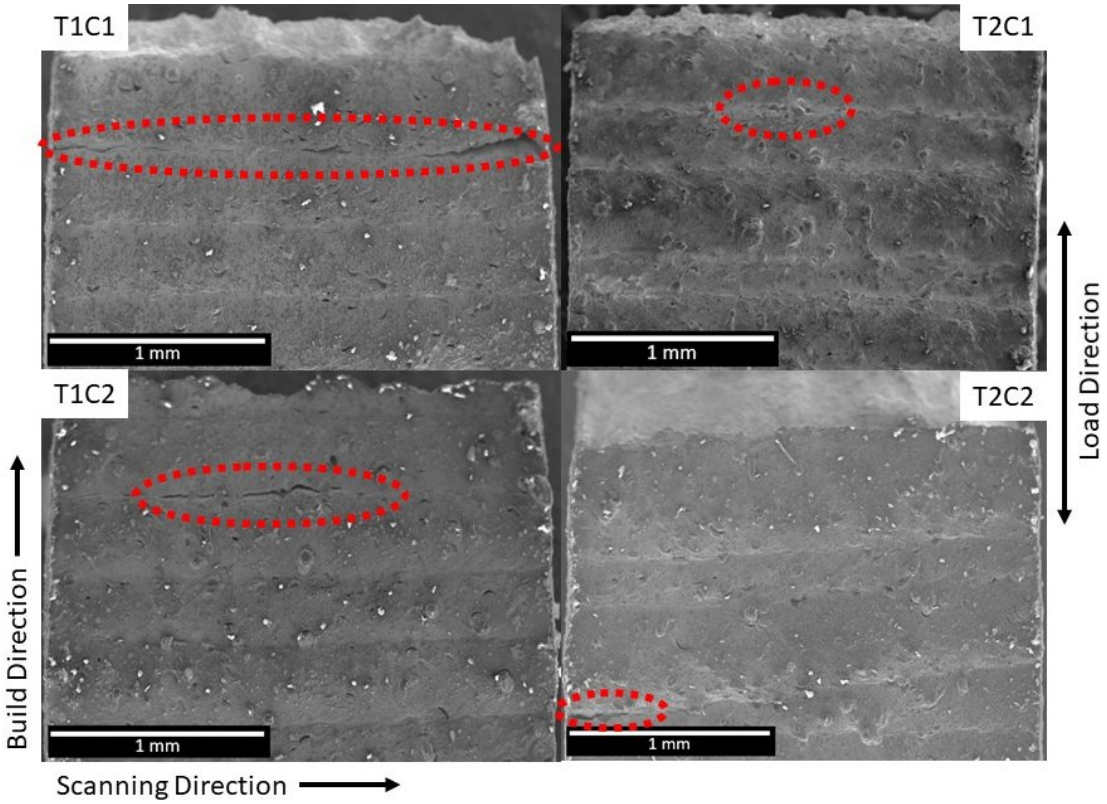

Figure 4.24: Post-tensile test of vertical specimens with the as-printed surface. Dotted red circles highlight the separating layers near the fracture surface.

During uniaxial loading, it is observed that multiple layers within the specimens experience separation, which means the specimens started to fail at several locations along the gage section. Note that all fractures initiate in the interlayers of the deposited specimens. This observation is consistent with expectations, as the interlayers represent the weakest regions in the specimens and are oriented perpendicular to the direction of the applied load.

Figure 4.25 depicts optical images of post-tensile test vertical specimens with both, as-printed and polished surfaces, specimens were etched to highlight

the fracture location relative to the build layers. Note that the surface of the polished specimens is polished prior to performing the tensile test in order to compare the relationship between microstructure fractures and fracture surface for polished specimens versus specimens tested with the as-printed surface.

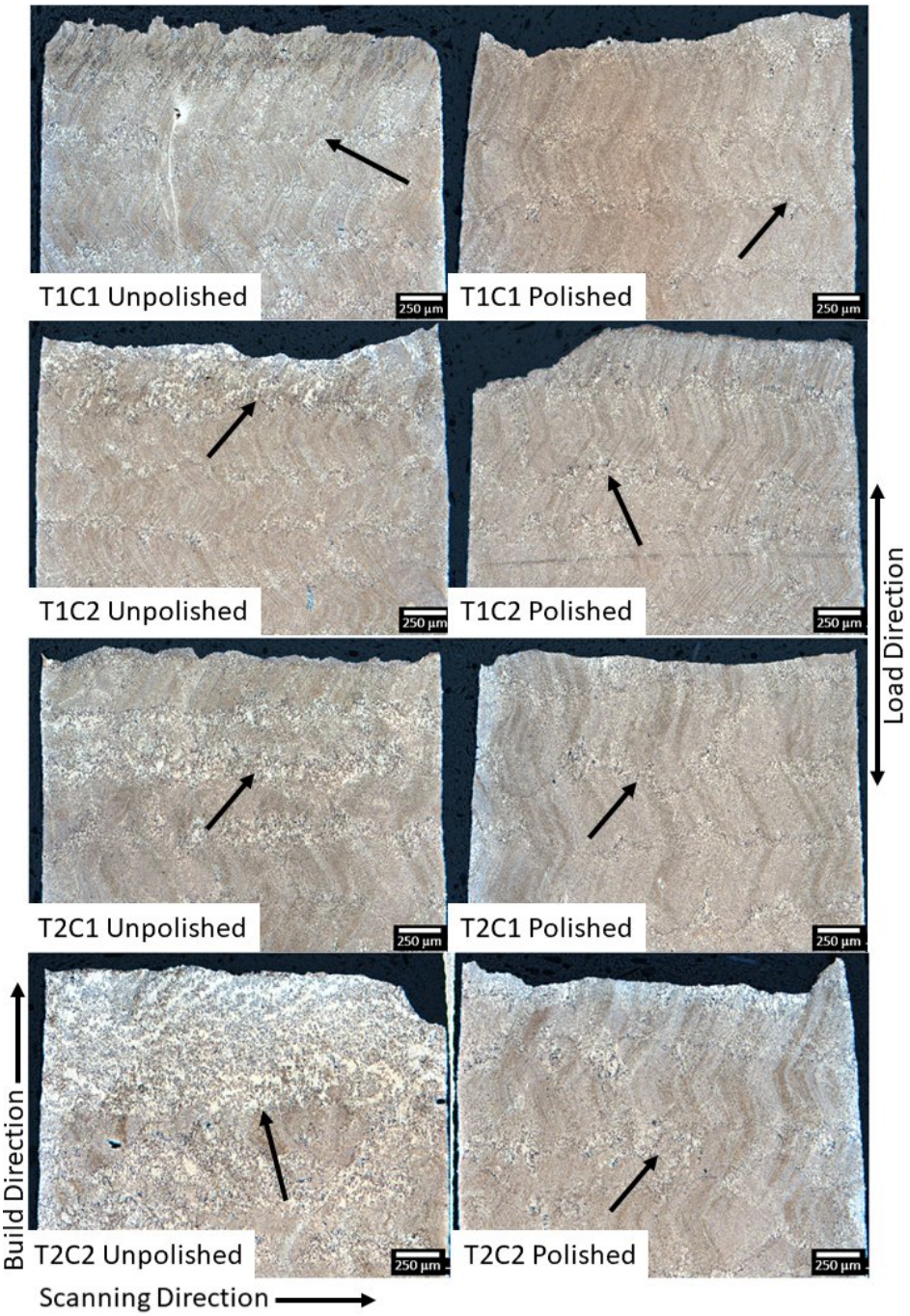

Figure 4.25: Etched cross-section of post-tensile test vertical specimens in the as-printed (unpolished) surface and polished conditions. The as-printed specimens display a significantly higher amount of deformation in between deposited layers compared to the polished specimens.

The specimens with the as-printed surface presented a significantly higher degree of deformation between the deposited layers in comparison to the specimens that were subjected to pre-tensile testing polishing. It is presumed that the higher degree of deformation is due to the stress concentration arising between the deposited layers during the fabrication process. The stress concentrations are eliminated by polishing the specimens, which is verified by a lower degree of deformation in the polished specimens as well as the increased elongation for polished vertical specimens described in Section 4.2.4. This observation suggests that when a load is applied perpendicular to the BD, the interlayers emerge as the weak points in an DED deposited components. This susceptability can be attributed to their smaller cross-sectional area, rendering them less capable of resisting crack propagation and stress concentration, and therefore acting as crack initiation sites. Consequently, it is reasonable to conclude that the interlayers cause a reduced elongation observed during quasi-static testing.

Furthermore, although significantly less deformation is observed on the polished specimens than the as-printed specimens, deformation is still visible between the deposited layers, as seen in Figure 4.25. This indicates that additional features lead to the interlayers being a weaker point in the deposited parts. As the deformations are primarily located in or around the interlayers, it is postulated that the change in crystallographic orientation with each subsequently deposited layer is responsible for the deformation. However, a more in depth analysis is required to characterize this behavior.

4.3 Comparison Between Laser Powder Bed Fusion and Direct Energy Deposition of GRCop-42

Although both L-PBF and DED deposition techniques build components on a layer-by-layer fashion, they differ on the build ambient, feedstock, power, speed, and size. The deposition time also varies significantly with each process, DED exhibiting a deposition rate of five times of the L-PBF ($25cm^3/h$ for DED compared to $5cm^3/h$ for L-PBF). However, the increase in deposition rate comes at the sacrifice of geometric precision and feature resolution [116].

Moreover, the laser spot size in DED is typically an order of magnitude larger with a scanning velocity of 1-2 orders of magnitude smaller than L-PBF, and the powder size used in DED systems is also 2-5 times larger than the powder size used in L-PBF [117, 118]. Since the laser diameter in L-PBF is an order of magnitude smaller, it results in smaller melt pools, and thus, a higher solidification rate. It has been reported that the cooling rate in L-PBF is 1000x faster than DED [117], which has a direct impact on the microstructure [119]. Additionally, the higher scanning velocities in L-PBF lead to higher solidification velocities and higher thermal gradients, which can also lead to changes in the solidification structure.

Aside from microstructural differences, the deposition method influences the surface topography, internal defects, and residual stresses. For instance, L-PBF components are build on a build plate surrounded by loose powder which are partially melted during the fabrication process and stick to the components'

surface [120]. Furthermore, internal defects also result from the power used during the deposition process and are detrimental to mechanical properties [96, 24, 97, 98]. For example, the power intensity can lead to inadequate melt pool penetration or powder vaporization resulting from lower or higher power input, respectively [121, 122]. These aspects need to be evaluated to understand its implications on the mechanical properties for each material and fabrication process.

This section characterizes GRCop-42 produced using L-PBF and DED processes. It investigates the surface topography, internal defects, microstructure and texture, and tensile responses of specimens from both deposition methods. Given that both L-PBF and DED have distinct advantages and end-use applications, it is important to fully characterize their individual properties and highlight these differences by comparing each aspect of the fabrication methods.

4.3.1 Surface Topography

Surface topography is the result of several parameters during the fabrication process and plays a pivotal role in determining a component's performance. For instance, research has revealed that surface topography can decrease the strength of specimens [92, 93, 94], which arises from stress concentrations created by surface roughness. However, it has also been demonstrated that the magnitude of the stress concentration is directly related to the magnitude of the surface roughness [94]. This implies that lower levels of surface roughness may have an insignificant impact on the strength of a specimen. In this study, numerous parameters are expected to influence surface topography. These include

aspects related to the material feedstock, such as the alloy type, particle size, and powder morphology. Additionally, the deposition process selection (*i.e.,* L-PBF and DED), and the specific process parameters, such as heat source power, travel speed, layer height, and scan strategy are instrumental in shaping the surface topography [117]. For example, the surface roughness increases as the layer thickness increases, decreasing the layer thickness would reduce surface roughness but increase the build time [123].

Figure 4.26 displays SEM images of the surface for (c) L-PBF spcimens and (d) DED specimens. Part (a) and (b) offer graphical representations of the specimen's orientation relative to the build platealong with their coordinate axis. Additionally, red boxes on the specimens are used to indicat the location from which the SEM images were acquired.

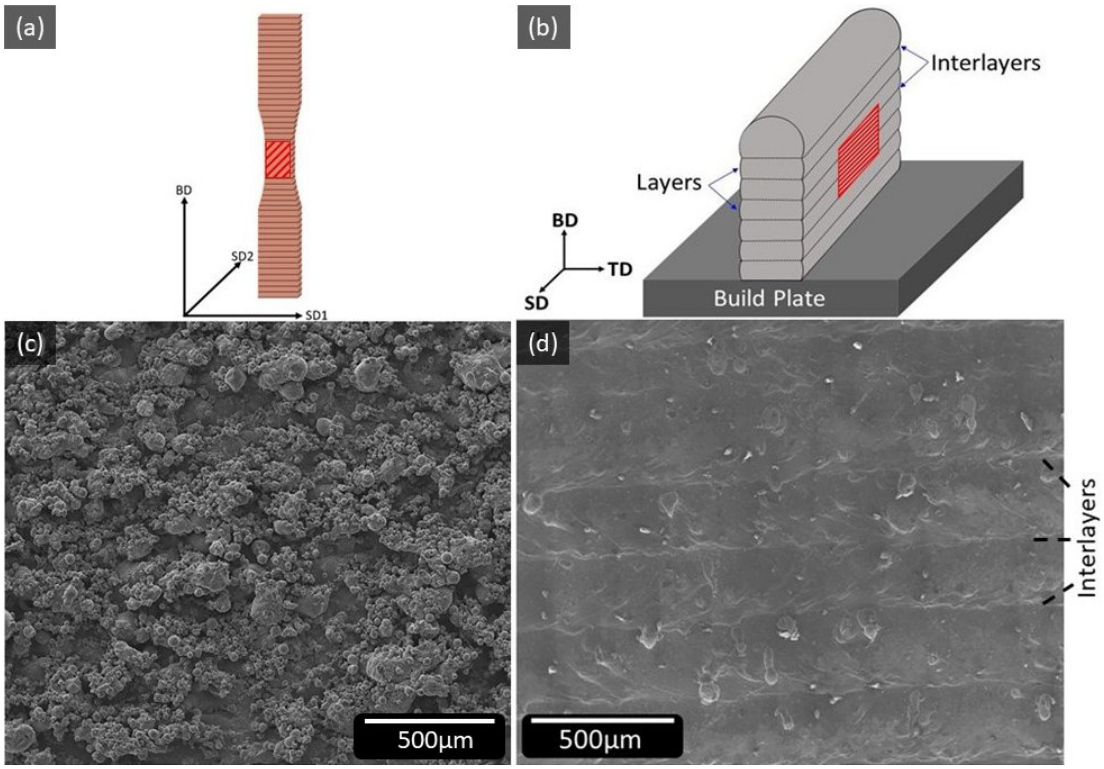

Figure 4.26: Graphical illustration of (a) L-PBF and (b) DED specimens during fabrication along with their coordinate system. Note that red boxes are used to elude to areas where SEM images of the surface were collected, which are depicted for (c) L-PBF and (d) DED specimens.

L-PBF specimens exhibit a substantial accumulation of loose and partially melted powder adhering to the surface, a consequence of their fabrication process, which occurs within an environment containing loose powder surrounding the component being built. This could also be caused by improper heat inpute, which can result in the adhesion of partially melted particles to the surface or balling effect [120]. In contrast, DED specimens display little powder adhering to the surface, implying that most of the powder blown into the laser source was either melted or immediately blown away from the component. However, DED

specimens exhibited evident layers, a direct outcome of their deposition process, while L-PBF specimens lack any noticeable surface waviness. These interlayers present on DED specimens can induce stress concentrations and potentially lead to a significant overestimation of the load-bearing area. Both these characteristics require careful consideration during the component design process.

Table 4.8 displays the surface roughness values obtained for both the L-PBF and DED specimens. The following surface characterization parameters were measured: average areal surface roughness (Sa), root mean square surface roughness (Sq), max measured valley depth (Sv), maximum measured peak height (Sp), and the collective range of maximum height of the surface (Sz).

Table 4.8: Surface topography values obtained from the surface analysis through laser microscopy for both L-PBF and DED specimens.

	Sa (µm)	**Sq** (µm)	**Sv** (µm)	**Sp** (µm)	**Sz** (µm)
1.0mm - L-PBF	22 ±2.0	28 ±2.2	79 ±8.9	95 ±14.0	176 ±10.3
1.7mm - L-PBF	20 ±2.8	25 ±3.3	75 ±7.9	91 ±14.6	165 ±18.2
1.2mm - DED	13 ±0.1	17 ±0.0	61 ±3.7	97 ±6.0	158 ±9.6
1.6mm - DED	13 ±0.2	17 ±0.1	59 ±4.4	98 ±6.9	157 ±2.5

Both specimen thicknesses for each deposition method are in good agreement with each other, suggesting minimal surface topography variation within the same build. Moreover, the surface topography values appear to be similar

for both deposition methods. While Sa, Sq, and Sv values for L-PBF specimens are slightly higher, they exhibit no significant differences between the two methods. The most pronounced divergence is the Sv value, with an 18µm differential observed between the 1.0mm L-PBF specimen and the 1.2mm DED specimen. Importantly, while the numerical values of surface topography measurements may not significantly differ between L-PBF and DED process, it is crucial to acknowledge that the impact of surface topography on components can vary significantly between these deposition methods. For instance, while the surface roughness in the absence of waviness had a negligible influence on the quasi-static response of L-PBF GRCop-42 [40], the pronounced waviness observed in GRCop-42 produced via DED had a significant impact on specimen elongation [124].

4.3.2 Porosity

Internal defects, such as gas porosity and lack of fusion, are common in AM components and significantly impact mechanical properties. These defects are closely related to the manufacturing process. For instance, a high power density can lead to powder vaporization, entrapping gases within the material [122], whereas lower power inputs can result in insufficient melt pool penetration on the previously deposited layers, creating lack of fusion defects [121]. Additionally, porosity can arise from gas entrapment during the deposition process, often due to the use of inert gases used to prevent contamination, or even during the powder atomization process [117].

Figure 4.27 displays a three-dimensional graphical representation of μCT scans for both L-PBF and DED specimens. It is evident that L-PBF specimens exhibited a higher occurrence of porosity compared to DED specimens. Furthermore, the porosity in L-PBF specimens appear to be of irregular shapes, indicative of lack of fusion defects, while DED specimens display spherical porosity, typically associated with entrapped gases [102, 103]. Quantitative porosity data, including porosity volume, scanned volume, and the porosity ratio percentage, are presented in Table 4.9.

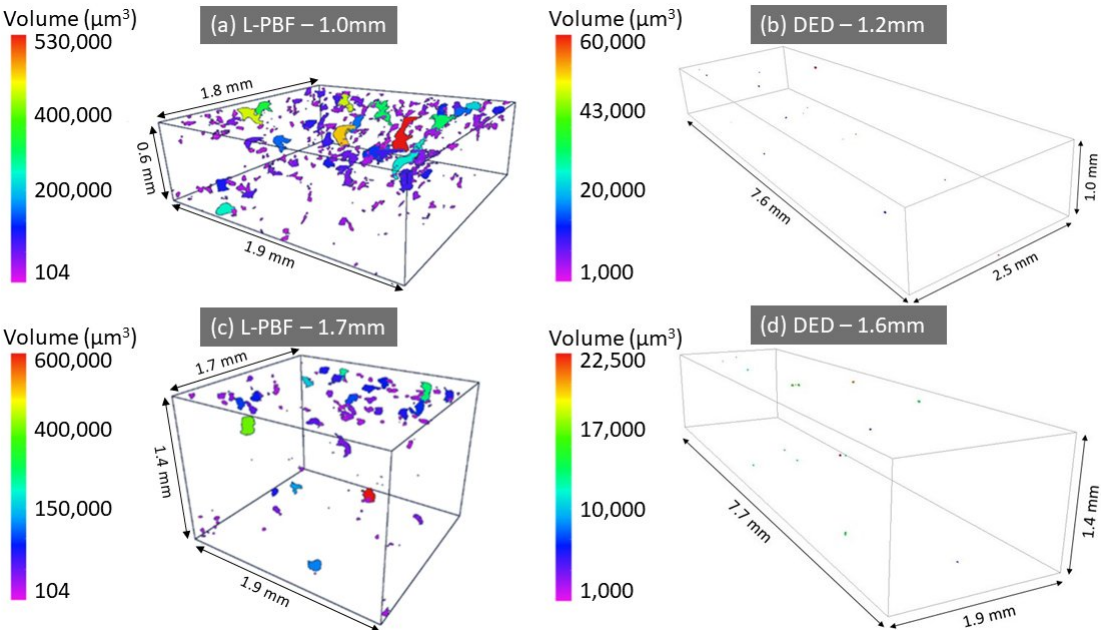

Figure 4.27: Graphical illustration of a three-dimensional reconstruction of the μCT scans. Note that L-PBF specimens display substantially more porosity than DED specimens.

Table 4.9: Porosity values obtained from the μCT analysis depicting the total scanned volume, porosity volume, and the porosity volume ratio percentage. It is noteworthy to mention that these scans were conducted at different times, leading to a different total volume scanned.

	Total Volume (mm^3)	**Porosity Volume** (mm^3)	**Porosity Percentage** (%)
1.0mm - L-PBF	2.0	0.008	0.42
1.7mm - L-PBF	4.4	0.005	0.12
1.2mm - DED	43.6	0.0008	0.0018
1.6mm - DED	36.6	0.0003	0.0008

In L-PBF specimens, internal defects constituted a notable portion, approximately 0.42% of the volume for 1.0mm specimens and 0.12% for 1.7mm specimens. Interestingly, the volume of porosity demonstrated a decrease as the specimen's thickness increased, as reported previously [40]. In sharp contrast, DED specimens exhibited minimal porosity, regardless of the specimen thickness, and can be considered fully dense.

Internal defects are widely acknowledged as significant influencers of a material's mechanical response [96, 24, 97, 98], and studies have revealed that they become increasingly critical in reducing material strength as the specimen size decreases [40]. Therefore, it is reasonable to expect that the mechanical properties of GRCop-42, produced via L-PBF and DED, will exhibit differences corresponding to the variations in porosity content.

4.3.3 Microstructure

The AM process encompasses a multitude of parameters including scanning speed, power, spot size, powder size, powder layer thickness (in the case of L-PBF), and powder flow rate (in the case of DED). The differing thermal conditions in these two processes can be quantified through the normalized energy density, represented as E^*, defined as

$$E^* = \frac{P^*}{v^* l^* h^*} \tag{4.1}$$

where P is the laser power, v is the laser velocity, l is the layer thickness, h is the hatch spacing, and * designates normalized values, which is calculated as

$$E^* = \frac{A_b P}{2vlh} \frac{\alpha}{\kappa(T_m - T_0)} \tag{4.2}$$

where A_b is the absorptivity, α is the thermal diffusivity, κ is the thermal conductivity, T_m is the melting point (solidus) and T_0 is the initial temperature [118, 125]. This parameter, provides insight into the energy required to melt a certain amount of material.

These parameters have a direct impact on the resulting grain structure and crystallographic texture. The critical parameters for determining these outcomes are the temperature gradient G, solidification rate R, and undercooling ΔT [117]. The combination of these parameters governs the solidification behavior: the ratio G/R governs the mode of solidification, while the product $G \times R$ determines the

size of the solidification structure [126]. In AM components, the grain growth rate is significantly influenced by the scanning speed and the location of the melt pool boundaries, which diverge substantially between L-PBF and DED processes [117].

Figure 4.28 depicts etched microstructures of L-PBF specimens on the left and DED specimens on the right. The microstructures in both parallel to the build direction (BD-SD plane) and perpendicular to the build direction (TD-SD plane) are shown on the upper and lower sections of the figure, respectively.

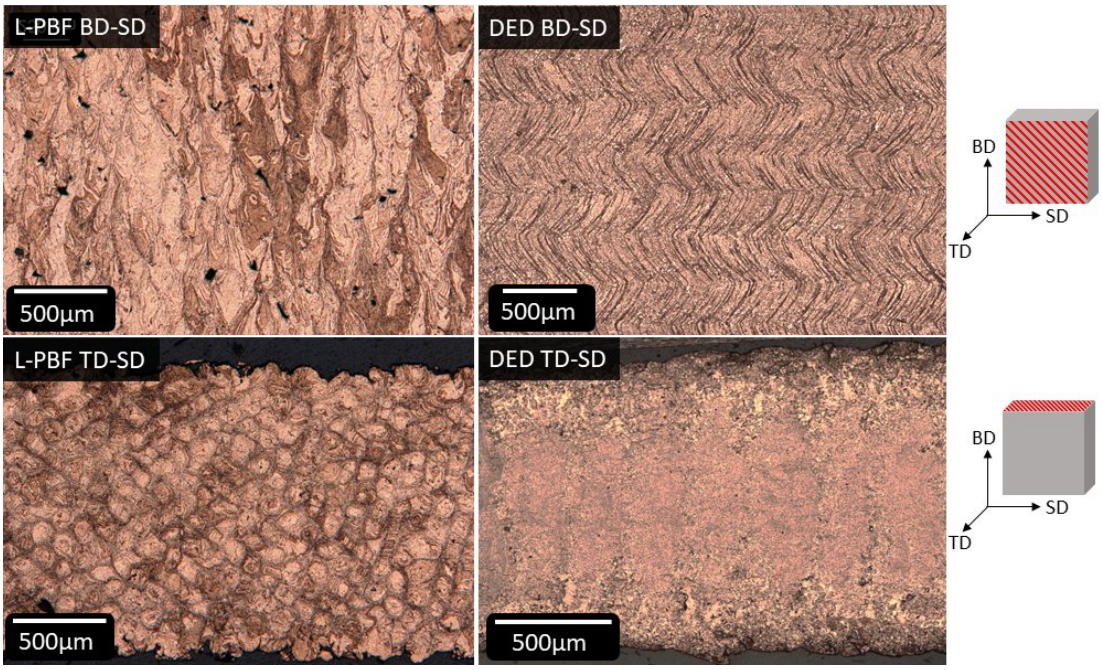

Figure 4.28: Optical images of the specimens etched cross-sections displaying the planes parallel to the build direction on the top roll and perpendicular to the build direction on the bottom roll. L-PBF specimens are depicted on the left and DED specimens on the right.

Significant variations in microstructures are evident between the two deposition methods. L-PBF demonstrates epitaxial grain growth through the layers

parallel to the build direction while easily discernible laser scan spots perpendicular to the build direction. These observations is in line with previous work [127], which showed nearly vertical columnar grain growth for specimens produced through L-PBF. In contrast, DED specimens display a zig-zag pattern running parallel to the build direction. The directional change occurs due to the alignment of grain growth with the temperature gradient [117]. Moreover, the alteration in directionality is a consequence of the bidirectional scanning mode employed during fabrication [108]. Perpendicular to the build direction, DED specimens presented a combination of grain structures: fine equiaxed grains appear along the wall edges, while the grain size increases towards the center. This phenomenon is attributed to variations in solidification rates - faster solidification at the edges, dominated by convection, compared to the center where conduction prevails [18, 106].

Figure 4.29 displays the inverse pole figure (IPF) maps for both L-PBF and DED specimens with scans obtained parallel to the build direction along with their respective pole figures. It is noteworthy to mention that the although the specimen orientations are identical for both specimens, the acquisition orientation during data collection are different and thus, the maps are using different coordinates and colored accordingly.

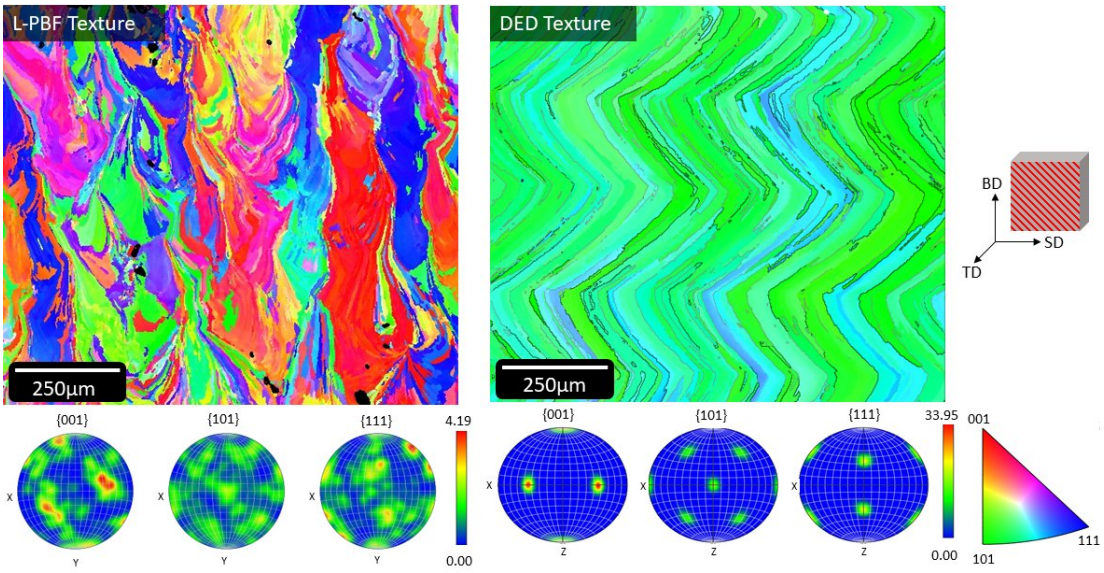

Figure 4.29: EBSD analysis conducted on the plane parallel to the build direction for L-PBF and DED specimens along with their corresponding pole figures.

L-PBF reveals moderately textured specimens, featuring a maximum multiples of uniform distribution (MUD) number of 4.19. The majority of grains oriented along the <001> direction along the build direction, which is consistent with other cubic materials [86, 118]. DED specimens are highly textured, characterized by a MUD number of 33.95 and present <001> oriented grains with rotated cube texture along the build direction. These divergent texture patterns are likely contributors to a higher degree of anisotropy for DED specimens.

These variations in texture can be attributed to the distinctive deposition techniques employed. L-PBF entails multiple remelting of layers and a specific scanning strategy, which results in multiple solidification fronts [91]. Conversely, DED employed a striping back and forth strategy, yielding continuous solidifica-

tion fronts in each layer. This aligns the heat flow direction with the preferred crystal growth direction, leading to a highly textured structure [117].

4.3.4 Quasi-static Test

Mechanical properties of the specimens were determined through quasi-static tests conducted until failure. To mitigate potential inaccuracies in cross-sectional area measurements due to surface topography, and considering the cost and feasibility of alternative methods, a correlation between surface topography and caliper measurements was established.

The engineering stress is then calculated with Equation (3.8). Where A_c was determined differently for L-PBF and DED specimens. For the L-PBF specimens, twice the Sp value was subtracted from both the width and the thickness, as shown in Equation (3.7) ($A_c = (w - 2Sp) \times (t - 2Sp)$). In contrast, due to the smooth surfaces on the width of the DED specimens resulting from EDM, the cross-section area was determined by subtracting the Sp value from the thickness before multiplying by the width to calculate the area, as shown in Equation (3.6) ($A_c = (w) \times (t - Sp)$).

It is important to note that for L-PBF specimens, the calculated cross-sectional area was related to the μCT area measurements [40], whereas the the cross-sectional area for DED specimens was derived from stress-strain measurements of polished specimens and the minimum μCT area [124]. Other studies have also explored the correlation between caliper-measured areas and sur-

face topography values for calculating the cross-sectional areas of AM specimens [75, 76, 77, 78].

Figure 4.30 provides the engineering stress-strain curves for specimens with the (a) as-printed surface and (b) a comparison between specimens tested with the as-printed surface and specimens with a machined or polished surface to investigate the effects of surface topography on the tensile response. In addition, the measured material properties for specimens with the as-printed surface, including the Young's modulus, YS, UTS, and elongation, are displayed in Table 4.10.

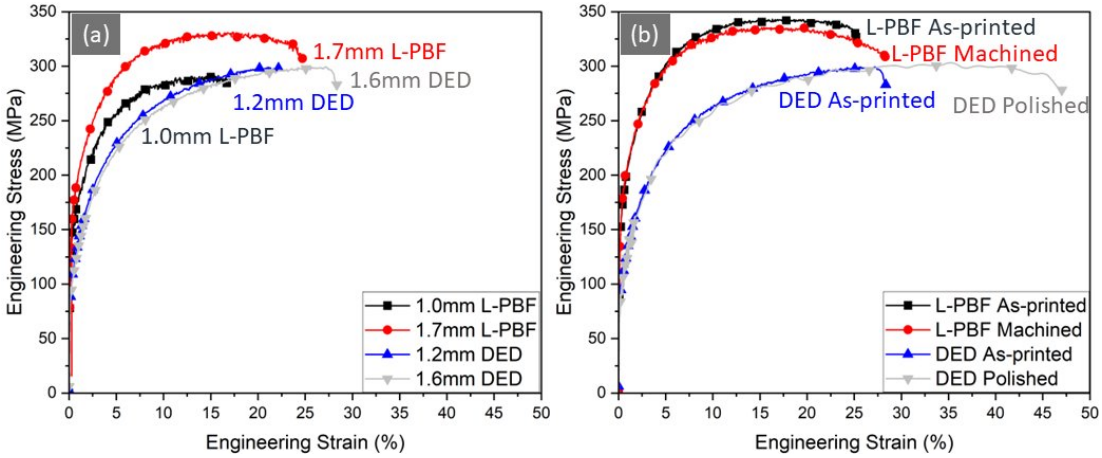

Figure 4.30: Engineering stress-strain curves for (a) specimens with the as-printed surfaces and (b) a comparison between specimens with the as-printed surfaces and specimens with a surface finish, either polished or machined.

Table 4.10: Mechanical properties of L-PBF and DED specimens tested with the as-printed surface.

	Young's Modulus (GPa)	**YS** (MPa)	**UTS** (MPa)	**Elongation** (%)
1.0mm - L-PBF	72 ±26.9	145 ±4.2	287 ±9.9	20 ±3.0
1.7mm - L-PBF	84 ±12.3	165 ±2.4	331 ±5.9	25 ±2.2
1.2mm - DED	62 ±3.3	101 ±6.3	282 ±12.3	19 ±2.6
1.6mm - DED	70 ±14.1	102 ±9.0	296 ±2.6	30 ±3.6

L-PBF specimens with the as-printed surface depict a decrease in strength of over 13% and over 20% reduction in elongation as the specimen thickness is reduced. This reduction is attributed to increased porosity in thinner specimens [40]. In contrast, DED specimens maintain a relatively consistent strength regardless of specimen thickness. However, the elongation drops by over 36% with decreasing specimen thickness. This behavior is linked to thicker specimens having a larger cross-sectional area to resist crack propagation [124]. Furthermore, it's worth noting that the surface finish resulting from each deposition method influences the mechanical properties differently. The surface topography of L-PBF specimens has little to no significant impact on the mechanical response, resulting in a strength decrease of approximately 6%. In contrast, surface topography significantly affects the mechanical properties of DED specimens, with a 57%

increase in elongation observed for polished specimens compared to as-printed specimens.

A significant disparity in the mechanical response is observed between L-PBF and DED specimens. Firstly, the elongation appears comparable for each thickness in the as-printed conditions. Secondly, the YS of DED specimens is notably lower than L-PBF specimens, regardless of thickness. Additionally, the UTS of both thicknesses of DED specimens is similar to that of the 1.0mm L-PBF specimen but approximately 11% lower than than that of the 1.7mm L-PBF specimen. This variation in strength between L-PBF and DED specimens can be attributed to the Hall-Petch effect [128], which states that reducing the grain size of a material increases its strength, as L-PBF specimens show significantly smaller grains than DED specimens, according to the Hall-Petch effect, given in Equation (2.3). This effect is responsible for the higher ductility observed on DED specimens due to their larger grain size when compared to L-PBF specimens.

4.3.5 Fractography

Fractography was conducted on specimens after tensile testing to investigate the predominant failure mechanisms associated with each deposition method. It is important to note that, for the analysis, L-PBF specimens, on the left, were mounted and polished, whereas DED specimens remained in their as-printed condition. This was done to highlight the deformation mechanisms observed in each deposition process. Figure 4.31 display postmortem SEM images perpendicular to the fracture plane for both L-PBF and DED specimens.

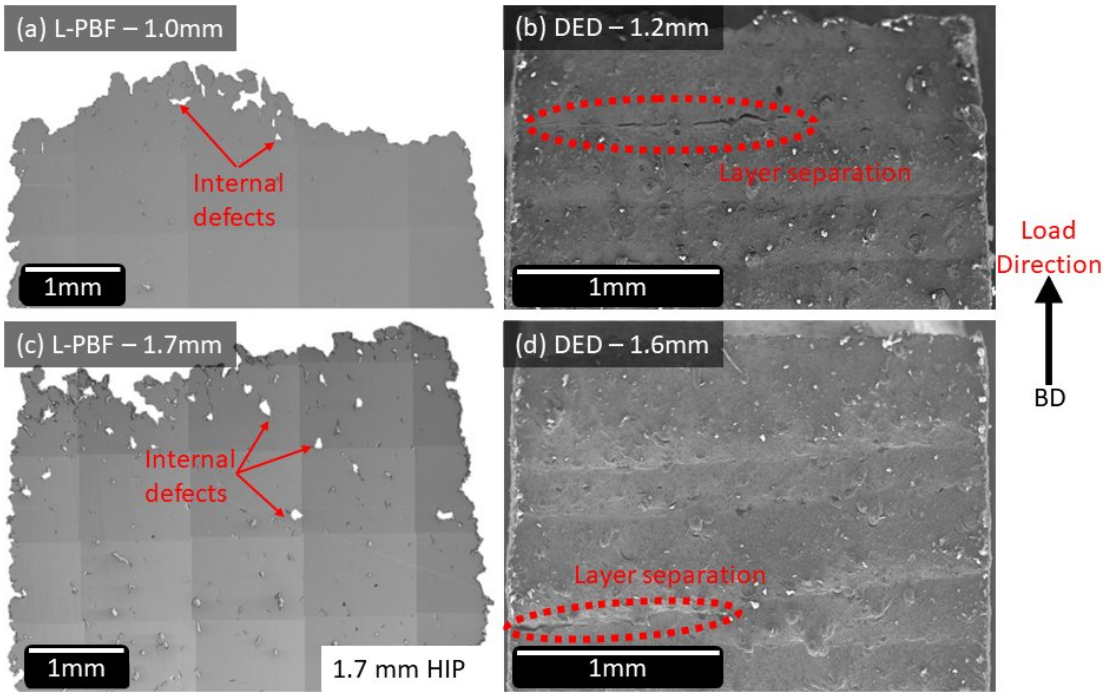

Figure 4.31: SEM images perpendicular to the fracture plane of (a) and (c) L-PBF specimens and (b) and (d) DED specimens.

In L-PBF specimens, the dominant failure mechanism is associated with internal defects. Extensive porosity is evident on the specimen, with these pores contributing significantly to the propagation of cracks in specimens of both thicknesses. Porosity growth and coalescence is a common failure mode on ductile materials [129]. The clustering of pores promotes their coalescence, resulting in an accelerated growth pores [130]. In contrast, DED specimens exhibited minimal porosity and thus do not significantly influence specimen fracture. Instead, the failure in DED specimens is primarily attributed to the separation of deposited layers, along the interlayers. The interlayers are a source of stress concentrations,

which are capable of triggering crack initiation [71], and are also a weak point as it has a smaller cross-sectional area, having less material to resist crack propagation.

4.4 Size Effects and Fatigue on Laser Powder Bed Fusion

The influence of component size on fatigue strength has been well documented in previous studies [35, 131, 132, 133]. Typically, an increase in component size is associated with a reduction in fatigue strength. This phenomenon is a result of fatigue initiation from mechanical discontinuities within the material, often stemming from undetected flaws. Thus, increasing the volume of material in a component increases the probability of finding a critical-sized flaw. For instance, EN-GJS-400-18-LT, a ductile cast iron used in wind turbine components, exhibited a higher fatigue strength for 21mm diameter specimens compared to 50mm diameter specimens. This discrepancy was attributed to the lower cooling rates in thicker blocks, resulting in reduced nodularity and nodule size, decreasing the fatigue strength [133]. Additionally, Sun *et al.* estimated that the fatigue strength for a full-scale railway axle (EA4T) at a 90% survival probability is 33% lower than that of 4mm specimens, at a fatigue life of 10^6 cycles [131].

However, while a decrease in fatigue strength with increasing specimen size is observed, the opposite trend has also been reported. Wang *et al.* [134] found that the fatigue strength of 18CrNiMo6-7 alloy steel increased as the specimen diameter increased from 3mm to 7.5mm. One potential explanation for this behavior was the presence of residual compressive stress on the surface of larger specimens, which slightly exceeded that of smaller specimens. Bu [135] also ob-

served that the the crack propagation areas were consistent across specimens of different sizes through fracture analysis of aviation ear flaps made from aluminum alloy. This suggests that the absolute length of fatigue cracks was longer for larger specimens. Furthermore, it is important to recognize that the critical size of a defect increases with increasing component size [133].

Consequently, size effects may lead to an increase or decrease in fatigue strength and life depending on the operative and dominant deformation and failure mechanisms for a particular material. Since components manufactured by AM typically contain internal defects (*i.e.,* porosity, lack of fusion, etc.), increased surface roughness compared to wrought, microstructural heterogeneities, and residual stresses [27, 136], it would be rational to expect larger AM components to have shorter fatigue lives due to the heightened probability of encountering critical manufacturing induced defects. Nonetheless, the findings from quasi-static tests on AM components have displayed a different trend [40, 124], suggesting different mechanics at play. Thus, technological size effects emerge as a pivotal determinant of the fatigue life of such components.

For this study, a total of 26 specimens were fabricated together in the same build as individual tensile flat bars parallel to the build direction (BD). The specimens were fabricated using GRCop-42 pre-alloyed gas atomized powder on an EOS M400-1 Series printer with a Yb-fiber IR laser, on a stainless steel base plate coated with a nickel-based alloy (IN718). Specimens were deposited with a power of 300W, 1000mm s^{-1}, 0.04mm layer thickness, and 0.1mm hatching distance, employing a continuous scan pattern was used during the deposition process to

prevent melt pool contamination with ejecta. Which could be detrimental to mechanical properties due to possible lack of fusion defects [137, 138]. Finally, a contour pattern was used to negate the effects the infill pattern has on the surface.

Two different thicknesses are considered, 2.1mm and 1.5mm, with a specimen design dimensions given in Figure 4.1. Where the 2.1mm specimens show a comparable UTS to standard size specimens, approximately 340MPa for HIP'd GRCop-42 specimens [40, 52], while the 1.5mm specimens show a decrease in YS, UTS, and elongation [40].

4.4.1 Surface Analysis

Surface topography, encompassing form, waviness, and roughness, of AM acomponents has been identified as a prominent source of size effects in various studies. Notably, L-PBF Inconel 718 thin walls demonstrated a significantly shorter high cycle fatigue (HCF) life for specimens with as-printed surface when compared to machined specimens [139]. Another study concerning L-PBF Ti-6Al-4V highlighted the pivotal role of as-printed surface roughness in reducing the fatigue life, in the low cycle fatigue (LCF) regime [140]. Additionally, research on L-PBF 304 L stainless steel (SS) [141] and L-PBF 316L SS [142] emphasized that surface roughness served and the primary site for fatigue crack initiation in specimens with as-printed surfaces.

Furthermore, aside from stress concentration and potential crack initiation sites, surface topography also introduced measurement inaccuracies when quantifying the effective cross-sectional area. Thus, when determining the properties of

specimens with varying sizes, it is important to accurately measure the effective cross-sectional area, as the surface topography plays a major role in AM components. This phenomenon has been corroborated in various materials and AM deposition techniques, such as L-PBF 316L SS [71], L-PBF 304L SS [92], electron beam melting Ti64 [92], and DED GRCop-42 [124].

Given that fatigue cracks tend to initiate on the surface, it is essential to investigate the overall surface topography of specimens. For these reasons, this study conducted areal measurements at three randomly selected location on three distinct specimens for each condition (*i.e.,* thickness and heat treatment condition), providing quantitative metrics for surface topography characterization. The following parameters were measured for surface characterization: average areal surface roughness (Sa), root mean square surface roughness (Sq), max measured valley depth (Sv), maximum measured peak height (Sp), and the collective range of maximum height of the surface (Sz). Table 4.11 shows the measured values of Sa, Sq, Sv, Sp, and Sz calculated in accordance with equations Equation (3.1), Equation (3.2), Equation (3.3), Equation (3.4), and Equation (3.5), respectively.

Table 4.11: Measured surface topography values obtained for both thicknesses and heat treatment conditions.

		Sa	Sq	Sv	Sp	Sz
1.5mm	as-built	19.9 ±1.5	24.8 ±1.8	79.4 ±8.7	90.3 ±10.3	169.6 ±12.3
	HIP	20.0 ±2.8	25.1 ±3.3	74.5 ±7.9	90.7 ±14.6	165.2 ±18.2
2.1mm	as-built	20.9 ±2.3	26.0 ±2.5	76.7 ±5.3	83.7 ±8.3	160.4 ±10.8
	HIP	20.3 ±2.0	25.2 ±2.3	73.2 ±10.5	89.2 ±9.0	162.4 ±17.1

The specimens exhibited similar values for all quantified surface topographic features, indicating that the surface topography of the AM specimens remains consistent across varying specimen thickness or heat treatment conditions. It has been suggested that stress concentrations resulting from the surface roughness of specimens lead to a decrease in YS, UTS, elongation, and Young's Modulus [71, 92, 93]. Furthermore, the magnitude of the stress concentration also depends on the magnitude of the surface roughness [94]. Therefore, it is plausible that the present surface roughness on these specimens may not be sufficiently large to induce significant stress concentration. Nonetheless, it still has the potential to result in inaccuracies when measuring cross-sectional areas with contact devices, such as calipers, and need to be accounted for.

Furthermore, specimens with varying thicknesses but a similar surface roughness imply that surface irregularities occupy a larger percentage of the

caliper measured cross-sectional area. Consequently, thinner specimens have a smaller load-bearing area compared to their thicker counterparts.

4.4.2 Quasi-static Tests

Quasi-static tensile tests were conducted to obtain mechanical properties, including YS, UTS, and elongation. These properties served as basis for establishing the appropriate parameters for subsequent fatigue testing. In this regard, two specimens were subjected to tensile tests for each thickness and heat treatment condition (as-built and HIP) to verify the ramifications of size effects n the mechanical response of specimens.

Figure 4.32 displays the engineering stress-strain curves for both thicknesses in the (a) as-built and (b) HIP'd conditions. Additionally, Figure 4.33 displays a bar chart for the YS, UTS, and elongation for 1.5mm and 2.1mm specimens in the same conditions. The evident size effect that is observed across both as-built and HIP'd specimens highlights the persistent size effects, which remain independent of, or are not entirely mitigated by, the employed heat treatment.

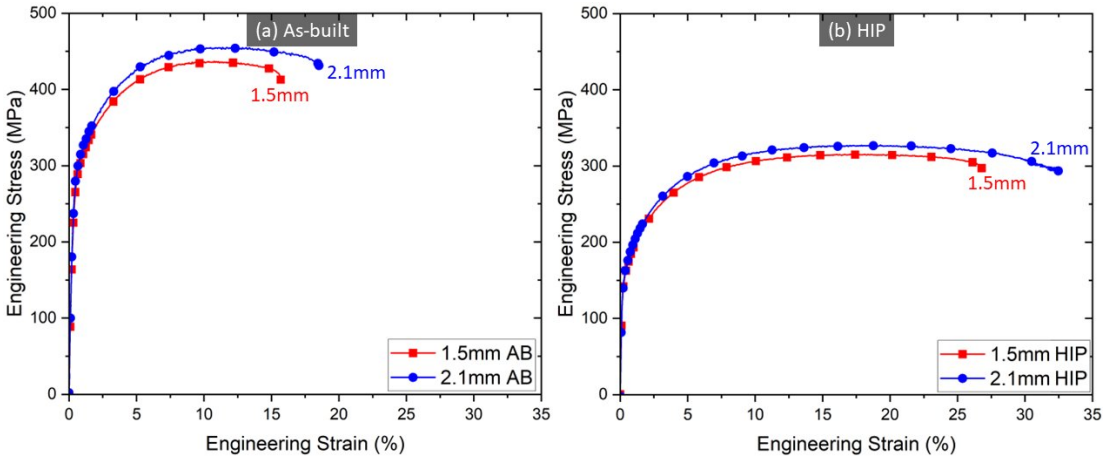

Figure 4.32: Quasi-static results for (a) as-built and (b) HIP'd specimens for both thicknesses. A distinct size effect is observed, where the 2.1mm specimens exhibit higher elongation and strength relative to their 1.5mm counterparts. Additionally, HIP'ing lowered the strength of specimens for both thicknesses but increase the total elongation prior to failure.

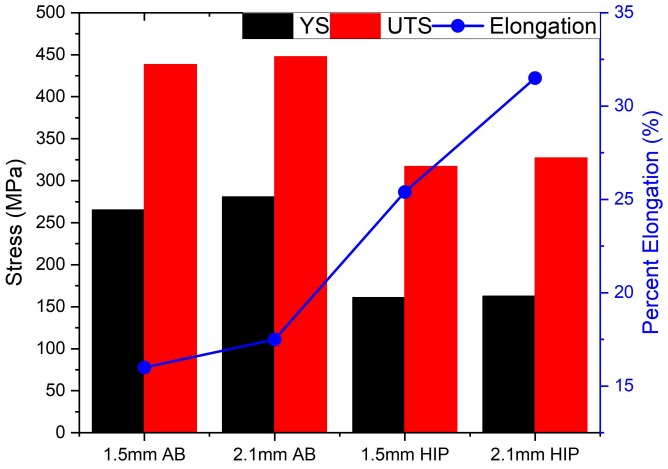

Figure 4.33: YS, UTS, and elongation comparison for 1.5mm and 2.1mm specimens in both as-built and HIP'd conditions.

It is noteworthy to mention that the authors have previously documented the quasi-static behavior of L-PBF GRCop-42 [40]. Consequently, only two specimens were utilized for tensile testing to corroborate that the current specimens

exhibited behavior consistent with previously reported results. It is also important to note that, while the printers and specific process parameters, including laser powder and scanning speed, differed between both sets of specimens, the energy density remained relatively constant (approximately $75\,\mathrm{J\,mm^{-3}}$). The tested specimens displayed similar trends, featuring a decreasing strength and elongation with decreasing thickness. This observation suggests that the size effects are not solely contingent on the specific printer and specific process parameters.

Comparing HIP'd specimens to their as-built counterparts reveals a significant decrease in both YS and UTS across all specimens. Notably, the 2.1mm specimens exhibited a 42% decrease in YS and a 27% decrease in UTS, while the 1.5mm specimens showed a 39% decrease in YS and a 28% UTS reduction. This behavior is expected, as HIP is known and employed to relieve residual stresses in L-PBF metals [99], which could be detrimental to the mechanical properties [143]. Conversely, HIP'ing led to an increase in elongation for both specimen thicknesses. Specifically, 1.5mm specimens exhibited a 59% increase in elongation, while the 2.1mm specimens showed an 80% elongation increase. HIP's positive influence on elongation has also been documented for Inconel 718, improving it by 20% compared to as-built specimens [17, 139].

Moreover, HIP induced a minor alteration in the magnitude difference of strength and elongation between the two thicknesses. In as-built specimens, the YS, UTS, and elongation were 6%, 2%, and 9% higher, respectively, for the 2.1mm specimens compared to the 1.5mm specimens. In the case of HIP'd specimens, the 2.1mm specimens exhibited a 1% higher YS, 3% higher UTS, and 19% higher

elongation compared to the 1.5mm specimens. Although the difference in strength between the two thicknesses remains relatively small, a significantly difference in elongation is observed in HIP'd specimens. The higher elongation is attributed to the reduction in porosity following HIP, a trend consistent with prior observations showing increased elongation to failure with thicker specimens for GRCop-42 [40] and Inconel 718 [139].

Table 4.12 details the Young's Modulus, YS, UTS, and percent elongation values for both 1.5mm and 2.1mm specimens in both as-built and HIP'd conditions.

Table 4.12: Average mechanical properties along with their respective standard deviations obtained from the quasi-static test.

	Condition	Young's Modulus (GPa)	YS (MPa)	UTS (MPa)	Elongation (%)
1.5mm	As-built	96.1 ±3.3	265.5 ±0.0	438.4 ±1.2	16.0 ±0.3
	HIP	82.7 ±2.0	161.0 ±0.8	317.1 ±1.8	25.4 ±1.3
2.1mm	As-built	82.4 ±1.1	281.0 ±0.8	447.9 ±1.0	17.5 ±1.7
	HIP	94.5 ±1.7	162.8 ±0.0	327.2 ±0.4	31.5 ±0.0

A reduction in both YS and UTS, along with decreased elongation, is evident as the specimen thickness decreases from 2.1mm to 1.5mm in both as-built and HIP'd conditions. Similar trends of declining YS, UTS, elongation, and Young's modulus have been documented in previous studies involving various

metals. Notably, L-PBF 316L stainless steel [71], L-PBF 304L stainless steel [92], and electron beam melting Ti64 [92] exhibited a similar behavior. These reductions were attributed to the surface roughness of the specimens, which generates stress concentrations and reduced the load-bearing area.

Additionally, GRCop-42 specimens also displayed a reduced strength and elongation with decreasing specimen thickness in a prior study [40]. However, in the case of GRCop-42, the decrease in strength and elongation were attributed to increased internal defects as specimen thickness decreased. It is well established that porosity has detrimental effects on the mechanical properties of AM materials, as evidenced in studies involving AM Ti-6Al-4V [96, 24], AM stainless steels [97], and others materials [98].

4.4.3 Fatigue Tests

The influence of specimen size and heat treatment condition regarding fatigue life were investigated. Tests were conducted in a load-controlled tensile-tensile ($R = 0.1$) experiment setup, at ambient temperature and air. Each test configuration consisted of eight specimens for each thickness in both as-built and HIP'd condition, loaded along the BD axis, with four specimens for each setup. Testing was carried out either until failure or up to 10^6 cycles, employing $\sigma_{max} = \frac{2}{3}\sigma_y$, where σ_y was determined as the 0.2% YS offset from the tensile tests detailed in section Section 4.4.2. Table 4.13 provides an overview of the fatigue test results for each thickness, heat treatment condition, cycles to failure, and applied stress. Note that the applied stress, being defined in relation to the YS, exhibited

variations across different thickness and heat treatment condition combinations. Figure 4.34 portrays the S-N (stress-number of cycles) graphs derived from the fatigue tests. Notably, thinner specimens exhibited a higher degree of scatter.

Table 4.13: HCF life cycles are summarized for 1.5mm and 2.1mm specimens in both as-built and HIP'd conditions. HIP'd specimens consistently withstood 10^6 cycles without failing, while as-built specimens failed at significantly lower cycles.

Specimen	**Condition**	**Cycles**	**Stress** (MPa)
1.5mm	as-built	125,014	175
	as-built	71,493	175
	as-built	79,964	175
	as-built	119,105	175
	HIP	1,000,000	104
	HIP	1,000,000	104
	HIP	1,000,000	104
	HIP	1,000,000	104
2.1mm	as-built	101,172	193
	as-built	111,321	193
	as-built	99,668	193
	as-built	97,085	193
	HIP	1,000,000	110
	HIP	1,000,000	110
	HIP	1,000,000	110
	HIP	1,000,000	110

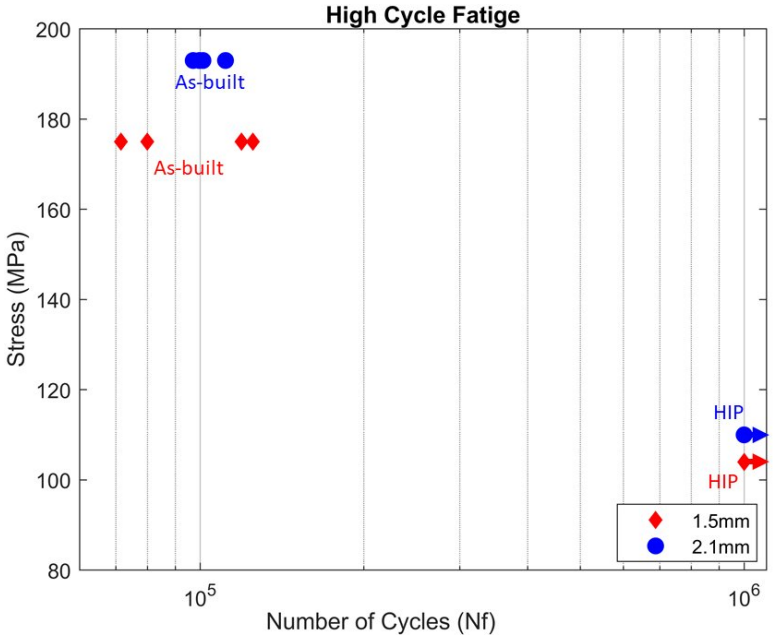

Figure 4.34: S-N graphs for both (a) 1.5mm and (b) 2.1mm specimens in as-built and HIP'd conditions reveal that as-built specimens failed at approximately 10^5 cycles for both thicknesses, whereas HIP'd specimens endured testing until 10^6 cycles before the test was stopped.

As-built 1.5mm specimens exhibited an average of 98,894 ±23,421 cycles to failure, with greater variability in comparison to as-built 2.1mm specimens, which failed at an average of 102,312 ±5,403 cycles to failure. In contrast, HIP'd specimens successfully endured testing for 10^6 cycles without failing, regardless of thickness. Moreover, both thicknesses demonstrated relatively consistent cycles to failure for the as-built and HIP'd specimens, with the latter exhibiting significantly higher fatigue life. This indicates that HIP'ing greatly enhances the fatigue life of L-PBF GRCop-42 due to its ability on minimize internal porosity. This phenomenon was observed for selective laser melting (SLM) $AlSi_{10}Mg$, where the improvement of fatigue strength was attributed to a 64% decrease in porosity and

the formation of intermetallic phases, improving the resistance to fatigue crack growth [144]. A similar behavior was also observed in Inconel 718 [139], where it was found that a lack of pores in the specimens delayed the fracture, leading to increased elongation in HIP'd specimens when compared to as-built specimens.

Furthermore, in AM alloys, it has been reported that surface roughness plays a larger role in the fatigue strength of as-built specimens, as near surface defects tend to have higher stress concentrations than internal defects [136]. However, once specimens are machined, cracks are seen to initiate within internal defects [145]. Other material attributes of AM alloys, such as microstructural inhomogeneities, residual stresses, and anisotropy have a more substantial influence on response once the effects of surface roughness and internal defects are minimized [27].

Given that all specimens had an as-printed surfaces, with no additional surface finishing steps applied, it is presumed that internal defects have a more significant influence on the reduction in fatigue life compared to surface conditions. This is due to the reduction in internal defects in HIP'd specimens, resulting in an extended fatigue life. Additionally, since both thicknesses experienced a similar cycle to failure at stresses of approximately 66% for their respective YS, it is assumed that at an equivalent stress levels, thicker specimens would exhibit longer fatigue life than their thinner counterparts. This assumption is reasonable as the specimens would have a similar crack propagation rate under the same amplitude. Consequently, thicker specimens would possess longer crack propagation lives than their thinner counterparts [133].

4.4.4 Porosity Measurements

Internal defects and microstructural characteristics resulting from the AM process are contributing factors to the observed size effect. A study involving L-PBF GRCop-42 [40] identified internal porosity as the primary driver of size effects during quasi-static testing as specimens thickness decreased from 2mm to 0.7mm. Additionally, L-PBF 316L tensile specimens demonstrated finer grains near the surface, resulting from the outer contour pass, which covered a larger percentage of the cross-sectional area in thinner specimens. This phenomenon led to an increase in yield strength (YS) and a decrease in elongation as the specimen width decreased [146]. Moreover, the influence of surface roughness diminished compared to internal defects when a larger lack of fusion defects were present [147]. Therefore, internal defects need to be fully characterized to understand their influence on quasi-static and fatigue behavior of AM components.

Defects resulting from AM deposition methods can be mitigated through post-fabrication processes such as heat treatments and machining. Notably, HIP has demonstrated efficacy in reducing the internal defects in AM components [36, 37, 38, 39]. It is noteworthy to mention that HIP's effectiveness is limited in addressing surface-connected or near surface porosity [38, 39]. Additionally, HIP is generally ineffective in reducing porosity in fine structures including thin walls and lattice structures [40, 2]. Furthermore, larger pores may be flattened during HIP, leading to morphological changes that cannot be detected via µCT and may detrimentally impact fatigue life [27].

To comprehensively assess the role of internal defects in damage evolution and crack propagation, the porosity was quantified in pristine specimens for both thicknesses and heat treatment conditions via µCT scans. Porosity was also assessed for one specimen of each thickness in the HIP'd condition after undergoing fatigue testing to investigate changes in porosity distribution during cyclic loading. It is important to note that µCT scans were conducted prior to the detection of any visible cracks to avoid interference from fracture surfaces or micro-cracking. Table 4.14 summarizes the scanned volume, total pore volume, and percent porosity for both 1.5mm and 2.1mm specimens in the as-built pristine, HIP pristine, and HIP fatigued conditions.

Table 4.14: Total scanned volume, total pore volume, and calculated porosity percentage for specimens in each thickness and heat treatment, and testing condition.

	Condition	**Total Volume** (mm^3)	**Pore Volume** (mm^3)	**Porosity** (%)
1.5mm	as-built	94.87	0.19	0.20
	HIP pristine	82.48	0.07	0.08
	HIP fatigued	97.76	0.03	0.03
2.1mm	as-built	142.78	0.08	0.06
	HIP pristine	114.39	0.06	0.05
	HIP fatigued	151.49	0.02	0.01

The overall porosity percentage is higher for thinner specimens regardless of heat treatment condition. In the as-built condition, the 1.5mm specimens exhibited over three times the porosity percentage of the 2.1mm specimens. HIP'd specimens show a reduction in porosity for both thicknesses, with the greatest impact observed in thinner specimens. However, 1.5mm specimens continue to exhibit a higher porosity percentage than their 2.1mm counterparts. HIP was shown to be effective in reducing internal porosity, as evidenced by the decreased volume percentage in HIP'd specimens for both thicknesses when compared to the as-built specimens. This observation aligns with prior research findings [40, 37, 81]. Figure 4.35 showcases the 3D reconstruction of µCT scans and bar charts, illustrating porosity percentages and their respective volumetric pore sizes for specimens in the as-built pristine, HIP'd pristine and HIP'd fatigued conditions.

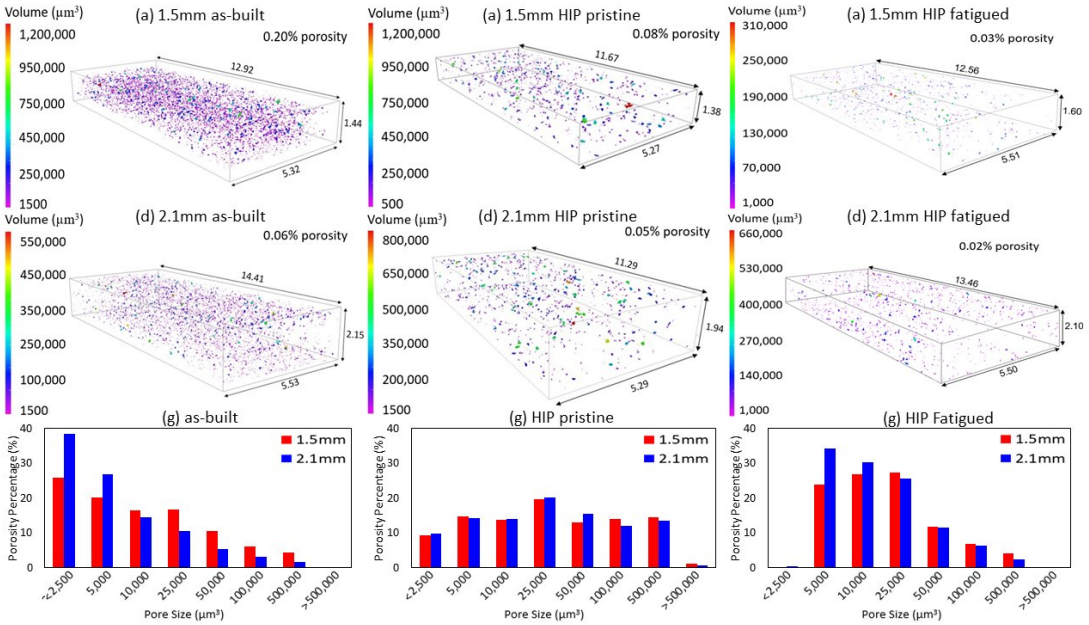

Figure 4.35: 3D µCT data reconstruction for the porosity analysis and the number of pores with their respective pore volume for (a)(d)(g) as-built specimens, (b)(e)(h) HIP'd pristine specimens prior to fatigue, and (c)(f)(i) HIP'd specimens post fatigue. HIP'd pristine is shown to significantly reduce the porosity percentage compared to as-built specimens, especially small pores. However, on HIP'd post fatigue specimens, small and medium pore percentages increased, with a lower percentage of larger pores.

The analysis of porosity reveals that in as-built specimens, the percentage of smaller pores is higher for 2.1mm specimens (up to 5,000µm^3). However, for pores larger than 5,000µm^3, 1.5mm specimens exhibit a higher percentage. In HIP'd pristine specimens, the pore percentages are comparable for both thicknesses relative to their respective pore volumes. Furthermore, a more substantial reduction in smaller pores, relative to larger pores, indicates that HIP is more effective in closing smaller pores (<25,000 µm^3). These results are consistent with a previously published paper on size effects of GRCop-42 [40], which demonstrated that HIP had little effect on addressing larger pores. In HIP'd fatigued specimens,

the percentage of smaller pores (ranging from 2,500µm^3 to 25,000µm^3) is higher compared to HIP'd pristine specimens. However, pores larger than 25,000µm^3 experience a progressive reduction when compared to HIP'd pristine specimens. Additionally, 2.1mm specimens exhibited a higher percentage of small pores ($<$ 10,000µm^3) compared to 1.5mm specimens, while pores larger than 10,000µm^3 are higher on 1.5mm specimens.

Figure 4.36 presents the percentage of porosity associated with each pore volume for 1.5mm and 2.1mm specimens in the as-built condition, pristine HIP'd condition, and fatigued HIP'd condition.

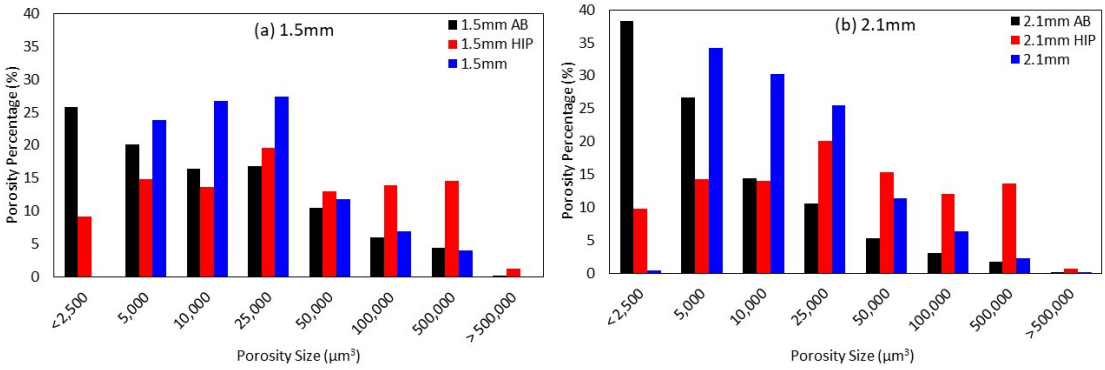

Figure 4.36: Porosity percentage with respect to pore volume for (a) 1.5mm and (b) 2.1mm specimens in the pristine as-built condition, pristine HIP'd condition, and fatigued HIP'd condition.

The near absence of pores smaller than 2,500µm^3 and the increase in pores between 5,000 and 25,000µm^3 post fatigue testing suggest void coalescence. The progressive decrease in the percentage of larger pores ($<$ 25,000µm^3) is likely an artifact of the increase in smaller pores, as evidenced by a 30% and 43% increase for pores smaller than 25,000µm^3 for fatigued 1.5mm and 2.1mm specimens compared to the pristine specimens, respectively. This decrease in larger pores may

be due to the redistribution of material caused by the closure of smaller pores, reducing the percentage of larger pores. Previous studies have indicated that during HCF of α-iron at a constant stress amplitude of 70% of the YS, pore growth was more likely than pore formation, leading to an increase in pore size without a significant change in the overall pore ratio. This phenomenon occurred in specimens subjected to cycling between 37%-73% of the fatigue life [148]. In contrast, during HCF of aluminum 7075-T6 under tensile mean stresses of 0MPa and 194MPa for 75% of the fatigue life led to pore formation instead of growth. This was attributed to the increase in pores with an area of 10µm^2, with no significant pores larger than that size being found [149].

To directly establish a correlation between fatigue cycling and internal porosity, two additional 2.1mm specimens were subjected to µCT scans before and after undergoing fatigue testing to 10^6 cycles at 110 MPa (two-thirds of the YS). The porosity of these specimens was then measured at the same location. Figure 4.37 illustrates the porosity percentage found in HIP'd 2.1mm specimen in the pristine and post fatigue conditions. The specimen underwent the following sequence: (1) µCT - (2) HCF testing - (3) µCT.

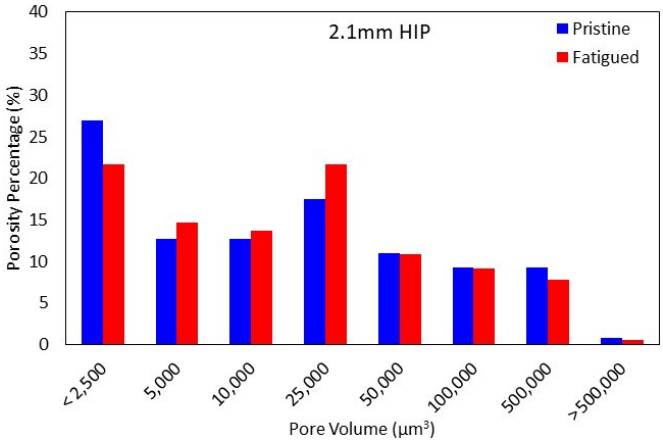

Figure 4.37: Porosity percentage with respect to the pore volume found on a HIP'd 2.1mm specimen before and after fatigue testing to 10^6 cycles. Porosity increases for pores larger than 2,500µm up to 25,000µm for fatigued specimens and a similar porosity percentage or slight decay for pores larger than 25,000µm.

Similar to previous findings, the porosity percentage increased for pores with sizes ranging from 2,500µm^3 to 25,000µm^3 after fatigue. In contrast, pores larger than 25,000µm^3 displayed a similar or slightly higher pore percentage for pristine specimens. The trend indicates that smaller pores decreased while larger pores increased or remained unchanged after fatigue. Analysis of the total number of pores in the specimen indicated an overall reduction in porosity for all pore size ranges, along with a decrease in total pore volume from 0.07mm^3 for pristine specimens to 0.04mm^3 for tested specimens. However, a larger reduction ($\approx$48%) was observed in pores smaller than 2,500µm^3, suggesting that pore growth was more likely than new pore nucleation.

4.4.4.1 Quasi-static test post fatigue

The existing fatigue history of a component has been demonstrated to influence its mechanical properties, including parameters such as YS, UTS, and elongation as evidenced in previous studies [148, 149, 150]. However, its crucial to recognize that the mechanical response of fatigued specimens cannot be readily extrapolated, as the underlying mechanisms by which a material yields and fails are not the same as the ones active in fatigue. Additionally, factors such as microstructure, internal defects, and surface topography have varying effects on fatigue behavior compared to YS and ductility. Thus, the damage accumulated during cyclic loading was investigated through quasi-static tests of fatigued specimens.

To investigate the consequence of cyclic loading on the subsequent mechanical properties, tensile testing was conducted on one HIP'd specimen for each thickness, 1.5mm and 2.1mm, following fatigue testing. The results of these tests, following fatigue testing to 10^6 cycles at approximately 66% of the YS, are displayed in Figure 4.38, which illustrates the engineering stress-strain response of the 1.5mm and 2.1mm HIP'd specimens.

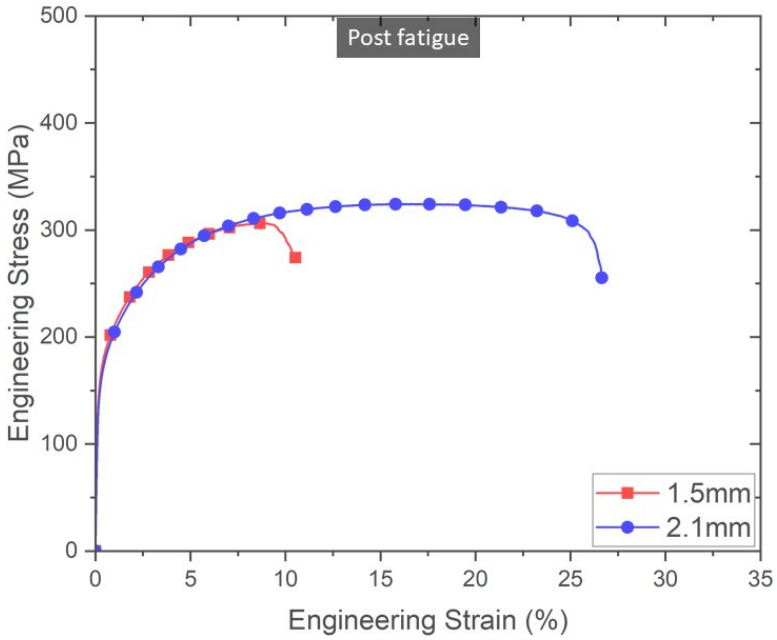

Figure 4.38: Engineering stress-strain plot displaying the response of 1.5mm and 2.1mm HIP specimens after 10^6 cycles. Although both specimens appear to have a decrease in elongation when compared to pristine specimens, 1.5mm specimen displays a significantly lower elongation than the 2.1mm specimen.

Although little change (less than 5%) in the strength was observed for both specimens, there was a considerable reduction in elongation for both HIP'd specimens. 1.5mm specimen exhibited a substantial reduction in elongation, 61%, decreasing from 27% to 11%, while the 2.1mm specimen displayed a 17% reduction in elongation, dropping from 32% to 27%. This decrease in elongation signifies the impact of damage accumulation during fatigue testing, which led to reduced ductility in these specimens.

The more pronounced reduction in elongation observed in the thinner specimen following fatigue loading eludes to a greater degree of damage accumulation in thinner specimens during cyclic loading. Indeck *et al.* [148] reported approx-

imately 20% decrease in YS, UTS, and ductility of α-iron during quasi-static testing after cycling loading to 31%-94% of the fatigue life. Similarly, in the case of aluminum 7075-T6 subjected to 75% of its fatigue life at a mean stress of 194MPa, a 7% decrease in strength was observed, which was attributed to fatigue induced porosity, with no significant impact on elongation [149].

4.4.5 Fractography

Fractography was conducted on specimens post tensile and fatigue testing to gain insights into damage accumulation in the gage section and fracture surface. The specimens were optically imaged perpendicular to the fracture plane, enabling the investigation of damage accumulation in the gage section. Further, fractography was conducted on the fracture surface using an SEM to identify features indicative of ductile and brittle fractures.

Figure 4.39 displays the fractured specimens observed perpendicular to the fracture plane for both 1.5mm and 2.1mm specimens in the as-built and HIP'd conditions. It also includes a comparison between fatigued specimens and quasi-statically tested specimens.

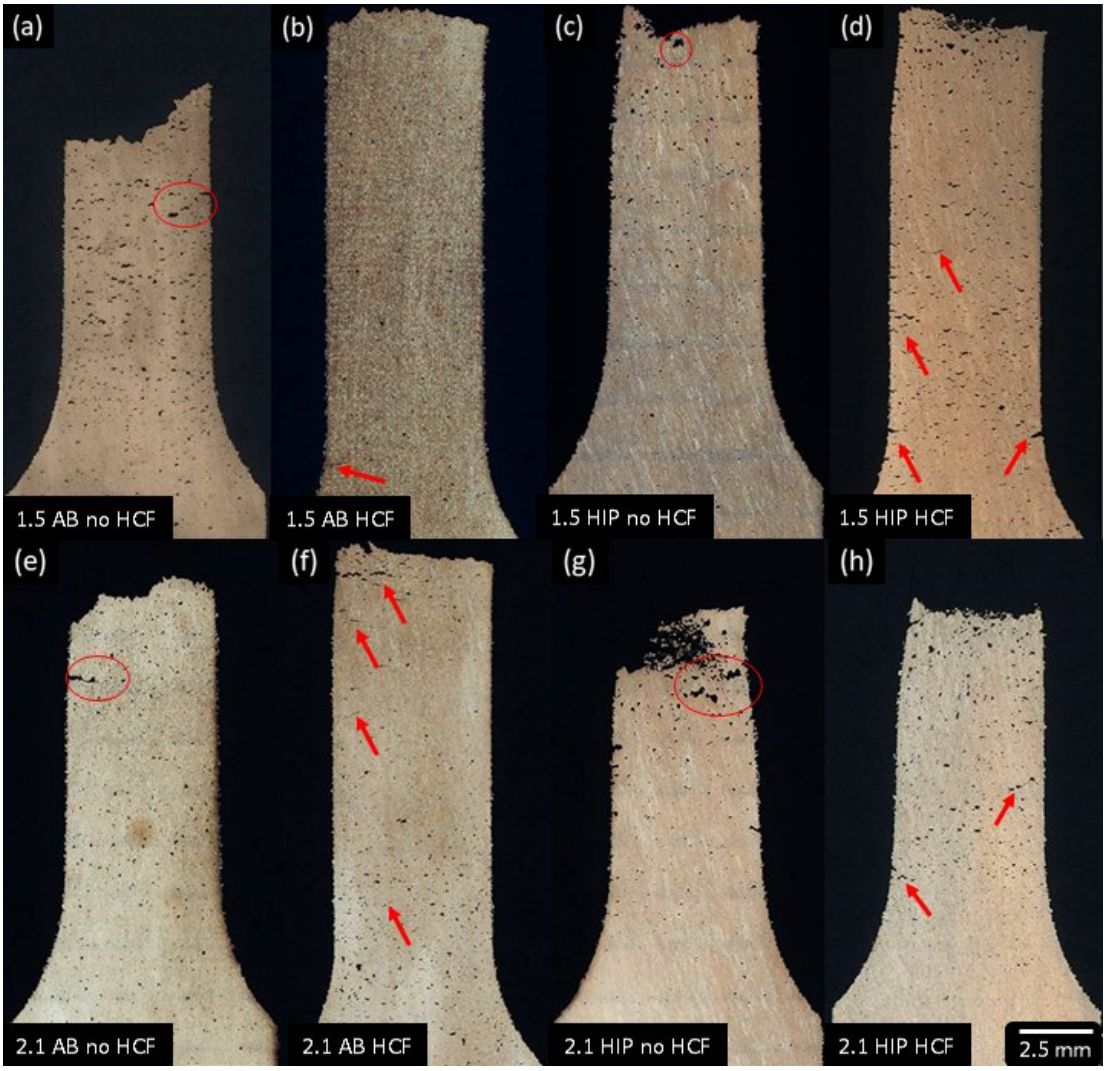

Figure 4.39: Fractured specimens perpendicular to the fracture plane shown (a), (b), (c), and (d) for 1.5mm specimens and (d), (f), (g), and (h) for 2.1mm specimens. Parts (a) and (e) show as-built specimens with no HCF, parts (b) and (f) displays as-built specimens + HCF, parts (c) and (g) displays HIP'd specimens with no HCF, and parts (d) and (h) show HIP'd specimens + HCF. Red circles are used highlight pore growth and coalescing, and red arrows point to secondary cracks and/or pores coalescing.

Fatigued specimens exhibited relatively flat fractures when observed perpendicular to the fractured plane in both as-built and HIP'd conditions. Addi-

tionally, cracks were found to nucleate and propagate perpendicular to the load direction, along the width of the gage section. In contrast, quasi-static tests conducted on pristine specimens resulted in slanted fracture surfaces with visible shear lips, characteristic of ductile overload. Notably, pore coalescence was also observed throughout the gage section, particularly near the fracture surface, for both fatigued and pristine specimens. Seltzman *et al.* [54] found that GRCop-84 tested under quasi-static loading failed due to void nucleation, which originated from the fractured Cr_2Nb intermetallic phase in the copper matrix. This was idenditified through the presence of Cr_2Nb precipitates inside over 80% of the ductile dimples in the fracture surface. Therefore, it is likely that defects near the surface play a more significant role in the fatigue life than pore nucleation originating from fractured Cr_2Nb particles.

Figure 4.40 illustrates the fracture surfaces of 1.5mm and 2.1mm specimens, in both as-built and HIP'd conditions. In the case of as-built specimens, fatigue testing was carried out until failure occurred. In contrast, HIP'd specimens were subjected to 10^6 fatigue cycles and subsequently subjected to quasi-static testing.

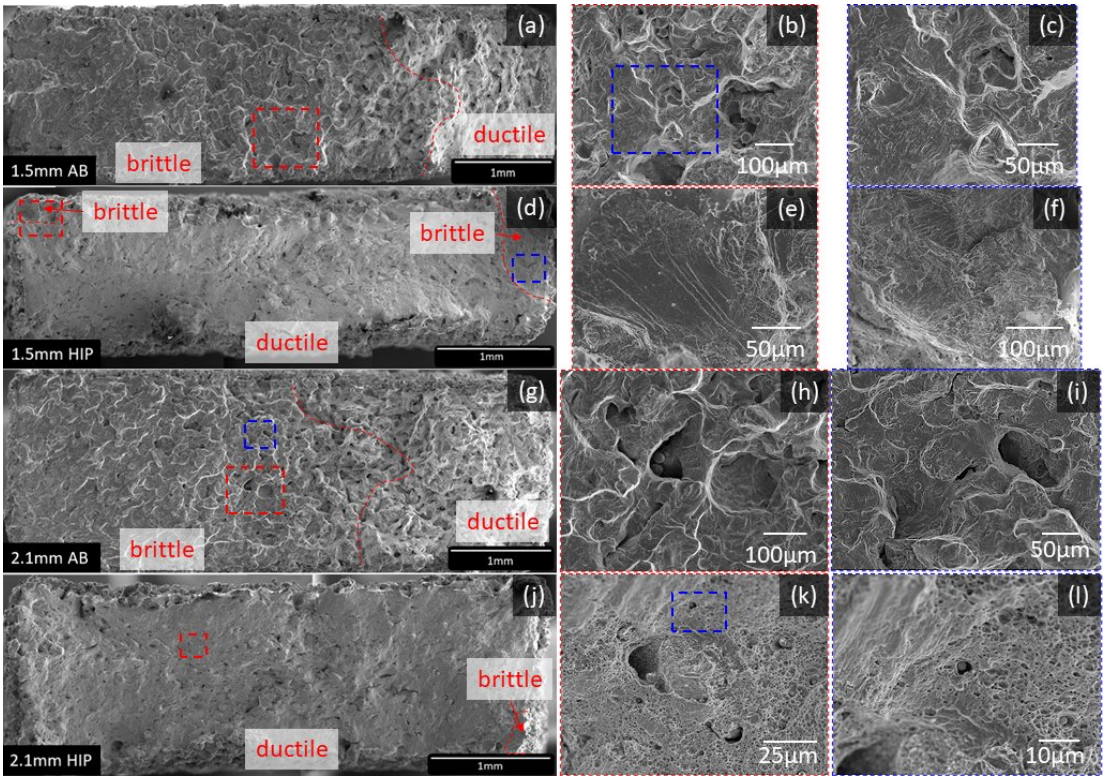

Figure 4.40: Fracture surface for 1.5mm and 2.1mm specimens in both as-built and HIP'd conditions. (a) shows the 1.5mm as-built fracture surface with a zoomed in version at (b) showing unmelted powder and a further zoomed in image (c) showing striation marks. Part (d) shows the 1.5mm HIP'd fracture surface with zoomed in sections at (e) and (f) to show brittle fracture starting at the corners of the specimen. Part (g) shows the 2.1mm as-built fracture surface with two zoomed in locations at (h) and (i) to show unmelted powder and striation marks, respectively. Part (j) shows the 2.1mm HIP'd fracture surface with a zoomed in version (k) showing a defect surrounded by ductile dimples and a further zoomed in image (l) to show a debonded particle from the matrix.

Although all fractured specimens appear to have the fracture starting at or near the surface, the fracture surfaces for as-built and HIP'd specimens demonstrate significant differences. As-built specimens exhibited a substantial portion, over three-quarters, of the fracture surface characterized by brittle features, as evident in Figure 4.40 (a) left-to-right, with the remaining section displaying an

overloaded appearance, indicated by a duller fracture surface. The as-built specimens also exhibited striation marks, which are evidence of cyclic loading effects, and revealed internal porosity along with unmelted powder, as can be seein in Figure 4.40 (b), (c), (h), and (i).

In contrast, HIP'd specimens displayed differences in their fracture surfaces, as depicted in Figure 4.40 (d) and (j). Although brittle features, such as cleavage, were observed at the corners, the majority of the surface exhibited ductile dimples due to overloading during subsequent quasi-static testing. Furthermore, it was noted that certain particles were debonded from the matrix, as illustrated in Figure 4.40 (l), which could lead to porosity formation [54].

The extent of brittle fracture was more pronounced on the fracture surfaces of 1.5mm specimens in comparison to both 2.1mm as-built and HIP'd specimens. This observation aligns with finding of Wang *et al.* [134], who reported that the area corresponding to fatigue propagation in specimens with varying diameters (3mm, 5mm, and 7.5mm) accounted for approximately 50% of the fracture surface. Wang *et al.* attributed this phenomenon to the Paris equation, which states that, under equivalent stress amplitudes, the crack propagation should exhibit similar behavior in specimens of different thicknesses. The size effects on HCF life was also observed in HIP'd thin-walled Inconel 718, where HCF life increased with increasing specimen thickness [139]. Consequently, thicker specimens were found to possess a higher fracture toughness and displayed delayed fracture initiation.

Lastly, it was observed that fractures appear to initiate at the corners of the cross-sectional area, suggesting a propensity for crack formation in close proximity to pores near the material surface or surface defects. This observation aligns with the principle that defects located near the surface create more pronounced stress concentrations compared to internal defects [136].

Chapter 5. Conclusions

This study investigates the size effects on mechanical properties of GRCop-42 specimens fabricated using L-PBF and DED techniques. A comprehensive analysis including quasi-static tensile testing, porosity assessments, surface topography examination, microstructural characterization, high cycle fatigue testing and damage accumulation, and fractography, was conducted to elucidate the observed behaviors. The key findings are summarized as follows:

- **Size effects and deposition method:** In L-PBF specimens, there is an evident reduction in mechanical properties as the specimens thickness decreases. This decline is attributed to increased internal porosity in thinner specimens. However, DED specimens display a different trend, with mechanical property variations primarily linked to specimen orientation. Where, horizontal specimens with as-printed surfaces exhibit comparable YS, UTS, and elongation regardless of thickness or powder composition. Conversely, vertical specimens with as-printed surfaces show approximately 6% higher elongation for thicker specimens compared to thinner ones, as well as a significant reduction in elongation (approximately 47% for thinner and 41% for thicker specimens) compared to horizontal specimens. This is attributed to the larger load-bearing area in thicker specimens, enabling

them to resist stresses generated in interlayers and resist crack propagation through the cross-section. These results highlight that the size effects in GRCop-42 are heavily influenced by the fabrication method.

- **Surface finish:** Surface finish influences the tensile response of L-PBF and DED specimens differently. L-PBF polished specimens exhibits only a minor difference (within 6%) in flow stress compared to as-printed specimens. In contrast, DED polished specimens, whether horizontal or vertical, display consistent elongation and strength, irrespective of specimen thickness or powder composition. This highlights the significance of surface waviness and roughness on the mechanical response, as they create stress concentrations and reduce the effective load-bearing area that resists crack propagation in DED specimens.

- **Cross-sectional area measurement:** The method employed for cross-sectional area measurements significantly influences the reduction in strength with decreasing thickness. Caliper measurements tend to overestimate the load-bearing area, leading to inaccuracies as specimen thickness decreases. Optical microscopy measurements also reflect a decreasing trend in strength with decreasing specimen thickness but lack the accuracy of load-bearing area measurement and is destructive, therefore, this method does not allow the same pristine specimens to be both measured and tested. µCT scans offer precise load-bearing area estimates but also are costly and time-consuming. Therefore, relating surface topography values such as Sp to caliper measurements is suggested as a cost-effective alternative. However,

it is important to note that the equation to obtain the calibrated cross-sectional area, A_c, is dependent on the fabrication method and the post processing steps, such as cutting, machining, grinding, and polishing.

- **Surface topography:** Surface topography in both L-PBF and DED remain consistent across various thicknesses. While this is positive for surface topography predictability, it implies that thinner specimens have a smaller percentage of the measured cross-sectional area acting as a load-bearing area. Additionally, the surface topography varies significantly between the two deposition methods. For instance, L-PBF specimens have relatively flat surfaces with a high degree of partially melted powder and loose powder adhered to the surface. While, DED specimens display significant waviness produced during deposition, resulting in sharp valleys acting as stress concentration zones, facilitating crack initiation. Moreover, the DED deposition method resulted in smaller interlayer areas, contributing to decreased resistance to crack propagation. The stress concentration, coupled with a smaller area, is presumed to account for the lower elongation in as-printed vertical DED specimens. In summary, surface topography played a minor role in the tensile response of L-PBF specimens and a major role in DED specimens.

- **Porosity:** Porosity is known to substantially impact the mechanical properties of specimens and it is highly dependent on deposition method and process parameters. The volume ratio of porosity in L-PBF specimens increases as thickness decreases, with HIP being more effective at reducing

porosity in thicker specimens. Notably, HIP is more efficient in closing smaller pores than larger ones. Furthermore, increased porosity in the thinner specimens promotes the formation of crack networks, reducing strength with decreasing thickness. This is substantiated by the smaller decrease in tensile properties for HIP'd specimens with decreasing thickness compared to as-built specimens. HIP'd DED specimens exhibit minimal porosity in all specimens regardless of build thickness or powder composition, indicating fully dense specimens. This further emphasizes the influence of porosity on tensile property reduction in L-PBF specimens but not in DED specimens.

- **Microstructure and Texture:** Both L-PBF and DED specimens displayed consistent grain structure and crystallographic texture regardless of thickness, powder composition, or heat treatment condition. Grain growth occurs epitaxially along the build direction, with DED specimens exhibiting a striped (zigzag) pattern due to laser path effects while L-PBF specimens displayed epitaxial growth normal to the build direction with a morphology resembling the melt pools forming during the deposition process. Perpendicular to the build direction (SD-TD plane), DED specimens depict small equiaxed grains near the edges built walls with larger grains in the center resulted from the single laser path deposition strategy, having a rapid cooling on the edges and a slow cooling in the center. In contrast, L-PBF specimens do not exhibit a "proper" grain morphology, with the grains' morphology resembling the laser scan spots during the deposition. The crystallographic texture for LPBF and DED specimens also varies significantly for each depo-

sition process. Where, L-PBF displays a weak to moderate <101> texture regardless of thickness and heat treatment condition while DED specimens present a strong {001}<101> texture along the build direction. This indicates that microstructure and texture are more dependent on fabrication methods, build parameters, and scan strategy than on specimen thickness or heat treatment. It is noteworthy to mention that a similar microstructure among specimens of varying thickness suggest fewer grains in thinner specimens, resulting in fewer obstacles to impede dislocation movement, hence, reducing the ductility.

- **Fractography:** Fractography in L-PBF and DED specimens reveal distinct fracture mechanisms. L-PBF specimens do not show surface roughness-induced crack initiation, instead the observed pores along the fracture path suggest that crack propagation was facilitated due to internal porosity. Increased porosity in thinner L-PBF specimens plays a significant role in reducing mechanical properties with decreasing thickness. Conversely, DED specimens displayed interlayer separation upon uniaxial loading, which is more pronounced on vertical specimens due to the loads applied perpendicular to the interlayers. Furthermore, a higher degree of deformation was observed in between each layer for the as-printed DED specimens, and although deformation was also observed on polished specimens, the deformation was significantly lower, indicating internal factors at play in between the layers, requiring further investigation.

- **High cycle fatigue on L-PBF specimens:** As-built specimens exhibited failure after approximately 10^5 cycles, while HIP'd specimens demonstrated enhanced fatigue endurance, withstanding up to 10^6 cycles without failures independent of specimen thickness. Surface topography remained consistent across all specimens, regardless of thickness or heat treatment, and did not significantly influence fatigue life at the given stress level for each specimen. Consequently, it can be hypothesized that HIP significantly enhances fatigue life by reducing internal porosity.

- **Porosity post fatigue:** Post fatigue testing, specimens exhibited a trend of increasing small and medium-size pores percentage, ranging from 2,500µm^3 and 25,000µm^3. Despite an overall reduction in pore counts across all size categories after fatigue, smaller pores (<2,500µm^3) exhibited a greater decrease, implying a greater tendency for existing pores to grow rather than the initiation of new ones. Due to the limited number of specimens used in this investigation, additional work is warranted to further verify these results.

- **Tensile properties post fatigue:** Quasi-static testing conducted after the fatigue regime displayed a reduction in elongation for HIP'd specimens of both thicknesses. Specifically, 2.1mm specimens experienced a 17% decrease in elongation, while 1.5mm specimens demonstrated a substantial reduction, exceeding 60%, in elongation. This indicates that 1.5mm specimens accumulated greater damage during fatigue testing. This observation aligns with fractography findings, which revealed a more extensive area on

the fracture surface featuring brittle features in thinner specimens. It is worth noting that no statistical significance can be attributed to this test as only one specimen of each thickness was quasi-statically tested post fatigue.

- **Fatigue fractography:** The fracture surfaces of fatigued as-built specimens featured brittle fractures covering over half of the fracture surface, alongside significant porosity evident throughout the fracture surface for both specimen thicknesses. In contrast, HIP'd specimens, subjected to 10^6 cycles and subsequently quasi-statically tested to failure, presented fracture initiation on the corners of the specimens, likely initiated during fatigue testing due to their brittle nature, with the remaining of the fracture surface being composed of ductile dimples, indicating a ductile overload fracture during quasi-static testing. Moreover, HIP'd specimens contained minimal porosity on the fracture surface, indicating that porosity has a significant impact on crack propagation during fatigue testing and the reduced fatigue life of as-built specimens.

Chapter 6. Future Work

6.1 Low Cycle Fatigue

LCF behavior characterization is of paramount importance for combustion chambers. Since a constrained liner operating in this environment is subjected to substantial stresses and strains, often exceeding 1%, resulted from thermal expansion and the generation of plastic strains [17]. Given that size effects were observed on the quasi-static and HCF testing, it is expected that they will also play a key role in the LCF life of components. However, it is unclear what characteristic of the components will be dominant. This study aims to investigate the size effects on LCF life of components to identify the dominant characteristics affecting LCF. Furthermore, given the different failure mechanisms at play for L-PBF and DED specimens, it becomes necessary to understand how size effects will impact the LCF life and mechanical properties of both deposition methods. Consequently, to properly design component used in LCF conditions, the mechanical properties need to be investigated considering the fabrication method and any post fabrication treatments including heat treatments and surface finishes.

6.2 Damage Accumulation during Fatigue Life

The purpose of this study is to investigate the effects that cyclic loading has on the subsequent material properties of materials. It was demonstrated that the elongation decreased for both specimen thickness after being cycled for 1,000,000 cycles. However, the number of specimens of specimens used for these results were limited and need to be further explored. Conducting interrupted fatigue testing and evaluating changes in the specimens microstructure, defects, and subsequent mechanical properties can enlighten the deformation mechanisms present and responsible for the decrease in mechanical properties. Moreover, the damage mechanisms were shown to vary significantly for each deposition method. For instance, L-PBF specimens showed porosity growth and coalescence while DED specimens depicted a higher degree of deformation located on the interlayers for specimens with both as-printed and polished surfaces. Therefore, a better understanding of the underlying deformation mechanisms is crucial.

6.3 Size Effects on Other Alloy Systems

Several industries benefit from reducing component size and weight. Understanding how this size reduction influences the mechanical behavior is key for the safe implementation of designs containing thin features. While the stress response is expected to remain constant with reducing cross-sectional area due to the relationship between force and area during quasi-static tensile testing, the current work demonstrates that this is not always the case. Where the yield strength,

ultimate tensile strength, and elongation decreases with decreasing specimen size, which were attributed to internal defects or surface topography. The purpose of this study is to identify if other alloys, specifically AM alloys, depict similar behaviors to GRCop-42 as the specimen size is reduced. As a result, size effects need to be studied for other alloys to ensure that the proper material properties are being employed during the design stage of components, thereby avoiding instances of unwarranted over engineering or premature material failure.

6.4 Influence of Powder Size on Mechanical Properties

The powder size and distribution can influence the deposition process and the resultant material properties. A study on $AlSi_{10}Mg$ alloy revealed that as the mean particle size decreased from 40µm to 9µm, the powder packing density and flowability of the 9µm powder decreased by 30% and 75%, respectively, compared to the 40µm powder. Consequently, the components fabricated using fine powder exhibited lower densities, higher oxygen content, diminished dimensional accuracy, and different microstructures [151]. Therefore, defining the optimal powder size and understanding how it influences resulting mechanical properties has a significant potential for advancing future research.

6.5 Use of Different Energy Sources to Melt GRCop-42

Due to copper's high thermal conduction and high reflectivity to infra-red radiation, it requires higher power inputs for proper melting [12, 152, 153, 154, 155]. Exploring alternative laser sources, such as green or blue lasers, offers the

prospect of reducing power requirements. However, the impact of this on solidification behavior, microstructure, porosity, and resulting mechanical properties remain uncertain. Hence, a comprehensive characterization of the mechanical properties of components fabricated using different laser sources is imperative to assess the feasibility of employing different laser during the deposition of copper-alloy.

6.6 Determining a Critical Flaw Size

Given the significant role of porosity in the mechanical property decrease with specimen size of L-PBF GRCop-42 specimens, establishing the critical flaw size for components of specific thickness becomes increasingly important. Moreover, determining the critical flaw size is essential for the qualification of AM components. Non-destructive assessments on post-build components can then be conducted to ascertain the safety and suitability of AM components for operational conditions.

References

[1] Paul R Gradl and Christopher S Protz. Technology Advancements for Channel Wall Nozzle Manufacturing in Liquid Rocket Engines. *Acta Astronautica*, 174:148–158, 2020.

[2] Kavan Hazeli, Behzad Bahrami Babamiri, Joseph Indeck, Andrew Minor, and Hesam Askari. Microstructure-Topology Relationship Effects on the Quasi-static and Dynamic Behavior of Additively Manufactured Lattice Structures. *Materials & Design*, 176:107826, 2019.

[3] Alex Eliseev. Additive manufacturing goes large – Aerospace prints bigger and better parts, January 2019.

[4] Gerard Shields. 3D Printing Lattice Structures - The Ultimate Guide, February 2022.

[5] C Vyas, G Poologasundarampillai, J Hoyland, and P Bartolo. 3d printing of biocomposites for osteochondral tissue engineering. In *Biomedical Composites*, pages 261–302. Elsevier, 2017.

[6] Xiaoyi Guan and Yaoyao Fiona Zhao. Modeling of the laser powder–based directed energy deposition process for additive manufacturing: a review. *The International Journal of Advanced Manufacturing Technology*, 107(5):1959–1982, 2020.

[7] Robert P Minneci, Eric A Lass, Jeffrey R Bunn, Hahn Choo, and Claudia J Rawn. Copper-based alloys for structural high-heat-flux applications: a review of development, properties, and performance of Cu-rich Cu–Cr–Nb alloys. *International Materials Reviews*, 66(6):394–425, 2021.

[8] SJ Zinkle and SA Fabritsiev. Copper alloys for high heat flux structure applications. *Atomic and Plasma-Material Interaction Data for Fusion (supplement to Nuclear Fusion)*, 5:163, 1994.

[9] Justin Michaud. Advancing rocket propulsion through additive manufacturing, novel surface finishing technologies and public-private partnerships. *Metal-AM*, 6(3):133–143, 2020.

[10] Additive Manufacturing Requirements for Spaceflight Systems, Apr 2021.

[11] Omar Mireles, Carlos Gomez, William Tilson, Travis Belcher, Brandon Abranovic, Mariana Chaidez, John Lopez, Christopher Romanowski, and Lief Wesche. Thermal, Fluid, Mechanical, and Microstructural Property Characterization of Additively Manufactured Lattice Structures. In *Joint Army-Navy-NASA-Air Force (JANNAF) Additive Manufacturing (AM) Technical Interchange Meeting (TIM)*, number M18-6798, 2018.

[12] A Popovich, Vadim Sufiiarov, Igor Polozov, Evgenii Borisov, D Masaylo, and Aleksei Orlov. Microstructure and Mechanical Properties of Additive Manufactured Copper Alloy. *Materials Letters*, 179:38–41, 2016.

[13] Paul R Gradl, Omar R Mireles, Christopher S Protz, and Chance P Garcia. *Metal Additive Manufacturing for Propulsion Applications*. American Institute of Aeronautics and Astronautics, Inc., 2022.

[14] I Yadroitsev, Ph Bertrand, and I Smurov. Parametric Analysis of the Selective Laser Melting Process. *Applied surface science*, 253(19):8064–8069, 2007.

[15] A Liu, Chee Kai Chua, and Kah Fai Leong. Properties of Test Coupons Fabricated by Selective Laser Melting. In *Key Engineering Materials*, volume 447, pages 780–784. Trans Tech Publ, 2010.

[16] A Bauereiß, T Scharowsky, and C Körner. Defect Generation and Propagation Mechanism during Additive Manufacturing by Selective Beam Melting. *Journal of Materials Processing Technology*, 214(11):2522–2528, 2014.

[17] Paul R Gradl, Christopher S Protz, Kenneth Cooper, David Ellis, Laura J Evans, and Chance Garcia. GRCop-42 Development and Hot-fire Testing Using Additive Manufacturing Powder Bed Fusion for Channel-cooled Combustion Chambers. In *AIAA Propulsion and Energy 2019 Forum*, page 4228, 2019.

[18] Abdollah Saboori, Donato Gallo, Sara Biamino, Paolo Fino, and Mariangela Lombardi. An Overview of Additive Manufacturing of Titanium Components by Directed Energy Deposition: Microstructure and Mechanical Properties. *Applied Sciences*, 7(9):883, 2017.

[19] Do-Sik Shim, Gyeong-Yun Baek, Jin-Seon Seo, Gwang-Yong Shin, Kee-Poong Kim, and Ki-Yong Lee. Effect of Layer Thickness Setting on Deposition Characteristics in Direct Energy Deposition (DED) Process. *Optics & Laser Technology*, 86:69–78, 2016.

[20] Paul R Gradl, Christopher S Protz, and Tal Wammen. Additive Manufacturing and Hot-fire Testing of Liquid Rocket Channel Wall Nozzles Using Blown Powder Directed Energy Deposition Inconel 625 and JBK-75 Alloys. In *AIAA Propulsion and Energy 2019 Forum*, page 4362, 2019.

[21] Erfan Azinpour, Roya Darabi, Jose Cesar de Sa, Abel Santos, Josef Hodek, and Jan Dzugan. Fracture Analysis in Directed Energy Deposition (DED) Manufactured 316L Stainless Steel Using a Phase-field Approach. *Finite Elements in Analysis and Design*, 177:103417, 2020.

[22] SL Sing, CF Tey, JHK Tan, S Huang, and Wai Yee Yeong. 3D Printing of Metals in Rapid Prototyping of Biomaterials: Techniques in Additive Manufacturing. In *Rapid prototyping of biomaterials*, pages 17–40. Elsevier, 2020.

[23] Paul Gradl, Darren C Tinker, Alison Park, Omar R Mireles, Marissa Garcia, Ryan Wilkerson, and Christopher Mckinney. Robust Metal Additive Manufacturing Process Selection and Development for Aerospace Components. *Journal of Materials Engineering and Performance*, pages 1–32, 2022.

[24] Haijun Gong, Khalid Rafi, Hengfeng Gu, GD Janaki Ram, Thomas Starr, and Brent Stucker. Influence of Defects on Mechanical Properties of Ti–6Al–4 V Components Produced by Selective Laser Melting and Electron Beam Melting. *Materials & Design*, 86:545–554, 2015.

[25] Lore Thijs, Frederik Verhaeghe, Tom Craeghs, Jan Van Humbeeck, and Jean-Pierre Kruth. A Study of the Microstructural Evolution During Selective Laser Melting of Ti–6Al–4V. *Acta materialia*, 58(9):3303–3312, 2010.

[26] Thomas Vilaro, Christophe Colin, and Jean-Dominique Bartout. As-fabricated and Heat-treated Microstructures of the Ti-6Al-4V Alloy Processed by Selective Laser Melting. *Metallurgical and Materials Transactions A*, 42(10):3190–3199, 2011.

[27] Niloofar Sanaei and Ali Fatemi. Defects in additive manufactured metals and their effect on fatigue performance: A state-of-the-art review. *Progress in Materials Science*, 117:100724, 2021.

[28] Gengming Zhang, Chao Chen, Xiaojun Wang, Pengwei Wang, Xiaoyong Zhang, Xueping Gan, and Kechao Zhou. Additive Manufacturing of Fine-structured Copper Alloy by Selective Laser Melting of Pre-alloyed cu-15Ni-8Sn Powder. *The International Journal of Advanced Manufacturing Technology*, 96(9-12):4223–4230, 2018.

[29] Peter Mercelis and Jean-Pierre Kruth. Residual stresses in selective laser sintering and selective laser melting. *Rapid prototyping journal*, 2006.

[30] Zdeněk P Bažant. Size effect. *International Journal of Solids and Structures*, 37(1-2):69–80, 2000.

[31] Jay R Lund and Joseph P Byrne. Leonardo da vinci's tensile strength tests: Implications for the discovery of engineering mechanics. *Civil engineering systems*, 18(3):243–250, 2001.

[32] Alan Arnold Griffith. Vi. the phenomena of rupture and flow in solids. *Philosophical transactions of the royal society of london. Series A, containing papers of a mathematical or physical character*, 221(582-593):163–198, 1921.

[33] Waloddi Weibull, Waloddi Weibull, Sweden Physicist, Waloddi Weibull, Suède Physicien, and Waloddi Weibull. *A statistical representation of fatigue failures in solids*. Elander, 1949.

[34] George Ellwood Dieter and David Bacon. *Mechanical Metallurgy*, volume 3. McGraw-hill New York, 1976.

[35] Shun-Peng Zhu, Yang Ai, Ding Liao, José AFO Correia, Abílio MP De Jesus, and Qingyuan Wang. Recent advances on size effect in metal fatigue under defects: a review. *International Journal of Fracture*, 234(1):21–43, 2022.

[36] Paul R Gradl, Chris Protz, Sandra E Greene, David Ellis, Brad Lerch, and Ivan Locci. Development and hot-fire testing of additively manufactured

copper combustion chambers for liquid rocket engine applications. In *53rd AIAA/SAE/ASEE joint propulsion conference*, page 4670, 2017.

[37] Behzad Bahrami Babamiri, Joseph Indeck, Gabriel Demeneghi, Jefferson Cuadra, and Kavan Hazeli. Quantification of Porosity and Microstructure and Their Effect on Quasi-static and Dynamic Behavior of Additively Manufactured Inconel 718. *Additive Manufacturing*, 34:101380, 2020.

[38] A Du Plessis and EJAM Macdonald. Hot isostatic pressing in metal additive manufacturing: X-ray tomography reveals details of pore closure. *Additive Manufacturing*, 34:101191, 2020.

[39] Samuel Tammas-Williams, Philip J Withers, Iain Todd, and Philip B Prangnell. The Effectiveness of Hot Isostatic Pressing for Closing Porosity in Titanium Parts Manufactured by Selective Electron Bbeam Melting. *Metallurgical and materials transactions A*, 47:1939–1946, 2016.

[40] Gabriel Demeneghi, Baxter Barnes, Paul Gradl, Jason R Mayeur, and Kavan Hazeli. Size Effects on Microstructure and Mechanical Properties of Additively Manufactured Copper-Chromium-Niobium Alloy. *Materials Science and Engineering: A*, page 141511, 2021.

[41] L. Lu, Y. Shen, X. Chen, L. Qian, and K. Lu. Ultrahigh Strength and High Electrical Conductivity in Copper. *Science*, 304(5669):422–426, 2004.

[42] David R Lide. *CRC Handbook of Chemistry and Physics*, volume 85. CRC press, Boca Raton, 2004.

[43] Paul R Gradl, Christopher S Protz, Kevin Zagorski, Vishal Doshi, and Hannah McCallum. Additive Manufacturing and Hot-fire Testing of Bimetallic GRCop-84 and C-18150 channel-cooled Combustion Chambers using Powder Bed Fusion and Inconel 625 Hybrid Directed Energy Deposition. In *AIAA Propulsion and Energy 2019 Forum*, page 4390, 2019.

[44] David L Ellis and Gary M Michal. Precipitation strengthened high strength, high conductivity Cu-Cr-Nb alloys produced by chill block melt spinning. Technical report, 1989.

[45] William S Loewenthal and David L Ellis. GRCop-84 Rolling Parameter Study. Technical report, 2008.

[46] Kenneth Reed Anderson. Effects of Thermal and Mechanical Processing on Microstructures and Desired Properties of Particle-Strengthened Cu-Cr-Nb Alloys. Technical report, 2000.

[47] Henry C de Groh III, David Ellis, and William Loewenthal. Comparison of AMZIRC and GRCop-84. 2006.

[48] David L Ellis, Hugh R Gray, and Michael Nathel. Aerospace Structural Materials Handbook Supplement GRCop-84. 2001.

[49] David L Ellis. GRCop-84: A High-temperature Copper Alloy for High-heat-flux Applications. 2005.

[50] Henry C de Groh, David L Ellis, and William S Loewenthal. Comparison of GRCop-84 to other cu alloys with high thermal conductivities. *Journal of materials engineering and performance*, 17(4):594–606, 2008.

[51] Robert Minneci, Claudia Rawn, Jeff Bunn, Jarad Floyd, and Zachary Jones. Preliminary residual stress mapping of GRCop-84 fabricated by SLM. 2017.

[52] Paul R Gradl, Christopher S Protz, David L Ellis, and Sandy E Greene. Progress in Additively Manufactured Copper-Alloy GRCop-84, GRCop-42, and Bimetallic Combustion Chambers for Liquid Rocket Engines. 2019.

[53] KG Cooper, JL Lydon, MD LeCorre, ZC Jones, DS Scannapieco, DL Ellis, and BA Lerch. Three-dimensional printing GRCop-42. 2018.

[54] AH Seltzman and SJ Wukitch. Fracture characteristics and heat treatment of laser powder bed fusion additively manufactured GRCop-84 copper. *Materials Science and Engineering: A*, 827:141690, 2021.

[55] AH Seltzman and SJ Wukitch. Precipitate Size in GRCop-42 and GRCop-84 Cu-Cr-Nb Alloy Gas Atomized Powder and L-PBF Additive Manufactured Material. *Fusion Science and Technology*, pages 1–14, 2023.

[56] Ken R Anderson and Joanna R Groza. Microstructural size effects in high-strength high-conductivity Cu-Cr-Nb alloys. *Metallurgical and Materials Transactions A*, 32:1211–1224, 2001.

[57] Chunlei Qiu, GA Ravi, Chris Dance, Andrew Ranson, Steve Dilworth, and Moataz M Attallah. Fabrication of Large Ti-6Al-4V Structures by Direct Laser Deposition. *Journal of Alloys and Compounds*, 629:351–361, 2015.

[58] Ashwath Kumar, Yun Bai, Anders Eklund, and Christopher B Williams. Effects of Hot Isostatic Pressing on Copper Parts Fabricated via Binder Jetting. *Procedia Manufacturing*, 10:935–944, 2017.

[59] HV Atkinson and S Davies. Fundamental Aspects of Hot Isostatic Pressing: An Overview. *Metallurgical and Materials Transactions A*, 31(12):2981–3000, 2000.

[60] John Slotwinski, Edward Garboczi, and Keith Hebenstreit. Porosity Measurements and Analysis for Metal Additive Manufacturing Process Control. *Journal of Research of the National Institute of Standards and Technology*, 119:494–528, 2014.

[61] A. Thompson, I. Maskery, and R.K. Leach. X-ray Ccomputed Tomography for Additive Manufacturing: a Review. *Measurement Science and Technology*, 27:72001, 2016.

[62] A. Du Plessis, P. Sperling, A. Beerlink, W. B. Du Preez, and S. G. Le Roux. Standard Method for MicroCT-based Additive Manufacturing Quality Control 4: Metal Powder Analysis. *MethodsX*, 5:1336–1345, 2018.

[63] I. Maskery, N.T. Aboulkhair, M.R. Corfield, C. Tuck, A.T. Clare, R.K. Leach, R.D. Wildman, I. A. Ashcroft, and R.J.M. Hague. Quantification and Characterisation of Porosity in Selectively Laser Melted Al–Si10–Mg using X-ray Computed Tomography. *Materials Characterization*, 111:193–204, 2016.

[64] LG Vettraino, JL Heelan, CA Faconti, JL Walley, A Garg, JR Groza, and JC Gibeling. Influence of Processing on the Microstructure of Cu–8Cr–4Nb. *Journal of Materials Science*, 43(19):6546–6555, 2008.

[65] George F Vander Voort and William Van Geertruyden. Specimen Preparation for Electron Backscattered Diffraction. *McGraw-Hill Book Company Table*, 8:p23, 2010.

[66] Susan Swapp. Electron backscatter diffraction (EBSD), Oct 2021.

[67] Y.H. Wang, J.H. Jiang, C. Wanintrudal, C. Du, D. Zhou, L.M. Smith, and L.X. Yang. Whole Field Sheet-metal Tensile Test using Digital Image Correlation. *Experimental Techniques*, 34(2):54–59, 2010.

[68] M.A. Sutton, J. Orteu, and H.W. Schreier. *Image Correlation for Shape, Motion and Deformation Measurements*, volume 1. Springer, New York, 2009.

[69] L. Shi, X. Zhang, L. Zhang, C. Wang, and J. Wang. Application of Digital Image Correlation Technique in Stress and Strain Measurement. In *15th Asia Pacific Conference for Non-Destructive Testing*. NDT.net, 2018.

[70] P.L Reu, M. Sutton, Y. Wang, and T.J. Miller. Uncertainty Quantification for Digital Image Correlation. In *Imaging Methods for Novel Materials and Challenging Applications*. Springer, 2012.

[71] Ashley Roach, Benjamin White, Anthony Garland, Bradley Jared, Jay Carroll, and Brad Boyce. Size-dependent Stochastic Tensile Properties in Additively Manufactured 316L Stainless Steel. *Additive Manufacturing*, 32:101090, 2020.

[72] William G. Tilson and Colton Katsarelis. SLM Inconel 718 Thin Section Study. Technical Report MPFR-19-004, NASA Marshall Spaceflight Center, Huntsville, AL, 2019.

[73] Johannes Schindelin, Ignacio Arganda-Carreras, Erwin Frise, Verena Kaynig, Mark Longair, Tobias Pietzsch, Stephan Preibisch, Curtis Rueden, Stephan Saalfeld, Benjamin Schmid, et al. Fiji: an Open-source Platform for Biological-Image Analysis. *Nature Methods*, 9(7):676–682, 2012.

[74] A. Du Plessis, I. Yadroitsev, I. Yadroirsava, and S. G. Le Roux. X-Ray Microcomputed Tomography in Additive Manufacturing: A Review of the Current Technology and Applications. *3D Printing and Additive Manufacturing*, 5:227–247, 2018.

[75] Cheng-Han Yu, Ru Lin Peng, Vladimir Luzin, Maximilian Sprengel, Mattias Calmunger, Jan-Erik Lundgren, Håkan Brodin, Arne Kromm, and Johan Moverare. Thin-wall Effects and Anisotropic Deformation Mechanisms of

an Additively Manufactured Ni-based Superalloy. *Additive Manufacturing*, 36:101672, 2020.

[76] Seungjong Lee, Shuai Shao, Douglas N Wells, Miroslav Zetek, Miloslav Kepka, and Nima Shamsaei. Fatigue Behavior and Modeling of Additively Manufactured IN718: The Effect of Surface Treatments and Surface Measurement Techniques. *Journal of Materials Processing Technology*, 302:117475, 2022.

[77] Pierre Margerit, Daniel Weisz-Patrault, Krishnaswamy Ravi-Chandar, and Andrei Constantinescu. Tensile and Ductile Fracture Properties of as-printed 316L Stainless Steel Thin Walls Obtained by Directed Energy Deposition. *Additive Manufacturing*, 37:101664, 2021.

[78] Tracy Connor Varney, Tylee Oldham, Md Imran Noor, and Paul F Rottmann. Quantifying the Microstructure and Mechanical Property Differences between Bulk and Thin-wall Additively Manufactured Inconel 718. *Materialia*, 31:101867, 2023.

[79] ASTM E8/E8M-16a: Standard Test Methods for Tension Testing of Metallic Materials. ASTM International, West Conshohocken, PA, 2016.

[80] C. Chen, Y. Xie, X. Yan, S. Yin, H. Fukanuma, R. Huang, R. Zhao, J. Wang, Z. Ren, M. Liu, and H. Liao. Effect of Hot Isostatic Pressing (HIP) on Microstructure and Mechanical Properties of Ti-6Al-4V Alloy Fabricated by Cold Spray Additive Manufacturing. *Additive Manufacturing*, 27:595–605, 2019.

[81] P.R. Gradl, C. Protz, S.E. Greene, D. Ellis, and I. Locci. Development and Hot-fire Testing of Additively Manufactured Copper Combustion Chamber Liners for Liquid Rocket Engine Applications. *AIAA/SAE/ASEE Joint Propulsion Conference*, 53:4670, 2017.

[82] K. Moussaoui, W. Rubio, M. Mousseigne, T. Sultan, and F. Rezai. Effects of Selective Laser Melting Additive Manufacturing Parameters of Inconel 718 on Porosity, Microstructure and Mechanical Properties. *Materials Science and Engineering: A*, 735:182–190, 2018.

[83] Zhongfa Mao, David Z Zhang, Junjie Jiang, Guang Fu, and Peng Zhang. Processing Optimisation, Mechanical Properties and Microstructural Evolution during Selective Laser Melting of Cu-15Sn High-tin Bronze. *Materials Science and Engineering: A*, 721:125–134, 2018.

[84] Suman Das. Physical Aspects of Process Control in Selective Laser Sintering of Metals. *Advanced Engineering Materials*, 5(10):701–711, 2003.

[85] Thomas Vilaro, Christophe Colin, Jean-Dominique Bartout, Loic Nazé, and Mohamed Sennour. Microstructural and Mechanical Approaches of the Selective Laser Melting Process Applied to a Nickel-Base Superalloy. *Materials Science and Engineering: A*, 534:446–451, 2012.

[86] Luke N Carter, Christopher Martin, Philip J Withers, and Moataz M Attallah. The Influence of the Laser Scan Strategy on Grain Structure and Cracking Behaviour in SLM Powder-bed Fabricated Nickel Superalloy. *Journal of Alloys and Compounds*, 615:338–347, 2014.

[87] MW Decker, JR Groza, and JC Gibeling. Creep Properties of an Extruded Copper–8% Chromium–4% Niobium Alloy. *Materials Science and Engineering: A*, 369(1-2):101–111, 2004.

[88] Henry C deGroh III, David L Ellis, and William S Loewenthal. Comparison of GRCop-84 to Other High Thermal Conductive Cu Alloys. Technical Report 2007-214663, NASA Glenn Research Center, Cleveland, OH, 2007.

[89] R.P. Minneci, E.A. Lass, J.R. Bunn, H. Choo, and C.J. Rawn. Copper-based Alloys for Structural High-Heat-Flux Applications: A Review of Development, Properties, and Performance of Cu-rich Cu-Cr-Nb Alloys. *International Materials Reviews*, pages 1–32, 2020.

[90] CJ Todaro, MA Easton, D Qiu, D Zhang, MJ Bermingham, EW Lui, M Brandt, DH StJohn, and M Qian. Grain Structure Control During Metal 3D Printing by High-intensity Ultrasound. *Nature Communications*, 11(1):1–9, 2020.

[91] Suraj Dinkar Jadhav, Sasan Dadbakhsh, Louca Goossens, JP Kruth, Jan Van Humbeeck, and Kim Vanmeensel. Influence of Selective Laser Melt-

ing Process Parameters on Texture Evolution in Pure Copper. *Journal of Materials Processing Technology*, 270:47–58, 2019.

[92] Ben Brown, Wes Everhart, and Joe Dinardo. Characterization of Bulk to Thin Wall Mechanical Response Transition in Powder Bed AM. *Rapid Prototyping Journal*, 22(5):801–809, 2016.

[93] J.K. Algardh, T. Horn, H. West, R. Aman, A. Snis, H. Engqvist, J. Lausmaa, and O. Harrysson. Thickness Dependency of Mechanical Properties for Thin-walled Titanium Parts Manufactured by Electron Beam Melting (EBM). *Additive Manufacturing*, 12:45–50, 2016.

[94] D Arola and CL Williams. Estimating the Fatigue Stress Concentration Factor of Machined Surfaces. *International Journal of Fatigue*, 24:923–930, 2002.

[95] B. Vayssette, N. Saintier, C. Brugger, and M. El May. Surface Roughness Effect of SLM and EBM Ti-6Al-4V on Multiaxial High Cycle Fatigue. *Theoretical and Applied Fracture Mechanics*, 108:102581, 2020.

[96] J Dzugan, M Seifi, R Prochazka, M Rund, P Podany, P Konopik, and JJ Lewandowski. Effects of Thickness and Orientation on the Small Scale Fracture Behaviour of Additively Manufactured Ti-6Al-4V. *Materials Characterization*, 143:94–109, 2018.

[97] H. D. Carlton, A. Haboub, G. F. Gallegos, D.Y. Parkinson, and A. A. MacDowell. Damage Evolution and Failure Mechanisms in Additively Manufactured Stainless Steel. *Materials Science and Engineering: A*, 651:406–414, 2016.

[98] A. Y. Al-Maharma, S. P. Patil, and B. Markert. Effects of Porosity on the Mechanical Properties of Additively Manufactured Components: a Critical Review. *Materials Research Express*, 7:122001, 2020.

[99] B.J. Mfusi, N.R. Mathe, L.C. Tshabalala, and P.A. Popoola. The Effect of Stress Relief on the Mechanical and Fatigue Properties of Additively Manufactured Al-Si10-Mg Parts. *Metals*, 9:1216, 2019.

[100] Kazuhisa Miyoshi. *Surface Characterization Techniques: An Overview*. CRC Press, 2004.

[101] Benoit Rosa, Antoine Brient, Serge Samper, and Jean-Yves Hascoët. Influence of Additive Laser Manufacturing Parameters on Surface using Density of Partially Melted Particles. *Surface Topography: Metrology and Properties*, 4(4):045002, 2016.

[102] S Yadav, CP Paul, AN Jinoop, AK Rai, and KS Bindra. Laser Directed Energy Deposition Based Additive Manufacturing of Copper: Process Development and Material Characterizations. *Journal of Manufacturing Processes*, 58:984–997, 2020.

[103] John Hock Lye Pang, Jacek Kaminski, Helene Pepin, et al. Characterisation of Porosity, Density, and Microstructure of Directed Energy Deposited Stainless Steel AISI 316L. *Additive Manufacturing*, 25:286–296, 2019.

[104] Sunil Yadav, Christ P Paul, Arackal N Jinoop, Saurav K Nayak, Arun K Rai, and Kushvinder S Bindra. Effect of Process Parameters on Laser Directed Energy Deposition of Copper. In *Gas Turbine India Conference*, volume 83532, page V002T10A004. American Society of Mechanical Engineers, 2019.

[105] O Nenadl, V Ocelik, and J Th M De Hosson. Texture Development in Direct Powder Deposition. *Journal of Laser Applications*, 29(4):042007, 2017.

[106] Camille Guevenoux, Simon Hallais, Alexandre Charles, Eric Charkaluk, and Andrei Constantinescu. Influence of Interlayer Dwell Time on the Microstructure of Inconel 718 Laser Cladded Components. *Optics & Laser Technology*, 128:106218, 2020.

[107] Yanis Balit, Eric Charkaluk, and Andrei Constantinescu. Digital Image Correlation for Microstructural Analysis of Deformation Ppattern in Additively Manufactured 316L Thin Walls. *Additive Manufacturing*, 31:100862, 2020.

[108] HL Wei, J Mazumder, and Tarasankar DebRoy. Evolution of Solidification Texture During Additive Manufacturing. *Scientific reports*, 5(1):1–7, 2015.

[109] Camille Guévenoux, Simon Hallais, Yanis Balit, Alexandre Charles, Eric Charkaluk, and Andrei Constantinescu. Plastic Strain Localization Induced

by Microstructural Gradient in Laser Cladding Repaired Structures. *Theoretical and Applied Fracture Mechanics*, 107:102520, 2020.

[110] S.I. Wright. Orientation texture. In Franco Bassani, Gerald L. Liedl, and Peter Wyder, editors, *Encyclopedia of Condensed Matter Physics*, pages 221–233. Elsevier, Oxford, 2005.

[111] Alphons Anandaraj Antonysamy, J Meyer, and PB Prangnell. Effect of Build Geometry on the β-grain Structure and Texture in Additive Manufacture of Ti6Al4V by Selective Electron Beam Melting. *Materials characterization*, 84:153–168, 2013.

[112] Karsten Kunze, Thomas Etter, Jürgen Grässlin, and Valery Shklover. Texture, Anisotropy in Microstructure and Mechanical Properties of IN738LC Alloy Processed by Selective Laser Melting (SLM). *Materials Science and Engineering: A*, 620:213–222, 2015.

[113] JFS Markanday, MA Carpenter, NG Jones, RP Thompson, SE Rhodes, CP Heason, and HJ Stone. Occurrence of a Brass Texture and Elastic Anisotropy in Laser Blown Powder Processed Superalloy IN718. *Materials Science and Engineering: A*, 825:141781, 2021.

[114] GP Dinda, AK Dasgupta, and J Mazumder. Texture Control During Laser Deposition of Nickel-based Superalloy. *Scripta Materialia*, 67(5):503–506, 2012.

[115] Sarah Wolff, Taekyung Lee, Eric Faierson, Kornel Ehmann, and Jian Cao. Anisotropic Properties of Directed Energy Deposition (DED)-Processed Ti-6Al-4V. *Journal of Manufacturing Processes*, 24:397–405, 2016.

[116] M Godec, S Malej, D Feizpour, Č Donik, M Balažic, D Klobčar, L Pambaguian, M Conradi, and A Kocijan. Hybrid additive manufacturing of Inconel 718 for future space applications. *Materials Characterization*, 172:110842, 2021.

[117] Tarasankar DebRoy, HL Wei, JS Zuback, Tuhin Mukherjee, JW Elmer, JO Milewski, Allison Michelle Beese, A de Wilson-Heid, Amitava De, and Wei Zhang. Additive manufacturing of metallic components–process, structure and properties. *Progress in Materials Science*, 92:112–224, 2018.

[118] Lova Chechik and Iain Todd. Inconel 718 two ways: Powder bed fusion vs. directed energy deposition. *Additive Manufacturing Letters*, 6:100145, 2023.

[119] Mohammad H. Farshidianfar, Amir Khajepour, and Adrian P. Gerlich. Effect of Real-time Cooling Rate on Microstructure in Laser Additive Manufacturing. *Journal of Materials Processing Technology*, 231:468–478, 2016.

[120] Dongdong Gu and Yifu Shen. Balling phenomena in direct laser sintering of stainless steel powder: Metallurgical mechanisms and control methods. *Materials & Design*, 30(8):2903–2910, 2009.

[121] K Darvish, ZW Chen, and T Pasang. Reducing lack of fusion during selective laser melting of cocrmo alloy: Effect of laser power on geometrical features of tracks. *Materials & Design*, 112:357–366, 2016.

[122] Wayne E King, Holly D Barth, Victor M Castillo, Gilbert F Gallegos, John W Gibbs, Douglas E Hahn, Chandrika Kamath, and Alexander M Rubenchik. Observation of keyhole-mode laser melting in laser powder-bed fusion additive manufacturing. *Journal of Materials Processing Technology*, 214(12):2915–2925, 2014.

[123] Chunlei Qiu, Chinnapat Panwisawas, Mark Ward, Hector C Basoalto, Jeffery W Brooks, and Moataz M Attallah. On the role of melt flow into the surface structure and porosity development during selective laser melting. *Acta Materialia*, 96:72–79, 2015.

[124] Gabriel Demeneghi, Baxter Barnes, Paul Gradl, David Ellis, Jason R Mayeur, and Kavan Hazeli. Directed energy deposition GRCop-42 copper alloy: Characterization and size effects. *Materials & Design*, 222:111035, 2022.

[125] Meurig Thomas, Gavin J Baxter, and Iain Todd. Normalised model-based processing diagrams for additive layer manufacture of engineering alloys. *Acta Materialia*, 108:26–35, 2016.

[126] Sindo Kou. Welding metallurgy. *New Jersey, USA*, 431(446):223–225, 2003.

[127] H Helmer, A Bauereiß, RF Singer, and C Körner. Grain structure evolution in Inconel 718 during selective electron beam melting. *Materials Science and Engineering: A*, 668:180–187, 2016.

[128] Niels Hansen. Hall–Petch relation and boundary strengthening. *Scripta materialia*, 51(8):801–806, 2004.

[129] A Amine Benzerga and Jean-Baptiste Leblond. Ductile Fracture by Void Growth to Coalescence. *Advances in applied mechanics*, 44:169–305, 2010.

[130] AR Vishnu, G Vadillo, and JA Rodríguez-Martínez. Void growth in ductile materials with realistic porous microstructures. *International Journal of Plasticity*, page 103655, 2023.

[131] C Sun, X Zhang, X Liu, and Y Hong. Effects of specimen size on fatigue life of metallic materials in high-cycle and very-high-cycle fatigue regimes. *Fatigue & Fracture of Engineering Materials & Structures*, 39(6):770–779, 2016.

[132] Andrea Carpinteri, Andrea Spagnoli, and Sabrina Vantadori. Size effect in S–N curves: A fractal approach to finite-life fatigue strength. *International Journal of Fatigue*, 31(5):927–933, 2009.

[133] M Shirani and G Härkegård. Fatigue life distribution and size effect in ductile cast iron for wind turbine components. *Engineering Failure Analysis*, 18(1):12–24, 2011.

[134] Gang Wang, Chen Gao, Yue Zhang, GuangTao Xu, and MingHao Zhao. Size Effect on the Fatigue Performance of 18CrNiMo7-6 Alloy Steel. *steel research international*, 92(9):2100054, 2021.

[135] Y. G. Bu. Investigation of the Size Effect with Regard to the Fatigue Strength of Typical Al Alloy Mechanical Elements in Aeronaultical Structures. *Tsinghua University*, 2012.

[136] Ali Fatemi, Reza Molaei, Shahriar Sharifimehr, Nam Phan, and Nima Shamsaei. Multiaxial fatigue behavior of wrought and additive manufactured Ti-6Al-4V including surface finish effect. *International Journal of Fatigue*, 100:347–366, 2017.

[137] D Butcher, S Christie, SGR Brown, and NP Lavery. Validated Computational Modelling Techniques for Simulating Melt Pool Ejecta In Laser Powder Bed Fusion Processing. In *2019 International Solid Freeform Fabrication Symposium*. University of Texas at Austin, 2019.

[138] Yang Liu, Yongqiang Yang, Shuzhen Mai, Di Wang, and Changhui Song. Investigation into spatter behavior during selective laser melting of AISI 316L stainless steel powder. *Materials & Design*, 87:797–806, 2015.

[139] Nabeel Ahmad, Shuai Shao, Mohsen Seifi, and Nima Shamsaei. Additively manufactured in718 in thin wall and narrow flow channel geometries: Effects of post-processing and wall thickness on tensile and fatigue behaviors. *Additive Manufacturing*, 60:103264, 2022.

[140] Ali Fatemi, Reza Molaei, Jutima Simsiriwong, Niloofar Sanaei, Jonathan Pegues, Brian Torries, Nam Phan, and Nima Shamsaei. Fatigue behaviour of additive manufactured materials: An overview of some recent experimental studies on ti-6al-4v considering various processing and loading direction effects. *Fatigue & fracture of engineering materials & structures*, 42(5):991–1009, 2019.

[141] Seungjong Lee, Jonathan W Pegues, and Nima Shamsaei. Fatigue behavior and modeling for additive manufactured 304L stainless steel: The effect of surface roughness. *International Journal of Fatigue*, 141:105856, 2020.

[142] Rakish Shrestha, Jutima Simsiriwong, and Nima Shamsaei. Fatigue Behavior of Additive Manufactured 316L Stainless Steel parts: Effects of Layer Orientation and Surface Roughness. *Additive Manufacturing*, 28:23–38, 2019.

[143] Yuting Lv, Yang Ding, Yuanfei Han, Lai-Chang Zhang, Liqiang Wang, and Weijie Lu. Strengthening mechanism of friction stir processed and post heat treated NiAl bronze alloy: effect of rotation rates. *Materials Science and Engineering: A*, 685:439–446, 2017.

[144] Wolfgang Schneller, Martin Leitner, Sebastian Springer, Florian Grün, and Michael Taschauer. Effect of HIP Treatment on Microstructure and Fatigue Strength of Selectively Laser Melted AlSi10Mg. *Journal of Manufacturing and Materials Processing*, 3(1):16, 2019.

[145] Eric Wycisk, Claus Emmelmann, Shafaqat Siddique, and Frank Walther. High cycle fatigue (HCF) performance of Ti-6Al-4V alloy processed by selective laser melting. In *Advanced materials research*, volume 816, pages 134–139. Trans Tech Publ, 2013.

[146] Jaehyun Yu, Dohyung Kim, Kyeongsik Ha, Jong Bae Jeon, Dong Joo Kim, and Wookjin Lee. Size effect due to contour laser scanning in 316l stainless steel produced by laser powder bed fusion. *Journal of Materials Research and Technology*, 15:5554–5568, 2021.

[147] Milad Hamidi Nasab, Simone Romano, Dario Gastaldi, Stefano Beretta, and Maurizio Vedani. Combined effect of surface anomalies and volumetric defects on fatigue assessment of AlSi7Mg fabricated via laser powder bed fusion. *Additive Manufacturing*, 34:100918, 2020.

[148] Joseph Indeck, Jefferson Cuadra, Cyril Williams, and Kavan Hazeli. Accumulation and evolution of elastically induced defects under cyclic loading: Quantification and subsequent properties. *International Journal of Fatigue*, 127:522–536, 2019.

[149] Joseph Indeck, Gabriel Demeneghi, Jason Mayeur, Cyril Williams, and Kavan Hazeli. Influence of reversible and non-reversible fatigue on the microstructure and mechanical property evolution of 7075-T6 aluminum alloy. *International Journal of Fatigue*, 145:106094, 2021.

[150] Joseph Indeck, David Cereceda, Jason R Mayeur, and Kavan Hazeli. Understanding slip activity and void initiation in metals using machine learning-based microscopy analysis. *Materials Science and Engineering: A*, 838:142738, 2022.

[151] MA Balbaa, A Ghasemi, E Fereiduni, MA Elbestawi, SD Jadhav, and J-P Kruth. Role of powder particle size on laser powder bed fusion processability of AlSi10Mg alloy. *Additive manufacturing*, 37:101630, 2021.

[152] DQ Zhang, ZH Liu, and CK Chua. Investigation on Forming Process of Copper Alloys via Selective Laser Melting. In *High Value Manufacturing: Proceedings of the 6th International Conference on Advanced Research in Virtual and Rapid Prototyping, Leiria, Portugal*, page 285, 2013.

[153] Ken Imai, Toshi-Taka Ikeshoji, Yuji Sugitani, and Hideki Kyogoku. Densification of Pure Copper by Selective Laser Melting Process. *Mechanical Engineering Journal*, pages 19–25, 2020.

[154] Toshi-Taka Ikeshoji, Kazuya Nakamura, Makiko Yonehara, Ken Imai, and Hideki Kyogoku. Selective Laser Melting of Pure Copper. *JOM*, 70(3):396–400, 2018.

[155] PA Lykov, EV Safonov, and AM Akhmedianov. Selective Laser Melting of Copper. In *Materials Science Forum*, volume 843, pages 284–288. Trans Tech Publ, 2016.

Appendix A. Material Systems and Experimental Procedure

A.1 Tested Specimens: L-PBF

The number of specimens of each thickness and heat treatment is reported in Table 1.The number of specimens reported in Table 1 does not include the specimens machined to remove the surface roughness. Generally, at least two specimens of in each condition were tested. Table 1 also reports the dimensions each specimen as measured with calipers. The width and thickness values reported are averages of the width and thickness measured at three locations within the gauge section of each specimen.

Table A.1: Table showing the number of specimens of each thickness and heat treatment tested, and the dimensions of each specimen considered in the present study.

Specimen	Caliper Measured Width (mm)	Caliper Measured Thickness (mm)	Caliper Measured Area (mm^2)
AB 0.7mm 1	5.55	0.730	4.05
AB 1.0mm 1	5.56	0.973	5.41
AB 1.0mm 2	5.58	0.987	5.51
AB 1.0mm 3	5.59	0.970	5.42
AB 1.7mm 1	5.62	1.700	9.55
AB 1.7mm 2	5.60	1.693	9.48
AB 2.0mm 1	5.63	2.287	12.87
AB 2.0mm 2	5.66	2.297	13.00
HIP 0.7mm 1	5.54	0.710	3.93
HIP 0.7mm 2	5.52	0.710	3.92
HIP 0.7mm 3	5.52	0.703	3.88
HIP 0.7mm 4	5.58	0.703	3.92
HIP 1.0mm 1	5.55	1.010	5.61
HIP 1.0mm 2	5.53	0.970	5.36
HIP 1.0mm 3	5.57	0.960	5.35
HIP 1.0mm 4	5.56	0.953	5.30
HIP 1.7mm 1	5.59	1.680	9.39
HIP 1.7mm 2	5.62	1.690	9.50
HIP 1.7mm 3	5.59	1.727	9.65
HIP 1.7mm 4	5.59	1.697	9.48
HIP 2.0mm 1	5.61	2.307	12.94
HIP 2.0mm 2	5.62	2.293	12.89

Table 2 presents the percentage decrease in Young's modulus, yield strength, UTS, and elongation as thickness decreases. Stress values are calculated with areas determined through μCT scans. The decrease in Young's Modulus as thickness is reduced from 2 to 0.7mm is 37.6% for as-built specimens and 23.3% for HIP specimens. The decrease in Yield Strength and UTS is greater than 20% for both heat treatment conditions. Elongation in as-built specimens is reduced by nearly 50% for both as-built and HIP conditions.

Table A.2: Table showing the mechanical properties as specimen thickness decreases.

Specimen	**Young's Modulus (GPa)**	**Yield Strength (MPa)**	**UTS (MPa)**	**% Elongation (%)**
2mm AB	84.5 ±0.3	306.8 ±2.4	496.8 ±2.4	19.0 ±0.8
1.7mm AB	74.8 ±0.2	284.2 ±0.5	453.6 ±1.7	16.3 ±0.4
1mm AB	64.6 ±15.0	251.7 ±2.4	399.3 ±4.0	13.1 ±0.4
0.7mm AB	52.8 ±3.3	230.0 ±6.5	352.9 ±7.4	10.0 ±0.8
2mm HIP	91.2 ±0.2	173.0 ±2.9	345.4 ±1.8	22.6 ±2.4
1.7mm HIP	83.6 ±12.3	165.4 ±2.4	330.8 ±5.9	25.4 ±2.2
1mm HIP	71.5 ±26.9	144.7 ±4.2	287.3 ±9.9	19.7 ±3.0
0.7mm HIP	70.0 ±19.8	134.7 ±2.7	263.2 ±8.3	11.6 ±7.5

A decrease in mechanical properties with decreasing thickness is still apparent, but diminished when compared to stress calculations made using caliper-measured area. In the as-built condition, a 35% decrease in UTS is observed between the 2.0mm and 0.7mm when area is measured with calipers; measuring these areas with optical microscopy shows only a 9% decrease, while measuring these cross-sectional areas with µCT scans shows a 29% decrease in UTS between the 2.0mm and 0.7mm specimens. A similar trend is observed in the HIP condition. This indicates that while the reduction in load-bearing area is at least partially responsible for the apparent decrease in strength, it is not the only factor. Furthermore, the percentage reduction in Young's modulus, yield strength and UTS is greater in as-built specimens than in HIP specimens, indicating that heat treatment reduces the magnitude of the mechanical property decrease with decreasing thickness. This is consistent with data presented in [17, 52, 89].

A.2 Tested Specimens: LP-DED

Table 3 lists the Cr and Nb wt%, their ratios for each specimen in addition to trace elements in parts per million (ppm).

Table A.3: Chemical composition for the different deposited specimens.

	T1C1	**T1C2**	**T2C1**	**T2C2**
Thickness (mm)	1.2	1.2	1.6	1.6
Cu	Remainder	Remainder	Remainder	Remainder
Cr (wt%)	3.13	3.30	3.13	3.30
Nb (wt%)	2.90	2.90	2.90	2.90
Fe (ppm)	40	30	40	30
O (ppm)	290	380	290	380
Al (ppm)	400	530	400	530
Si (ppm)	320	350	320	350
C (ppm)	<100	<50	<100	<50
S (ppm)	<100	10	<100	10
N (ppm)	<100	<10	<100	<10
Cr/Nb (wt% ratio)	1.08	1.14	1.08	1.14
Composition	C1	C2	C1	C2

Table 4 shows all specimens tested during this study. A total of 40 specimens were tested to ensure reproducibility of the uniaxial test results, including horizontal and vertical specimens in the unpolished condition, which have the as-built surface topography, and polished condition.

Table A.4: Quasi-statically tested specimens used for this study.

	As-printed		**Polished**	
	Horizontal	**Vertical**	**Horizontal**	**Vertical**
T1C1	3	3	2	2
T1C2	3	3	2	2
T2C1	3	3	2	2
T2C2	3	3	2	2